# Theoretical Investigation of Nanostructured Thermoelectric Materials

Inaugural Dissertation

to obtain the academic degree

Doctor rerum naturalium (Dr. rer. nat.)

submitted to
the Department of Biology, Chemistry and Pharmacy
of Freie Universität Berlin

by
Lukas Hammerschmidt
from Tübingen
2015

This work was prepared under supervision of
Prof. Dr. Beate Paulus (Freie Universität Berlin)
from March 2011 until April 2015

| | |
|---|---|
| 1. Gutachter: | Prof. Dr. Beate Paulus |
| 2. Gutachter: | Prof. Dr. Thomas Risse |
| Disputation am | 15. Juni 2015 |

ignotum per ignotius

# Summary

Todays increasing demands on electrical power raise the challenging task to find alternative, renewable and sustainable power sources. By now it becomes apparent that only a combination of many alternative power sources will be able to promote the transition from fossile fuel to sustainable energy production. In this transition, thermoelectric materials may play their part for example in waste heat recovery, since they are ideal energy converter that transform heat directly and reversibly into electricity. Recent progress in the field of thermoelectric materials inspired start-ups and the appearance of next-generation thermoelectric technology in cars. Although they are already employed in applications, until today the efficiency of common thermoelectric materials is still quite small to compete on a large scale against other alternative power sources. However, by certain changes in the structure, thermoelectric materials allow in principle to be optimized with respect to their efficiency. Besides that, their reliability and the fact that they involve no moving parts leave them as ideal niche products already today, whenever exactly these properties are key.

Prototypical thermoelectric materials are based on telluride compounds often in combination with lead. Novel and promising thermoelectric materials are lead free and for example constituted by the class of skutterudites. In this work, the concept of skutterudites as thermoelectric materials is reviewed and their peculiar electronic structure and transport properties are analyzed within the means of first-principles computations. Based on calculations a model is developed that explains earlier inconsistent findings and that describes the orbital interactions and contributions to the characteristic shape of the valence bands of skutterudites.

Further improvement of skutterudites as thermoelectrics leads down two roads: filling of the vacant 2*a* Wyckoff positions and nanostructuring. This work goes a step along both roads. Filled skutterudites are investigated for group-13 atoms as filling species and their influence on the electronic properties is examined. A step towards nanostructuring is taken for the parent material $CoSb_3$ by studying the surface energetics and electronic structures of the low-index surfaces (100), (110) and (111). In this context, two new schemes are proposed of which the first one allows to calculate surface energies for symmetric but off-stoichiometric slabs and the second one allows to calculate the electron correlation in surfaces in terms of wave function based electron correlation methods. Finally, this work shows that electron correlation contributes greatly to the binding in common thermoelectric materials and, starting from model systems, takes a step towards the application of local correlation methods like the periodic LMP2 method to study these effects.

# Zusammenfassung

Der weltweit steigende Energiebedarf hat in den letzten Jahren zu einem wachsenden wissenschaftlichen Interesse an alternativen und nachhaltigen Energiequellen geführt. Mittlerweile zeigt sich, dass nur durch eine Kombination aus vielen verschiedenen erneuerbaren Energiequellen die Energiewende gelingen kann. Einen solchen Beitrag könnten zum Beispiel auch thermoelektrischen Materialien beisteuern. Sogenannte Thermoelektrika wandeln reversibel und direkt thermische Energie in elektrische Energie um. Demnach könnten Thermoelektrika dazu beitragen, wo immer Energie durch Abwärme verloren geht, diese zurückzugewinnen. Die jüngsten Fortschritte auf dem Gebiet der Thermoelektrika haben mittlerweile schon zur Einführung dieser Technologie in Autos und zu Unternehmensgründungen geführt. Ungeachtet der Tatsache, dass sie bereits Anwendung im Alltag finden, zeigen thermoelektrische Materialien jedoch noch immer eine recht gering Effizienz. Diese lässt sich aber, wie Forschungsergebnisse zeigen, durch Materialveränderungen optimieren. Außerdem sind thermoelektrische Elemente in der Regel sehr zuverlässig und erzeugen Elektrizität ohne die Verwendung von sich bewegenden Teilen. Allein schon diese besonderen Eigenschaften eröffnen ihnen bereits heute einen stetig wachsenden Markt als Nischenprodukte.

Thermoelektrische Materialien, die bereits Anwendung finden, basieren typischerweise auf Tellur, oft in Verbindung mit Blei. Neuartige und vielversprechende Kandidaten für thermoelektrische Materialien sind bleifrei und basieren zum Beispiel auf der Verbindungsklasse der Skutterudite. Die vorliegende Arbeit beschäftigt sich mit Skutteruditen als thermoelektrischen Materialien und erforscht ihre elektronische Struktur und Transporteigenschaften mit Hilfe theoretischer *first-principles* Methoden. Auf Basis dieser Untersuchung wird ein Modell entwickelt, welches die widersprüchlichen Ergebnisse verschiedener vorhergehender Arbeiten zufriedenstellend erklärt.

Darüber hinaus untersucht diese Arbeit die Optimierung von Skutteruditen. Skutterudite lassen sich entweder durch Nanostrukturierung oder das Füllen der unbesetzten $2a$-Wyckoff Positionen optimieren. In dieser Arbeit wird die Auswirkungen beider Optimierungsmöglichkeiten von Skutteruditen – Füllung und Nanostrukturierung – auf die elektronische Struktur und deren Transporteigenschaften untersucht. Als Fülleratome werden Gruppe-13 Atome betrachtet. Durch Berechnung der Oberflächenenergien niedrigindizierter $CoSb_3$ Oberflächen wird ein Schritt Richtung Nanostrukturierung unternommen. In diesem Zusammenhang werden zwei Methoden dargestellt, von der die eine erlaubt Oberflächenenergien symmetrischer, nicht stöchiometrischer Slabs zu berechnen, während die andere Einblicke in den Beitrag von Elektronenkorrelation zur Oberflächenenergie ermöglicht. Abschließend betrachtet die vorliegende Arbeit ganz grundsätzlich den Bindungsbeitrag von Elektronenkorrelation in Thermoelektrika und zeigt Möglichkeiten der Anwendung auf.

# List of Publications

A1 L. Hammerschmidt, S. Schlecht, and B. Paulus
*Electronic Structure and the Groundstate Properties of Cobalt Antimonide Skutterudites: Revisited with different theoretical methods*
Phys. Status Solidi A, **210**, 131-139 (2013)
DOI: 10.1002/pssa.201228453

A2 M. V. Daniel, L. Hammerschmidt, C. Schmidt, F. Timmermann, J. Franke, G. Beddies, N. Jöhrmann, M. Hietschold, D. C. Johnson, B. Paulus, and M. Albrecht
*Structural and Thermoelectric Properties of $FeSb_3$ Skutterudite Thin Films*
Phys. Rev. B, **91**, 085410 (2015)
DOI: 10.1103/PhysRevB.91.085410

A3 L. Hammerschmidt, M. Quennet, K. Töpfer, and B. Paulus
*Low-indexed Surfaces of $CoSb_3$ Skutterudites From First Principles*
Surf. Sci., accepted (2015)
DOI: 10.1016/j.susc.2015.03.020

A4 L. Hammerschmidt, L. Maschio, C. Müller, and B. Paulus
*Electron Correlation at the $MgF_2$(110) Surface: A Comparison of Incremental and Local Correlation Methods*
J. Chem. Theor. Comput., **11**, 252-259 (2014)
DOI: 10.1021/ct500841b

A5 S. Torabi, L. Hammerschmidt, E. Voloshina, and B. Paulus
*Ab Initio Investigation of Ground-State Properties of Group-12 Fluorides*
Int. J. Quant. Chem., **114**, 943-951 (2014)
DOI: 10.1002/qua.24695

## Additional Publications

B1 P. Leicht, L. Zielke, S. Bouvron, R. Moroni, E. Voloshina, L. Hammerschmidt, Y. S. Dedkov, and M. Fonin
*In Situ Fabrication of Quasi-Free-Standing Epitaxial Graphene Nanoflakes on Gold*
ACS Nano, **8**, 2725-2742 (2014)
DOI: 10.1021/nn500396c

B2 L. Hammerschmidt, C. Müller, and B. Paulus
*Electron Correlation Contribution to the Physisorption of CO on $MgF_2$(110)*
J. Chem. Phys., **136**, 124117 (2012)
DOI: 10.1063/1.3697867

B3 C. Erk, L. Hammerschmidt, D. Andrae, B. Paulus, and S. Schlecht
*Low-temperature Formation of Cubic $\beta$ -$PbF_2$: Precursor-based Synthesis and First-Principles Phase Stability Study*
Phys. Chem. Chem. Phys., **13**, 6029-6035 (2011)
DOI: 10.1063/1.3697867

# Contents

# List of Figures

# List of Tables

# List of Abbreviations

**PGEC** phonon glass electron crystal

**LAPW** linearized augmented-plane-wave

**MBD** many-body dispersion

**HF** Hartree-Fock

**SCF** self-consistent-field

**DFT** density functional theory

**LDA** local density approximation

**GGA** generalized gradient approximation

**BZ** Brillouin zone

**BSSE** basis set superposition error

**CI** configuration interaction

**CC** coupled cluster

**RTA** relaxation time approximation

**MoI** method of increments

**LMP2** Local-MP2

**PAO** projected atomic orbital

**HO** highest occupied

# Chapter 1

# Introduction

The growing interest in the search for alternative, new and renewable energy sources is mainly inspired by the increasing needs of power in our modern societies. In the last ten years alone, the world's primary energy consumption climbed from 360 to about $550 \cdot 10^{15}$ kJ [1] and with the industrialization of emerging countries and the growth of population, the consumption is expected to keep increasing. Although fossil energy sources are finite, they still account for the largest share in energy production. The proportion of sustainable energies differs greatly from country to country. In Germany renewable energies account for about 10 % of the primary energy consumption and are produced from a wide variety of sources[1]. Nowadays, it becomes apparent that the diversity of renewable energy sources is key in the transition from fossil fuel to sustainable energy production. In this transition the class of thermoelectric materials might play their part in the near future [2–12].

In principle, thermoelectric materials are ideal energy converter and transform heat directly and reversibly into electricity or vice versa. The discovery of the so-called thermoelectric effects dates back to work by Seebeck, Peltier and Thomson [13–16]. A schematic view on a modern thermoelectric module is shown in Fig. 1.1. In principle the thermoelectric effect is present in all materials, but only few are suitable and only those comprise the material group of thermoelectrics. Already in 1909 and 1911, Altenkirch identified a high thermoelectric coefficient, a high electrical conductivity and a low thermal conductivity as the principle requirements for efficient thermoelectric materials [17, 18]. The measure of the quality of a thermoelectric material is the dimensionless figure of merit [19]

$$ZT = \frac{S^2\,\sigma}{\kappa + \kappa_0}\,T, \tag{1.1}$$

where $T$ is the temperature, $S$ the Seebeck coefficient, $\sigma$ the electrical conductivity, $\kappa$ the lattice thermal conductivity and $\kappa_0$ the electronic part of the the thermal conductivity. The numerator of Eq. 1.1 is often called the power factor. Todays efficient thermoelectric materials own a $ZT > 1$. Unfortunately, the transport coefficients are interdependent and the optimization of each coefficient individually is limited. Thus, novel thermoelectric materials are based on nanostructuring, the phonon glass electron crystal (PGEC) concept, or a combination of both.

With the PGEC, Slack introduced a concept to guide the search for novel thermoelectric materials [20]. He proposed five requirements for high efficiency. First, the lattice thermal

[1] biomass 5.5 %, wind power 1.3 %, hydro power 0.5 %, heat pumps 0.2 %, photovoltaics 0.8 %, geo- and solarthermy 0.285 %, waste gas 0.9 %, bio fuels 0.8 % (Germany, effective Feb. 2013) [1]

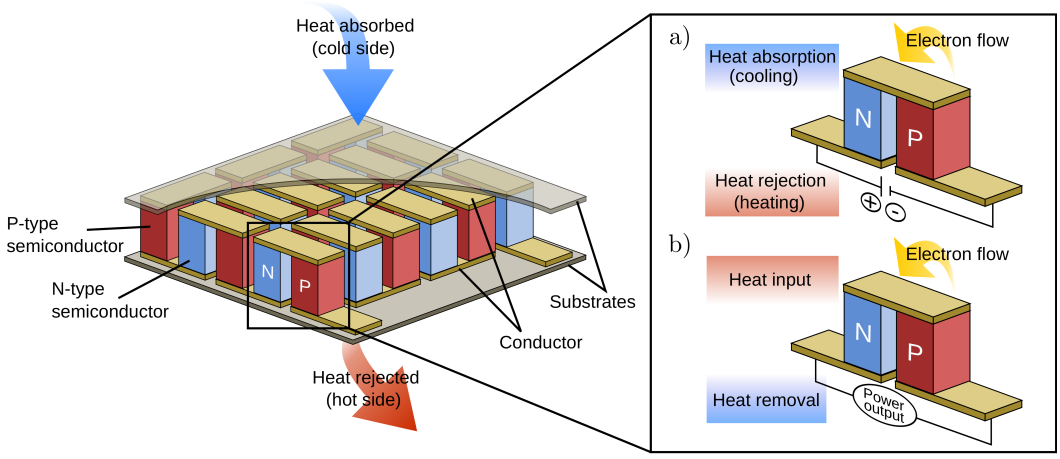


Figure 1.1: Conceptual illustration of a Peltier element / thermoelectric module. P- and n-type semiconductors are connected in series via conductors and either transform (a) electricity into a heat difference or (b) vice versa.

conductivity $\kappa$ should be reduced. In fact, reduction of the lattice thermal conductivity is the only way to reduce the thermal conductivity, since the electronic contribution is strongly correlated with the electrical conductivity. Slack calculated the theoretical minimum of the thermal conductivity for several materials [21]. Second, since the charge carrier mobility is proportional to the electrical conductivity, a high carrier mobility is required for both, n- and p-type, charge carriers [19, 22, 23]. Third, the density of states effective mass $m^*$ should be equal to the free electron mass $m_0$. This relates back to the charge carrier mobilities. Fourth, the optimal band gap is equal or larger than 0.25 eV. This last suggestion is mainly based on calculations by Mahan [22]. Fifth, the effective mass and the thermal conductivity should be independent of the temperature and together with the mobilities also independent of the charge carrier concentration. In general terms, the PGEC concept can be summarized as the idea of a material that conducts temperature like a glass but electrons like a crystal. The PGEC concept led to new ideas for thermoelectric materials, like so-called cage compounds which include for example clathrates [24–28] or skutterudites [29–34]. In cage compounds the thermal conductivity is reduced by void filling atoms that serve as scattering centers for phonons and thereby increase the figure of merit.

Another way of significantly enhancing the figure of merit is nanostructuring [35–37]. Hick and Dresselhaus were one of the first to increase the power factor by quantum wells [38]. This inspired investigations on quantum dots [39–42], quantum wires [43–45], superlattices [46,47] and nanostructuring of thermoelectrics in general [35] and led to reports of record $ZT$ values for complex structures like epitaxial multilayers or quantum dot superlattices [48–50].

Following the idea of nanostructuring and the PGEC concept, the search for – and optimization of – thermoelectrics led to a variety of potential materials [3, 4, 26, 51, 52]. The identification of promising candidates from this vast multitude of materials is key in determining novel thermoelectrics. At the same time, the variety of candidates alone prevents a simple experimental screening. Instead, a combination of theoretical and experimental approaches to study the fundamental mechanisms will be more promising. On the one hand, modern quantum chemical methods allow, for example, the calculation of a material's elec-

tronic structure, which in turn allows the calculation of its transport properties. Combined with a lattice structure prediction, this allows to establish a link between lattice structure, electronic structure and transport properties. On the other hand, nanostructuring poses new challenges for theory. The high surface proportion of nanoparticles, for example, brings the accurate characterization of surfaces into focus. Here, one big challenge is the determination of surface energies, which is a challenging task also experimentally. Thus, it will be necessary to come up with new ideas or to improve on existing methods to describe nanostructured thermoelectric materials.

The aforementioned paragraph summarizes nicely the scope of this thesis, which is twofold. On the one side, first-principles electronic structure methods are applied to study the peculiar properties of skutterudites. The focus here is on the link between lattice and electronic structure (see Sec. 4.1 and Papers A1 and A2) and the influence of filling, doping or exchange of atoms (see Sec. 4.1). A step towards nanostructures is taken by investigation of surfaces, including their lattice structures, electronic structures and energies (see Sec. 4.1 and Papers A3 and A4). On the other side, this thesis is a step towards the application of modern highly-accurate electronic structure methods, like electron correlation methods, to complex structures, such as thermoelectrics or surfaces (see Sec. 4.3 and Papers A4 and A5).

## 1.1 Lead Telluride and Skutterudite Materials as Thermoelectrics

Lead telluride (PbTe) crystallizes in the cubic sodium chloride structure ($Fm\bar{3}m$, no. 225), with a lattice parameter of 6.4384 Å (see Fig. 1.2) and has an indirect energy band gap of 0.31 eV at 300 K [53]. With a relatively high maximal $ZT$ value of 0.8-1 at around 650 K, PbTe is one of the most favored materials for industrial applications and as such its thermoelectric properties are well understood [54, 55].

Inspired by a theoretical study on group-13-doping of PbTe [56], substitutions with Tl led to an improved $ZT$ of about 1.5 at 773 K [57]. To improve the $ZT$ further, research on PbTe focuses mainly on the formation of alloys [58, 59] and nanostructuring [60, 61] with PbTe as parent material. While the former strategy aims mostly at increasing the Seebeck coeffi-

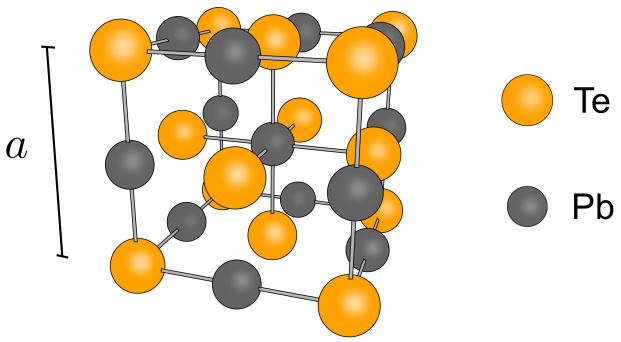


Figure 1.2: Unit cell of PbTe together with its lattice parameter $a$. Telluride atoms (orange circles) occupy the anion positions, lead atoms (gray circles) the kation positions.

cient, the latter aims at lowering the thermal conductivity. Although the thermal conductivity is already quite low in PbTe, promising candidates for further reductions are the so-called LAST-$m$ materials, which are combinations of PbTe and $AgSbTe_2$ that form $AgPb_mSbTe_{2+m}$ ($m \approx 18-22$) alloys with reported $ZT$s of around 1.7 ($\sim 700$ K) [62–65].

Theoretical studies on PbTe consistently describe either the parent material [56, 66–69] or its related doped and alloyed derivatives [70–72]. Thereby, the focus is on the lattice and electronic structure or the thermal conductivity. Special interest for doped and alloyed compounds is on the structural changes (electronic and lattice) and on changes of transport properties by first principles. The challenge of a theoretical description of nanoparticles is tackled by combining theoretical and experimental approaches [73, 74]. However, the applied methods so far are generally confined either to density functional theory (DFT) or molecular dynamics simulations. The influence of electron correlation is neglected. However, the influence of electron correlation is surprisingly large as is analyzed in Sec. 4.3.

Skutterudites comprise another very promising class of thermoelectrics. They were first recorded by Breithaupt and Boebert [75,76] and named after Skutterud (Norway), where they were found in cobalt mines. Skutterudites are binary compounds composed of a transition metal $M$ (e.g. $M =$ Co, Rh, Ir, Fe) and a pnicogen atom $Pn$ (e.g. $Pn =$ P, As, Sb) with the general formula $MPn_3$. Skutterudites crystallize in the cubic, body-centered $CoAs_3$ structure with the space group $Im\bar{3}$. Lattice constants for skutterudites of group-9 transition metals vary from 7.7 Å for $CoP_3$ to 9.3 Å for $IrSb_3$ [77]. $CoSb_3$ and $FeSb_3$ feature lattice constants of about 9.0385 [78] and 9.154 Å (from thin films, see paper A3), respectively. While metal atoms occupy the 8$c$-Wyckoff positions (0.25, 0.25, 0.25), pnicogen atoms occupy the 24$g$-Wyckoff positions (0,$y$,$z$) [75].

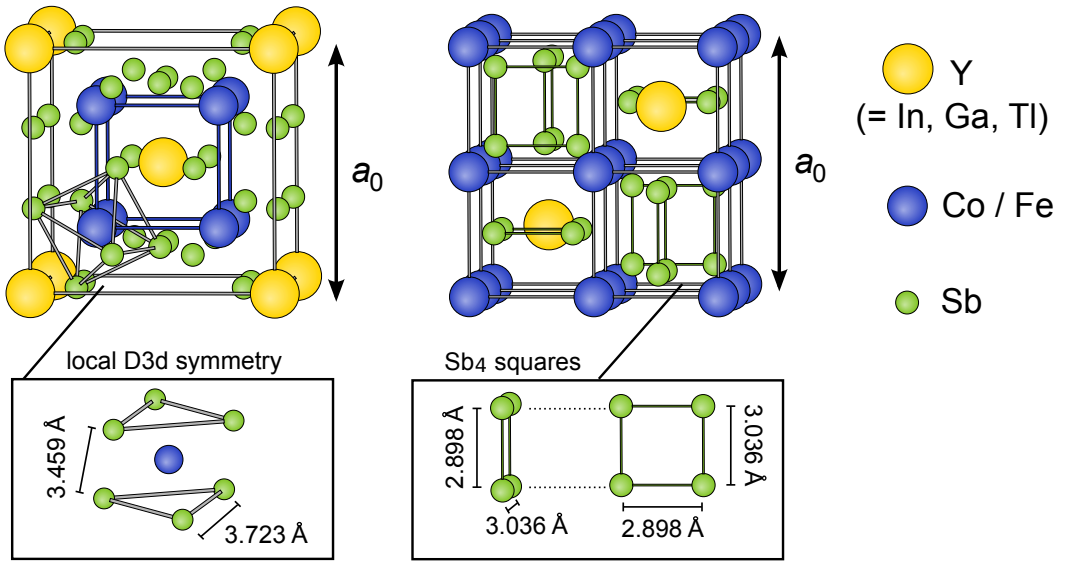


Figure 1.3: Two representations of the skutterudite unit cell with the formula unit $YMPn_3$ (with $M =$ Co, Rh, Ir, Fe; $Pn =$ P, As, Sb; $Y =$ In, Ga, Tl, Ce), where $Y$ is the filling species. $M$ atoms occupy the 8$c$-Wyckoff positions (0.25, 0.25, 0.25), pnicogen atoms occupy the 24$g$-Wyckoff positions (0,$y$,$z$) and filler atoms $Y$ the 2$a$-Wyckoff positions (0, 0, 0). Structural information was obtained within DFT/PBE lattice optimizations [A1].

In general terms, the $CoAs_3$ structure can be seen as a strongly distorted perovskite structure, where the transition metal atoms are coordinated by six pnicogen atoms (see Fig. 1.3). These pnicogen atoms form in total eight distorted octahedrons in the unit cell, with a local $D_{3d}$ symmetry, that are connected via corners. Additionally, pnicogen atoms form $Pn_4$ rectangles, which are sometimes referred to as $Pn_4$ rings.

The aforementioned structural configuration leaves a void in the unit cell center at the $2a$-Wyckoff position that is surrounded by $(MPn_6)_8$ clusters. Due to this void, skutterudites can accommodate filling elements, which makes them ideal PGEC compounds. First syntheses of filled skutterudites date back to the late 1970s and were performed by Jeitschko et al. [79–82]. Nowadays, the focus is mainly on $CoSb_3$ and $FeSb_3$ as parent materials for thermoelectrics. While $CoSb_3$ can be synthesized as a bulk material, $FeSb_3$ is metastable and can only be prepared either by substituting Co with Fe in $CoSb_3$ or from elements by beam epitaxy as thin films (see [83–85] and Paper A2).

Within a simple semiconductor transport model, Slack et al. predicted potential ZT values of $\sim 4$ at 1000 K for $CoSb_3$ skutterudites and, thus, inspired the interest on skutterudites as PGEC materials. Early measurements of thermoelectric properties were performed by Dudkin and revealed promising properties. The parent $CoSb_3$ features a large Seebeck coefficient and a high electron conductivity. However, at the same time it features a high thermal conductivity of about 10 W/mK at 300 K. A significant reduction of the thermal conductivity is achieved by introducing filling atoms. Nowadays a huge variety of fillers exist. Among others, successful examples are lanthanides, actinides, rare earth metals, earth alkali and alkali metals or group-IV elements [32, 86, 87]. Morelli and Meisner reached an increased ZT by reducing the thermal conductivity with a Ce filler in $FeSb_3$ [88]. Further improvements were obtained by Sales et al. [29, 30, 86], Nolas et al. [89] and Tang [90], who reported increased ZT values at high temperatures for p- and n-type $La_{0.9}Fe_3CoSb_{12}$, $Ce_{0.9}Fe_3CoSb_{12}$, $Yb_xCo_4Sb_{12}$ and $Ce_yFe_xCo_{4-x}Sb_{12}$. Other investigations followed, which were more or less systematic [2, 34, 77, 87, 91–97]. Trends derived from these studies show that smaller and heavier filler atoms seem to reduce the thermal conductivity more effectively [26] and that small fractions of filling species are more effective than large ones [98–101]. Apart from this, skutterudites have a natural filling fraction limit up to which they can incorporate a certain filling species. In a first-principles study, Shi et al. suggested that the filling limit depends mainly on two parameters. One is the atom or ion radius of the filling atom, due to the limited space in the voids. The other is the interaction of filler atoms with the pnicogen atoms [102]. However, the study showed that the filling fraction limit is also influenced by the formation of secondary phases between the impurity atoms and one of the host atoms. At a certain filling fraction, the formation of secondary phases can be energetically preferred over further filling of the voids.

In the beginnings, filler atoms were anticipated as independent Einstein oscillators to freely rattle in the voids and thus, by resonant scattering, reduce the phonon mean free path [103]. This is, however, not necessarily the case. Koza et al. showed that vibrational modes of fillers are coherently coupled with the host-lattice dynamics, which leads to eigenmodes of low energy [34]. These eigenmodes are characterized by small group velocities that render them ineffective for heat transport and thus reduce the thermal conductivity.

A reduced thermal conductivity, compared to $CoSb_3$, might also be achieved by substituting cobalt atoms by iron, as indicated by a softening of the phonon modes [85]. However,

from an experimental point of view, characterization of $FeSb_3$ is even more difficult. $FeSb_3$ is metastable and already the preparation is a challenging task and, so far, only possible as thin films [84, 85, 104]. Hence, a detailed thermoelectric characterization was missing. In Paper A2 we have performed such a characterization by a combined theoretical and experimental approach. While the experimental part was performed by my colleagues Daniel et al., I performed the first-principles characterization, employing DFT and Boltzmann transport theory. The combination and the very nice agreement between experimental and theoretical results allow us to draw a conclusive picture of the electronic transport properties of $FeSb_3$. Unfortunately, due to its metastability, $FeSb_3$ will never be applied in a thermoelectric device, besides its favorable electronic properties. However, partly substituting of iron or filling of $FeSb_3$ often leads to stabilized structures without deteriorating much the favorable electronic properties (see Section 4.1). Thus, in any case filling is key for skutterudite derivatives as thermoelectrics.

Besides the evident success to lower the thermal conductivity by filling of skutterudites, a conclusive description of the electronic structure – already for the parent material $CoSb_3$ – is still missing. Although many theoretical and experimental studies exist, uncertainties remain. One example is the size of the energy band gap, which ranges from 0.05 to 0.7 eV, depending on the data source. First optical absorption measurements by Ackermann and Wold revealed no band gap [105]. Singh and Pickett estimated an indirect pseudo-gap of 0.57 eV at the experimental lattice structure by applying the LDA functional within the DFT extended general-potential linearized augmented-plane-wave (LAPW) method [106] and claimed nice agreement with high temperature measurements [107]. Their pseudo-gap is crossed by a single valence band at the $\Gamma$-point that almost reaches up to the conduction bands and that minimizes the actual band gap. This single band features an almost linear dispersion near the Fermi level. By adiabatic, symmetry-conserving displacement of the Sb sublattice, Smith et al. found massless bands (Dirac bands) [108]. Later, with an indirect band gap of 0.55 eV, Caillat et al. confirmed Dudkin's results by resistivity measurements [109]. However, Kurmaev et al. found no band gap by XPS and XES measurements [110] and Arushanov et al. estimated a gap of 0.031 eV by studying the Shubnikov-de Haas effect [111].

Further theoretical investigations estimated band gaps between 0.1 and 0.4 eV and included LDA and PBE calculations with varying codes at different structures or simple band models [110–116]. Despite these studies, the picture remains diverse. In Paper A1 I show that the diversity of results is mainly due to the applied functionals and the underlying skutterudite lattice structure. Both strongly influence the size of the band gap. The band gap size is, in fact, inversely proportional to the lattice parameter. But moreover, the dispersion of the prominent single valence band can be increased or decreased by simply changing the aspect ratio of the $Sb_4$ rectangles (cf. Fig. 1.3). A detailed description is given in Paper A1 and Sec. 4.1.

Besides filling, nanostructuring is another way to significantly enhance the figure of merit [35]. Toprak et al. were one of the first to show its positive effect on $CoSb_3$ skutterudites [117]. Nanostructuring exploits mainly either quantum size effects or enhanced phonon scattering at nanoscale interfaces [35]. From a theoretical point of view nanostructures are difficult to describe. Typical nanoparticles are still too big to be computed by quantum chemical first-principles. Instead theoretical descriptions are often based on classical mechanics or a combination of both. Another way of treating nanoparticles is by considering only parts of the

whole nanosystem. Thus, in such a way and as a first approximation towards nanoparticles, we have investigated surface energies of $CoSb_3$ skutterudites (see Paper A3). By employing Wulff's scheme and the computed surface energies, it is possible to construct the probable shapes of nanocrystals in vacuum.

## 1.2 Towards Electron Correlation in Thermoelectrics and Nanoparticles

Quantum chemical electronic structure theory has come a long way in describing molecules very accurately in the last decades. While Hartree-Fock (HF) theory as a starting point is missing electron correlation, modern electronic structure methods include electron correlation in one way or the other. Some recent developments in this field and a historical overview are summarized, e.g., in the 2012 published Chemical Review issue "Quantum Chemistry 2012" [118]. Besides their apparent success, all of these quantum chemical methods share a common inconvenience. They are nicely applicable to small and medium sized systems but lack the direct transferability to extended systems. Either the application of periodic boundary conditions is challenging or they scale unfavorably with system size (more details on scaling are given in Sec. 2.7).

In principle DFT with common functionals is easily transferred to periodic boundaries and scales quite favorably with system size. At the same time it often features a high accuracy and is therefore widely adopted to solid state tasks [119–121]. However, standard density functionals often describe non-local electron correlation insufficiently. A well known example are weak interactions, like physisorption, where standard DFT functionals tend to underestimate binding energies [122–125]. Another example are surface energies, which apparently depend strongly on the applied exchange-correlation functional [126]. Recently introduced empirical or non-empirical dispersion correction schemes improve greatly and very efficiently on the accuracy [127–131]. Other successful approaches are non-local DFT functionals (e.g., vdW-DF [132] and VV10 [133]) and the recent many-body dispersion (MBD) method by Tkatchenko et al. [134]. All of these dispersion corrections, however, sacrifice partly the first-principles character of the method. The most recent developments beyond DFT, such as doubly-hybrid functionals [135–137], are just becoming available in extended structure codes.

Electron correlation is described more accurately and consistently in wave-function based post-HF methods. Examples are coupled-cluster theory (CC) [138] or Møller-Plesset perturbation theory (MP$n$) [139] of order $n$. Although electron correlation methods often achieve high accuracies, standard implementations of post-HF methods scale unfavorably with the system size and are unfeasible for extended systems [140]. More efficient implementations exploit the local character of the correlation hole and are based on a localized orbital representation.

Stollhoff and Fulde were among the first to employ the idea of localized orbitals in extended systems [141–143]. Their so-called *local ansatz* considered local excitations out of non-orthogonal orbitals. Later, Pulay and Saebø utilized an orthogonal set of localized orbitals and considered excitations into non-orthogonal projected atomic orbitals (PAOs), which represent the virtual space [144–146]. Afterwards, their scheme was implemented by Werner

and Schütz for molecular systems and became part of the MOLPRO program [147, 148]. An extension to solids was performed by Pisani et al. [149, 150], which was implemented in the CRYSCOR code [150, 151]. Stoll invented a slightly different scheme for extended systems [152–155]. His so-called method of increments (MoI) expands the electron correlation energy as a many body expansion and relies on cluster schemes that mimic the infinitely extended solid. In this way, the virtual space is truncated although in principle the MoI allows excitations into the whole virtual space. The advantage of the MoI is the readily applicability of molecular quantum chemistry codes and any implemented size-extensive quantum chemical method. However, the MoI does not necessarily need to rely on cluster schemes to truncate the virtual space. Shukla et al. employed an incremental scheme that, again, relies on PAOs [156]. Another cluster approach is the hierarchical method, which was introduced by Abdurahman et al. [157] and was amended to solids by Manby et al. [158] A more exhaustive overview was recently published by Müller and Paulus [140].

Besides others, the periodic Local-MP2 (LMP2) method and the MoI have both been applied very successfully to describe adsorption or cohesive energies [159–166]. In this thesis I apply the periodic LMP2 method to the test system of group-12 fluorides (see Paper A5). I show that there is a significant electron correlation contribution, which is reflected by the lattice parameter and the cohesive energy and that can be nicely obtained by the periodic LMP2 method (see Paper A5). In a step towards the more complicated thermoelectric material PbTe, I employ the same scheme to determine the electron correlation effects in PbTe (see Sec. 4.3). The PbTe system confirms the same trends as in the group-12 fluoride test cases. The electron correlation again contributes significantly to the cohesive energy and the lattice parameter. Already the LMP2 method achieves exceptional good agreement with experiment.

As such, bulk systems with well defined periodic boundary conditions are relatively straightforward to treat with local electron correlation methods. This remains true as long as the unit cell is small enough. Nanoparticles can be considered as huge molecules and, hence, feature often no periodic boundaries anymore. Then again, typical nanoparticles are usually still too large to be described entirely by quantum chemical methods. However, depending on the property, the description of small size effects can often be approximated by treating only parts of a nanocrystal. A practical example is adsorption, where only the adsorption site is of interest. Similarly, surface energies can be calculated in a slab model with periodic boundaries and still be employed in the Wulff scheme to estimate a nanoparticle's shape in vacuum. However, slab calculations are normally computationally expensive, which in turn allows only DFT computations. Then again, surface energies strongly depend on the applied DFT functional. LDA and generalized gradient approximation (GGA) functionals, for example, might differ by about 50 % with an unclear preference for either of them. This is in fact well reflected for $CoSb_3$ skutterudite surfaces as shown in Paper A3. Local wave function based electron correlation methods are in principle well suited to compute surface energies very accurately. Consequently, in Paper A4, I adapt the MoI to surface energies and compare it to the periodic LMP2 method. As a starting point I choose $MgF_2$ as a propitious test system. However, in principle there are no restrictions – other than the apparent limitations of the local methods – in employing the developed scheme also to other more complicated systems.

Accurately calculated surface energies are interesting for another reason. Measuring sur-

face energies, often involves cleavage of clean planes of single crystals – a very challenging task by itself – and the results are often quite sensitive to temperatures. Hence, measured surface energies often differ by 10 - 40 % already for simple systems [167–170]. Reliable calculated surface energies allow to circumvent difficult experimental setups and measurements.

# Chapter 2

# Theory and Methods

Since the development of quantum mechanics in the mid 1920's [171, 172], many contributors furthered its success with ideas, approximations, different views or approaches. These developments, and technical advances, enabled quantum chemists to solve an ever-growing variety of complex quantum systems including extended systems like the solid state. The underlying fundamental ideas, approximations, and methods applied in this thesis, will be illustrated in the following together with new developments that make even very accurate methods feasible for extended systems. Wherever derivations of the theory are brief, the reader is referred to the references in the text for further inquiries.

## 2.1 Hartree-Fock Theory

In 1926, Schrödinger postulated the existence of a wave function $\Psi$, which respresents a quantum state, and described its time evolution via a partial differential equation [172]. Although Schrödinger's equation, "the mother equation of [quantum] chemistry" (Popelier 2011, [173]), is easily written down as

$$i\frac{\partial}{\partial t}\Psi = \hat{H}\Psi, \tag{2.1}$$

it is difficult to solve for systems that exceed two particles and painfully so for even larger systems. Here, $\Psi$ is a high dimensional, in principle complex function, and $\hat{H}$ is the Hamiltonian that characterizes the state or generates the evolution of the system.

In spite of its complexity, different approaches allow to solve Schrödinger's equation in a reasonable but approximate way. Which approach or approximation to choose depends strongly on the phenomenon to be examined. In the case at hand, the most important applied approximations are of the following: First, relativistic effects are either neglected or incorporated approximately in a pseudopotential approach (for a review on pseudopotentials see e.g. [174] and references therein). Second, the systems at hand are confined to stationary states and are sufficiently described by the time-independent Schrödinger equation. Third, electronic and nuclear degrees of freedom are treated separately within the Born-Oppenheimer approximation [175].

With these aforementioned approximations the Schrödinger equation reduces to the non-relativistic, time-independent, electronic Schrödinger equation

$$\hat{H}^{\mathrm{el}}\Psi^{\mathrm{el}} = E^{\mathrm{el}}\Psi^{\mathrm{el}}, \tag{2.2}$$

where $E^{\text{el}}$ is the electronic energy, $\Psi^{\text{el}}$ is the electronic wave function and

$$\hat{H}^{\text{el}} = -\frac{1}{2}\sum_{i}^{N}\nabla_i^2 - \sum_{i}^{N}\sum_{A}^{M}\frac{Z_A}{r_{iA}} + \frac{1}{2}\sum_{i\neq j}^{N}\frac{1}{r_{ij}}, \tag{2.3}$$

is the electronic Hamiltonian. The first term in Eq. 2.3 denotes the kinetic energy and the last two terms denote the potential energy of the electrons. Here, $N$ is the number of electrons, $M$ is the number of nuclei, $Z$ is the atomic number, $r_{ij}$ is the distance between electrons $i$ and $j$, and $r_{iA}$ is the distance between electron $i$ and nucleus $A$. The following considers only the electronic Hamiltonian, energy and wave functions. Hence, the indices "el" are dropped for simplicity.

Even with the aforementioned approximations, the electron-electron interaction in Eq. 2.3 prevents a direct solution of Eq. 2.2. Thus, in what is commonly summarized as HF theory [176], the electronic wave function $\Psi$ is usually approximated by a single Slater determinant [177, 178]

$$\Psi(\mathbf{x}_1,\mathbf{x}_2,...,\mathbf{x}_N) = \frac{1}{\sqrt{N!}}\begin{vmatrix} \chi_1(\mathbf{x}_1) & \chi_2(\mathbf{x}_1) & \cdots & \chi_n(\mathbf{x}_1) \\ \chi_1(\mathbf{x}_2) & \chi_2(\mathbf{x}_2) & \cdots & \chi_n(\mathbf{x}_2) \\ \vdots & \vdots & \ddots & \vdots \\ \chi_1(\mathbf{x}_N) & \chi_2(\mathbf{x}_N) & \cdots & \chi_n(\mathbf{x}_N) \end{vmatrix} = |\chi_1\chi_2\dots\chi_N\rangle, \tag{2.4}$$

where $n$ is the number of spin orbitals. In general terms, the Slater determinant is an antisymmetric product ansatz for the wave function that obeys the Pauli principle. Here, $\chi_i(\mathbf{x})$ is a single-particle wave function that describes the spatial as well as the spin part of an electron and $\mathbf{x}$ is a variable that incorporates both the spatial coordinate $\mathbf{r}$ and the spin orbital coordinate $\omega$. Thus, a spin orbital $i$ is a product of a spatial orbital $\psi_i(\mathbf{r})$ and a spin function,

$$\chi_i(\mathbf{x}) = \psi_i(\mathbf{r})\begin{cases}\alpha(\omega)\\ \beta(\omega)\end{cases} \qquad \text{with} \qquad i = 1,2,...,n. \tag{2.5}$$

As given by the variational principle, the "best" slater determinant is the one that minimizes the energy. In Dirac notation, this statement is simply

$$E_0 = \min_{\Psi}\langle\Psi|\hat{H}|\Psi\rangle, \tag{2.6}$$

where $E_0$ is the ground state energy and $\Psi$ the Slater determinant that minimizes the electronic energy, i.e. the ground state electronic wave function. By following the variational principle with respect to the choice of the spin orbitals, the HF equation can be derived as

$$f(\mathbf{x}_i)\chi(\mathbf{x}_i) = \epsilon_i\chi(\mathbf{x}_i). \tag{2.7}$$

Solving the HF equation gives the optimal spin orbitals $\chi(\mathbf{x}_i)$ and their corresponding eigen-

values, the orbital energies, $\epsilon_i$. In Eq. 2.7, the Fock operator $f(\mathbf{x}_i)$ is

$$f(\mathbf{x}_i) = -\frac{1}{2}\nabla_i^2 - \sum_{A=1}^{M}\frac{Z_A}{r_{i,A}} + v^{\mathrm{HF}}(\mathbf{x}_i). \tag{2.8}$$

In this so-called mean-field approach, the electron $i$ in spin orbital $\chi_a$ experiences an averaged potential $v^{\mathrm{HF}}(\mathbf{x}_i)$, which is an effective one-electron operator. This HF potential is created by all other electrons in the spin orbitals $\chi_b$ and is given by

$$v^{\mathrm{HF}}(\mathbf{x}_i) = \sum_{\substack{b \\ b\neq a}} \hat{J}_b(\mathbf{x}_i) - \hat{K}_b(\mathbf{x}_i), \tag{2.9}$$

with the Coulomb and exchange operators acting on a spin orbital $\chi_a(\mathbf{x}_1)$ defined by

$$\hat{J}_b(\mathbf{x}_1)\chi_a(\mathbf{x}_1) = \int \chi_b^*(\mathbf{x}_2)\frac{1}{r_{12}}\chi_b(\mathbf{x}_2)\,\mathrm{d}\mathbf{x}_2\;\chi_a(\mathbf{x}_1), \tag{2.10}$$

$$\hat{K}_b(\mathbf{x}_1)\chi_a(\mathbf{x}_1) = \int \chi_b^*(\mathbf{x}_2)\frac{1}{r_{12}}\chi_a(\mathbf{x}_2)\,\mathrm{d}\mathbf{x}_2\;\chi_b(\mathbf{x}_1), \tag{2.11}$$

respectively.

As seen in Eqs. 2.9, 2.10 and 2.11 the HF potential depends on the spin orbitals of all other electrons and the HF equation is non-linear. Because of the non-linearity it must be solved iteratively, which is achieved within the self-consistent-field (SCF) approach. The principle idea of the SCF method is to solve the HF eigenvalue equation (Eq. 2.7) for an initial guess of the spin orbitals, i.e. an initial guess of the potential $v^{\mathrm{HF}}(\mathbf{x}_i)$ and to use this solution subsequently to calculate a new potential $v^{\mathrm{HF}}(\mathbf{x}_i)$. Afterwards, the procedure is repeated until a convergence criterion is fulfilled and self-consistency is achieved. The SCF solution of the HF equation (Eq. 2.7) yields a set of orthonormal spin orbitals $\{\chi_i\}$ with orbital energies $\epsilon_i$. The determinant created by these orbitals is the HF ground state wave function and is the best variational single determinant solution to the ground state.

The spatial part of the spin orbitals in Eq. 2.5 constitutes a molecular orbital. The unknown molecular orbitals $\psi_i(\mathbf{r})$ are usually expanded in a finite set of $K$ atomic orbitals $\phi_\mu$ which are adapted variants of solutions to hydrogen-like atoms and act as a basis

$$\psi_i = \sum_{\mu=1}^{K} C_{\mu i}\phi_\mu, \qquad \text{with} \qquad i = 1,2,...,K. \tag{2.12}$$

Applying these basis functions results in a matrix eigenvalue equation for the expansion coefficients, the so-called Roothaan-Hall equation [179, 180]

$$\mathbf{FC} = \boldsymbol{\varepsilon}\mathbf{SC}, \tag{2.13}$$

where $\mathbf{C}$ is a $K \times K$ square matrix containing the expansion coefficients and $\boldsymbol{\varepsilon}$ is a diagonal matrix containing the corresponding orbital energies $\epsilon_i$. In Eq. 2.13, $\mathbf{F}$ is the Fock matrix and

**S** is the overlap matrix, which are defined as

$$F_{\mu\nu} = \int \phi_\mu^*(\mathbf{r}_1) f(\mathbf{r}_1) \phi_\nu(\mathbf{r}_1) d\mathbf{r}_1, \tag{2.14}$$

$$S_{\mu\nu} = \int \phi_\mu^*(\mathbf{r}_1) \phi_\nu(\mathbf{r}_1) d\mathbf{r}_1. \tag{2.15}$$

## 2.2 Density Functional Theory

While it is obvious, from its initial form, to solve the Schrödinger equation in terms of wave functions, the basic idea of DFT is a different one. In DFT the key quantity is the electron density $\rho$ [181]. Besides that, there remain striking resemblances between DFT and HF theory.

The idea of DFT was first introduced by Thomas [182] and Fermi [183] in 1927/28. However, DFT started its success only after Hohenberg and Kohn contributed their two famous theorems in 1964 [184]. They proved that, first, the ground state electron density $\rho_0$ defines an external potential $v_{\text{ext}}$ uniquely up to an additive constant. Here, the external potential $v_{\text{ext}}$ can refer to the potential arising from the nuclei but it is generally not restricted to Coulomb potentials. Second, the ground state energy $E_0$ is always less or equal to an energy arising from a non-negative trial density $\rho_{\text{t}}$

$$E_0 \leq E[\rho_{\text{t}}]. \tag{2.16}$$

In general terms, the second Hohenberg-Kohn theorem simply justifies the variational principle with respect to the density for DFT. Still up to this point, the challenge remains to find a reasonable accurate representation of the exact electron density of interacting electrons.

Shortly after establishing the Hohenberg-Kohn theorem, Kohn and Sham mapped the system of interacting electrons to a system of non-interacting electrons. This is achieved by introducing an effective potential $v_{\text{eff}}$ that reproduces the exact density. Following their idea, the electronic energy can be written as

$$E[\rho] = \int \rho(\mathbf{r}) v_{\text{ext}}(\mathbf{r}) \mathrm{d}\mathbf{r} + T_{\text{s}}[\rho] + J[\rho] + E_{\text{XC}}[\rho], \tag{2.17}$$

where the first term on the right hand side is the classical electron-nuclei Coulomb interaction with the potential $v_{\text{ext}}(\mathbf{r})$ that arises from the nuclei. $T_{\text{s}}[\rho]$ is the kinetic energy of the system of non-interacting electrons and $J[\rho]$ is the classical Coulomb (Hartree) repulsion of the density with itself. $E_{\text{XC}}[\rho]$ is the so-called exchange-correlation functional and from Eq. 2.17 required to be

$$E_{\text{XC}}[\rho] = T[\rho] - T_{\text{s}}[\rho] + V_{\text{ee}}[\rho] - J[\rho], \tag{2.18}$$

where $V_{\text{ee}}$ is the exact electron interaction energy and $T[\rho]$ is the kinetic energy of the interacting system.

The Hamiltonian of a non-interacting system – in an effective "external" potential $v_{\text{eff}}$ – is separable and, therefore, the exact wave function is a single determinant. This determinant

is constructed from single particle orbitals that are the solutions to the Kohn-Sham equation

$$\left(-\frac{1}{2}\nabla^2 + v_{\text{eff}}(\mathbf{r})\right)\phi_i(\mathbf{r}) = \epsilon_i\phi_i(\mathbf{r}), \tag{2.19}$$

where, from the variational method, the effective potential $v_{\text{eff}}(\mathbf{r})$ is determined to be

$$v_{\text{eff}}(\mathbf{r}) = v_{\text{ext}}(\mathbf{r}) + \frac{\delta J[\rho]}{\delta\rho(\mathbf{r})} + \frac{\delta E_{\text{XC}}[\rho]}{\delta\rho(\mathbf{r})}. \tag{2.20}$$

The orbitals of the non-interacting system are the Kohn-Sham orbitals and their density

$$\rho(\mathbf{r}) = \sum_i^N \phi_i^2(\mathbf{r}), \tag{2.21}$$

reproduces exactly the density of the interacting system. Thus, the kinetic energy of the non-interacting system is

$$T_{\text{s}}[\rho] = \sum_i^N \langle\phi_i| - \frac{1}{2}\nabla^2|\phi_i\rangle. \tag{2.22}$$

Up to this point, the theory is still exact and an exact energy could be calculated from Eq. 2.17 if the correct exchange-correlation energy $E_{\text{XC}}$ was known. However, it is not, and $E_{\text{XC}}$ has to be approximated in practical calculations.

One of the simplest ideas to approximate the exchange-correlation energy $E_{\text{XC}}$ is to apply the exchange-correlation energy of the homogeneous [185] electron gas $\epsilon_{\text{XC}}$ also to inhomogeneous systems,

$$E_{\text{XC}}^{\text{LDA}}[\rho] = \int \rho(\mathbf{r})\epsilon_{\text{XC}}^{\text{LDA}}[\rho]\mathrm{d}\mathbf{r}, \tag{2.23}$$

which is the so-called local density approximation (LDA) [178, 186, 187]. The exchange-correlation energy $E_{\text{XC}}$ of the homogeneous electron gas can be divided into a sum of the exchange and correlation energy $E_{\text{XC}} = E_{\text{X}} + E_{\text{C}}$. While the first is solvable analytically for the homogeneous electron gas, the latter is only so for the high- and low-density limits [181]. For the expression of $\epsilon_{\text{C}}$ in the non-limit region, normally several points are calculated by accurate quantum Monte Carlo methods and interpolated afterwards. Within the LDA approximation, the only correlation functional applied in this thesis is the one generated by Vosko, Wilk and Nusair (VWN) [186].

To exploit the homogeneous electron density for rather inhomogeneous systems is often not the most sensible choice. Thus, to improve on LDA, the GGA is applied. A GGA functional incorporates additionally the gradient of the homogeneous electron density $\nabla\rho$,

$$E_{\text{XC}}^{\text{GGA}}[\rho] = \int \rho(\mathbf{r})\epsilon_{\text{XC}}[\rho, \nabla\rho]\mathrm{d}\mathbf{r}. \tag{2.24}$$

The gradient in $\epsilon_{\text{XC}}$ is thereby included as a separate function in each case and either added or multiplied to $\epsilon_{\text{C}}^{\text{LDA}}$ and $\epsilon_{\text{X}}^{\text{LDA}}$. Various flavors of GGA functionals have been created over the years, of which PBE [188] and PW91 [189] are the ones that have been applied in this

thesis.

Further improvements on the GGA functionals are sometimes achieved in meta-GGA by including also higher order derivatives $\nabla^2\rho$ or, as a different approach, in hybrid functionals by including some of the exact HF exchange $E_{\mathrm{X}}^{\mathrm{HF}}$,

$$E_{\mathrm{XC}}^{\mathrm{hybrid}} = \int \rho(\mathbf{r})\epsilon_{\mathrm{XC}}(\rho,\nabla\rho)\mathrm{d}\mathbf{r} + \zeta E_{\mathrm{X}}^{0}. \tag{2.25}$$

The two hybrid functionals that appear in this work are the B3LYP and B3PW functionals. Hybrid functionals mix exchange and correlation energies from different sources empirically. In both cases the functional is parameterized as

$$E_{\mathrm{XC}}^{\mathrm{B3LYP/B3PW}} = E_{\mathrm{XC}}^{\mathrm{LDA}} + a_0\left(E_{\mathrm{X}}^{\mathrm{HF}} - E_{\mathrm{X}}^{\mathrm{LDA}}\right) + a_{\mathrm{X}}\left(E_{\mathrm{X}}^{\mathrm{GGA}} - E_{\mathrm{X}}^{\mathrm{LDA}}\right) + a_{\mathrm{C}}\left(E_{\mathrm{C}}^{\mathrm{GGA}} - E_{\mathrm{C}}^{\mathrm{LDA}}\right), \tag{2.26}$$

with $a_0 = 0.20$, $a_{\mathrm{X}} = 0.72$, and $a_{\mathrm{C}} = 0.81$ for the three empirical parameters and the Becke 88 functional [190] for $E_{\mathrm{X}}^{\mathrm{GGA}}$. For B3LYP the correlation functional is the Lee, Yang, Parr functional [191] and for B3PW it is the PW91 functional [189].

To be precise, DFT in the form as mentioned above is spin free. However, it is straightforward to include spin. The density is then considered separately for $\alpha$- and $\beta$-spin. They are defined as

$$\rho_\sigma(\mathbf{r}) = N\int |\Psi(\mathbf{r},\sigma,\mathbf{x}_2,...,\mathbf{x}_N|^2, \tag{2.27}$$

with the interpretation that $\rho_\sigma(\mathbf{r})\mathrm{d}^3r$ is the probability of finding an electron of spin $\sigma$ in the volume element $\mathrm{d}^3r$. As for the spin-free DFT, the Hohenberg-Kohn theorems hold, which prove a one-to-one correspondence between spin densities and spin-dependent external potentials $v_{\mathrm{ext},\sigma}(\mathbf{r})$. Then, the Kohn-Sham equations that need to be solved, are spin-dependent. Spin dependent DFT allows directly for the determination of (some) magnetic properties.

## 2.3 Post-Hartree-Fock Methods

Both methods, HF and DFT, are mean-field approaches and approximate the electron-electron interaction as an interaction between a single electron and the potential created by all (other) electrons. As a consequence, the calculation of many-body wave functions is avoided and the computational effort reduces drastically. However, the missing energy contribution, due to the neglect of explicitly interacting electrons, is often crucial in cases that require a certain accuracy. While a systematic improvement on DFT is difficult, it is straightforward in HF. There are two essentially different approaches that are based on the HF results. While one improves on the wave function, the other improves on the Hamiltonian. In the following, the underlying ideas of post-HF treatment are presented together with a short introduction of the electron correlation methods that are relevant in this work.

### 2.3.1 The Exact Wave Function

As described in Sec. 2.1, the HF method creates a set $\{\chi_i\}$ of $n$ spin orbitals. The resulting ground state

$$|\Psi_0\rangle = |\chi_1 \chi_2 \dots \chi_N\rangle, \tag{2.28}$$

is a single determinant constituted by the $N$ spin orbitals that minimize the electronic energy, where $N$ is the number of electrons. In principle, however, there are $\binom{n}{N}$ possible slater determinants that could be formed from the $n$ spin orbitals. These slater determinants are conveniently described by taking the HF ground state as a reference. Then, by using the indices $a, b, c, \dots$ to denote the occupied, and $r, s, t, \dots$ to denote the unoccupied spin orbitals, a singly excited determinant is one where an electron, from an occupied spin orbital $\chi_a$ in the HF ground state, has been moved to an unoccupied (or virtual) spin orbital $\chi_r$,

$$|\Psi_a^r\rangle = |\chi_1 \chi_2 \dots \chi_r \chi_b \dots \chi_N\rangle. \tag{2.29}$$

Doubly, triply, …, and $N$-tuply excited determinants are defined accordingly.

By considering excited determinants as an $N$-electron basis, any antisymmetric function can be expanded in terms of all unique determinants formed from a complete set of one-particle functions [176]. Since all possible determinants can be described by reference to the HF determinant, the exact wave function is

$$|\Phi\rangle = c_0|\Psi_0\rangle + \sum_{ar} c_a^r |\Psi_a^r\rangle + \sum_{\substack{a<b \\ r<s}} c_{ab}^{rs} |\Psi_{ab}^{rs}\rangle + \sum_{\substack{a<b<c \\ r<s<t}} c_{abc}^{rst} |\Psi_{abc}^{rst}\rangle + \dots, \tag{2.30}$$

where $\Psi_a^r$ is the notation introduced in Eq. 2.29. Accordingly, $\Psi_{ab}^{rs}$ indicates doubly-excited determinants and so forth. The sums are over all unique pairs of occupied $a < b$ and virtual $r < s$ spin orbitals, respectively.

Eq. 2.30 shows that in principle the exact wave function can be expanded in the infinite set of $N$-electron determinants $\{\Psi_i\} = \{|\Psi_0\rangle, |\Psi_a^r\rangle, |\Psi_{ab}^{rs}\rangle, \dots\}$ and, consequently, the exact eigen energies of the ground and excited states within the Born-Oppenheimer approximation can be obtained by the Hamiltonian matrix elements $\langle\Psi_i|\hat{H}|\Psi_j\rangle$. Unfortunately, dealing with infinitely large basis sets is hard in practice, hence the basis set expansion is truncated. Within the Hilbert space spanned by the truncated basis, the best possible approximation of the system in general includes all excited determinants. This is called a full configuration interaction (CI) calculation. The difference between the full CI energy $E_{\text{FCI}}$ at the basis set limit and the HF energy $E_{\text{HF}}$ is the so-called correlation energy

$$E_{\text{corr}} = E_{\text{FCI}} - E_{\text{HF}}. \tag{2.31}$$

Unfortunately, the number of determinants that have to be included in a full CI calculation is extremely large even for small systems and a minimal basis set. There are several truncation schemes that consider only a manageable number of determinants. According to which Slater determinants are included the methods are either size extensive or not [192]. A method is size extensive if it scales correctly with the number of particles in the system (more details on the concept of size extensivity is for example given in Ref. [192]). Examples

of methods based on Eq. 2.30 are the configuration interaction (CI) [193] and the coupled cluster (CC) [192] method. The coupled cluster method was applied in this work and will be explained briefly in the next section.

### 2.3.2 Coupled Cluster Theory

Any truncated CI method is not size extensive. That is one of its great disadvantages which makes it impractical for extended systems. The CC theory, on the other hand, expands the wave function in terms of products of excited determinants and is size extensive [192, 194, 195]. Thus, the CC wave function $\Psi_{\mathrm{CC}}$ is

$$\Psi_{\mathrm{CC}} = e^{\hat{T}}\Psi_0, \tag{2.32}$$

where $\Psi_0$ is the normalized Hartree-Fock ground state wave function and the operator $e^{\hat{T}}$ is defined by the Taylor-series expansion

$$e^{\hat{T}} = 1 + \hat{T} + \frac{\hat{T}^2}{2!} + \frac{\hat{T}^3}{3!} + \ldots = \sum_{k=0}^{\infty} \frac{\hat{T}^k}{k!}, \qquad \text{with} \qquad \hat{T} = \hat{T}_1 + \hat{T}_2 + \ldots + \hat{T}_N, \tag{2.33}$$

In Eq. 2.33 $N$ is the number of electrons and $\hat{T}_i$ are the operators that create all $i$-th excited Slater determinants

$$\hat{T}_1\Psi_0 = \sum_{a}^{\mathrm{occ}}\sum_{r}^{\mathrm{vir}} t_a^r \Psi_a^r, \qquad \text{and} \qquad \hat{T}_2\Psi_0 = \sum_{a<b}^{\mathrm{occ}}\sum_{r<s}^{\mathrm{vir}} t_{ab}^{rs}\Psi_{ab}^{rs}. \tag{2.34}$$

By considering the rules for integrals of products of excited determinants and the HF reference determinant [176], and by exploiting Brillouin's theorem, the CC energy is

$$\begin{aligned} E_{\mathrm{CC}} &= \langle\Psi_0|\hat{H}|\left(1 + \hat{T}_1 + \hat{T}_2 + \frac{1}{2}\hat{T}_1^2\right)\Psi_0\rangle \\ &= E_0 + \sum_{a<b}^{\mathrm{occ}}\sum_{r<s}^{\mathrm{vir}}\left(t_{ab}^{rs} + t_a^r t_b^s - t_a^s t_b^r\right)(\langle ab|rs\rangle - \langle ab|sr\rangle), \end{aligned} \tag{2.35}$$

where $\langle ab|rs\rangle$ is a shorthand writing for the two-electron integrals. Thus, in principle the CC energy is obtained by merely calculating the two electron integrals and the single and double excitation coefficients, the so-called amplitudes ($t_a^r$, $t_b^s$, $t_{ab}^{rs}$, ...). However, the amplitudes have to be determined by solving the projected coupled cluster equations. These equations are obtained by projecting on the left with the entire set of $m$-tuply excited determinants, where $m$ is the highest order excitation included in $\hat{T}$ e.g.

$$\langle\Psi_0|\hat{H}e^{\hat{T}}|\Psi_0\rangle = E_{\mathrm{CC}}, \tag{2.36}$$

$$\langle\Psi_a^r|\hat{H}e^{\hat{T}}|\Psi_0\rangle = E_{\mathrm{CC}}\langle\Psi_a^r|e^{\hat{T}}|\Psi_0\rangle, \tag{2.37}$$

$$\langle\Psi_{ab}^{rs}|\hat{H}e^{\hat{T}}|\Psi_0\rangle = E_{\mathrm{CC}}\langle\Psi_{ab}^{rs}|e^{\hat{T}}|\Psi_0\rangle. \tag{2.38}$$

Then, this set of coupled equation, in which again higher order excitations contribute, has to be solved. Once more, this is computationally quite expensive. A variety of truncation schemes exist that make calculations feasible. A common applied and quite reliable trun-

cation scheme is the CCSD(T) method [196]. In CCSD(T), single and double excitations are included in the CC expansion, while triple excitations are treated by higher order perturbation theory (MP4, MP5). But instead of using the perturbation amplitudes for the wave function correction, the CC amplitudes are applied.

### 2.3.3 Perturbation Theory

In perturbation theory, the electron correlation contribution is determined by introducing a perturbation term in the Hamiltonian. Perturbation theory was first established by Rayleigh and Schrödinger (RS) [197, 198] and further applied to many-electron systems by Møller and Plesset (MP) [139].

From the RS perturbation theory, the sum of the leading energy term $E_0$ and the first-order correction $E_1$ equal the HF energy

$$E_{\mathrm{HF}} = E_0 + E_1. \tag{2.39}$$

To improve on the HF result, at least perturbation theory of second order (MP2) has to be considered. The second order perturbation term is

$$E_0^{(2)} = \sum_{\substack{a<b \\ r<s}} \frac{|\langle ab|rs\rangle - \langle ab|sr\rangle|^2}{\varepsilon_a + \varepsilon_b - \varepsilon_r - \varepsilon_s}, \tag{2.40}$$

where $a$ and $b$ indicate occupied spin-orbitals, $r$ and $s$ indicate virtual spin-orbitals and $\varepsilon_a$, $\varepsilon_b$, $\varepsilon_r$ and $\varepsilon_s$ indicate the corresponding energies. From RS perturbation theory, higher order corrections to the energy may also be derived. Stopping the perturbation expansion at second order is often referred to as MP2.

## 2.4 The Solid State and Periodic Boundary Conditions

To a first approximation, crystals can be regarded as infinitely extended systems that feature a certain structural unit periodically. In other words, systems in the solid state feature a translational symmetry. This translational symmetry corresponds to the set of vectors

$$\mathbf{T} = u\,\mathbf{a}_1 + v\,\mathbf{a}_2 + w\,\mathbf{a}_3, \tag{2.41}$$

where $\mathbf{a}_i$ are three non-coplanar basis vectors that define a primitive unit cell and $u$, $v$ and $w$ are integer values including zero. For many physical properties it is very convenient to additionally introduce the so-called reciprocal lattice. The reciprocal lattice vectors are defined analogously to the basis vectors in direct space (Eq. 2.41) by

$$\mathbf{K} = h\mathbf{b}_1 + k\mathbf{b}_2 + l\mathbf{b}_3, \tag{2.42}$$

and obey

$$e^{i\mathbf{K}\cdot\mathbf{T}} = 1. \tag{2.43}$$

The integer values $h$, $k$, $l$ are the so-called Miller indices [199] and demonstrate one advantage of introducing the reciprocal lattice. Each $\mathbf{k}$-vector with $\mathbf{k} = h\mathbf{b}_1 + k\mathbf{b}_2 + l\mathbf{b}_3$ and integer values of $h,k,l$ is a surface normal to the surface $(hkl)$. This will again be of interest in the next section. Eq. 2.43 shows that two vectors $\mathbf{k}$ and $\mathbf{k}'$ in reciprocal space, which differ only by a lattice vector $\mathbf{K}$, are equivalent. Hence, only $\mathbf{k}$-vectors in a reference cell, the so-called first Brillouin zone (BZ), need to be considered.

Wave functions that should reflect the translational symmetry of the crystal are required to obey Bloch's theorem [200]

$$\hat{T}\varphi(\mathbf{r},\mathbf{k}) = \varphi(\mathbf{r}+\mathbf{T},\mathbf{k}) = e^{i\mathbf{k}\cdot\mathbf{T}}\varphi(\mathbf{r},\mathbf{k}), \tag{2.44}$$

and are called Bloch functions

$$\varphi(\mathbf{r},\mathbf{k}) = e^{i\mathbf{k}\cdot\mathbf{r}}\zeta(\mathbf{r}), \tag{2.45}$$

with $\zeta(\mathbf{r}+\mathbf{T}) = \zeta(\mathbf{r})$, where $\hat{T}$ is a translation operator that corresponds to the direct lattice vector $\mathbf{T}$.

In solid state computations, the single-particle wave functions which are the solutions to the mean-field approaches discussed in Section 2.2 and 2.1, are called crystalline wave functions $\psi_i(\mathbf{r},\mathbf{k})$. They are usually approximated by a linear combination of Bloch functions (see e.g. [201–204])

$$\psi_i(\mathbf{r},\mathbf{k}) = \sum_\mu c_{\mu i}(\mathbf{k})\varphi(\mathbf{r},\mathbf{k}), \tag{2.46}$$

where the coefficients $c_{\mu i}(\mathbf{k})$ are obtained by solving the coupled set of matrix equations self-consistently. Exemplary for HF and analogously to Eq. 2.13, the coupled set of matrix equations are

$$F(\mathbf{k})C(\mathbf{k}) = S(\mathbf{k})C(\mathbf{k})E(\mathbf{k}). \tag{2.47}$$

Eq. 2.47 has to be solved for each value of $\mathbf{k}$ separately. Consequently, these equations yield $\mathbf{k}$-dependent energies. The energy plotted against $\mathbf{k}$ yields the electronic band structure. Usually, a high-symmetry path through the $\mathbf{k}$-space is plotted as representative for the whole band structure.

The Bloch functions themselves are again expanded in a set of basis functions, of which there are two types:

- *Atomic Orbitals*

$$\varphi_i(\mathbf{r},\mathbf{k}) = \frac{1}{\sqrt{N}}\sum_{\mathbf{T}} e^{ik\cdot\mathbf{T}}\phi_i(\mathbf{r}-\mathbf{r}_A-\mathbf{T}), \tag{2.48}$$

  where $N$ is the normalization, $i$ indicates the atomic orbital in the unit cell and $\mathbf{r}_A$ are the coordinates of atom $A$ in the reference cell on which the atomic orbital $\phi_i$ is centered. In practice, the atomic orbitals are normally themselves linear combinations of products of Gaussian functions and solid harmonics [205].

  One big advantage of atomic orbitals is the similarly accurate description of the va-

lence as well as of the core region of atoms in the crystal. This allows to perform all-electron calculations. Unfortunately, atomic basis sets introduce a basis set superposition error (BSSE) and general orthogonality is lost. Another benefit, however, is the possibility to exploit locality of atomic orbitals and, thus, to apply correlation methods to solids very effectively.

- *Plane Waves*

$$\varphi_i(\mathbf{r},\mathbf{k}) = \frac{1}{\sqrt{N}} \sum_{\mathbf{K}} a_{\mathbf{K},i}\, e^{i\mathbf{r}\cdot(\mathbf{k}+\mathbf{K})}, \tag{2.49}$$

where **K** is a reciprocal lattice vector. The size of the plane wave basis is usually determined by a single energy cutoff parameter equal to a certain kinetic energy $E_{\text{cutoff}} > \frac{\mathbf{k}^2+\mathbf{K}^2}{2}$.

Plane waves are in principle the natural choice for periodic functions. Unfortunately, a huge number of plane waves is necessary to describe the nodal structure of the wave functions in the core region [206]. For that reason, plane wave codes usually apply pseudopotentials that approximate the core region up to a certain distance and reproduce the exact all-electron wave function at the valence region.

To exploit the advantages of each basis set expansion, both have been applied in this work. Plane wave computations have been performed by applying the VASP code [207–211], and atomic basis set computations have been performed by applying the CRYSTAL program [212, 213].

## 2.5 Electronic Structure and Surfaces

While the preceding section only briefly mentioned that introducing a reciprocal lattice has certain advantages, this section explains how. The reciprocal space vector **k** itself, for example, has two main interpretations [214]. First, **k** is identified as a wave vector and, therefore, connected with a momentum $\mathbf{p} = \hbar\mathbf{k}$. Second, **k** labels the irreducible representation of the translation group according to which a corresponding wave function transforms.

Whichever interpretation is adopted, for each value of **k** there is a corresponding energy eigenvalue $E$ as obtained from Eq. 2.47. The resulting dependence of $E$ on the **k**-vector is called dispersion and the plot of $E(\mathbf{k})$ versus **k** is called the band structure. Since any **k**-vector outside of the first BZ can be translated back into the first BZ, it is sufficient to plot the band structure solely for the first BZ. The bandwidth of a single band is determined by its highest and lowest level. The Fermi level defines the highest occupied energy level, up to which a band structure is filled. The number of states incorporated in a volume element d**k** within the first BZ is given by the density of states

$$D_i(E) = \frac{2}{V_{\text{BZ}}} \int_{\text{BZ}} \delta(E - E_i(\mathbf{k}))\ \mathrm{d}\mathbf{k}, \tag{2.50}$$

where the integral is over the whole BZ, $V_{\text{BZ}}$ is the volume of the BZ and $E_i$ is the $i$-th band energy.

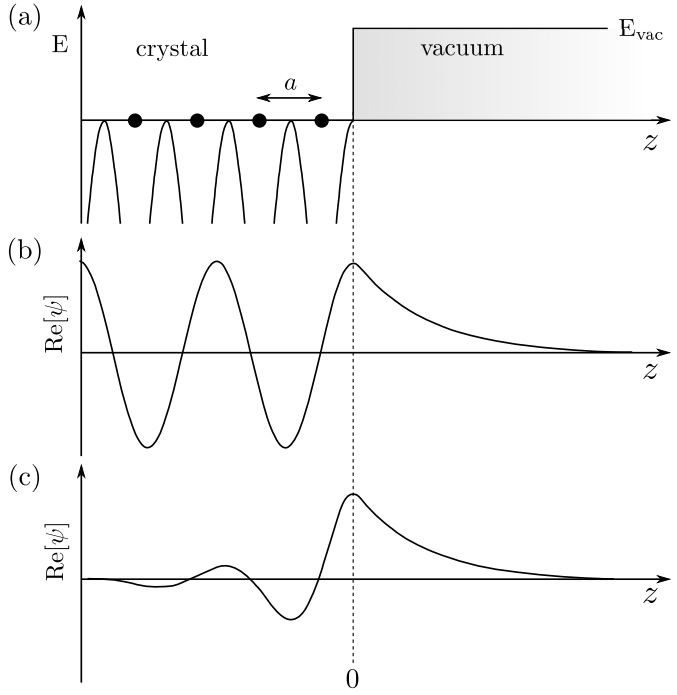


Figure 2.1: Schematic illustration of surface states in one-dimension: (a) the periodic potential of the crystal and the vacuum energy level; (b) real part of a bulk state at the surface decays exponentially into the vacuum; (c) real part of a surface state localized at the surface.

In the preceding discussions, crystals were considered to be ideal and infinitely extended in three dimensions. This approximation is reasonable as long as the number of atoms close to defects and surfaces is small. However, in nanoparticles, for example, the surface to bulk ratio increases and surfaces can play a significant role.

In a computer simulation, a surface is defined as the truncation of the ideal crystal in one dimension. Two common ways to model surfaces are cluster schemes or slab models, where a slab is a unit cell that is infinite in two dimensions and either separated by a vacuum gap or truncated in the third dimension.

The truncation of the periodic potential in one dimension leads to new solutions in the electronic Schrödinger equation which can be illustrated conveniently in a simple one-dimensional model. For a one-dimensional potential as shown in Fig 2.1a there exist two principle solutions to the one-dimensional single-electron Schrödinger equation, which are shown in Fig. 2.1b and 2.1c. The first solution corresponds to a bulk state with a typical Bloch character in the bulk and an exponential decay into the vacuum. The second solution is localized at the surface and decays exponentially in both directions, into the bulk and into the vacuum. This solution corresponds to a surface state.

Surface states can be identified by decomposing the general **k**-vector in the BZ into components that are either parallel or perpendicular to the surface plane

$$\mathbf{k} = \mathbf{k}_{\parallel} + \mathbf{k}_{\perp}, \tag{2.51}$$

and by projecting all eigenvalues $\epsilon_i(\mathbf{k}_{\parallel} + \mathbf{k}_{\perp})$ onto $\mathbf{k}_{\parallel}$ independent of $\mathbf{k}_{\perp}$. Then, for a set of

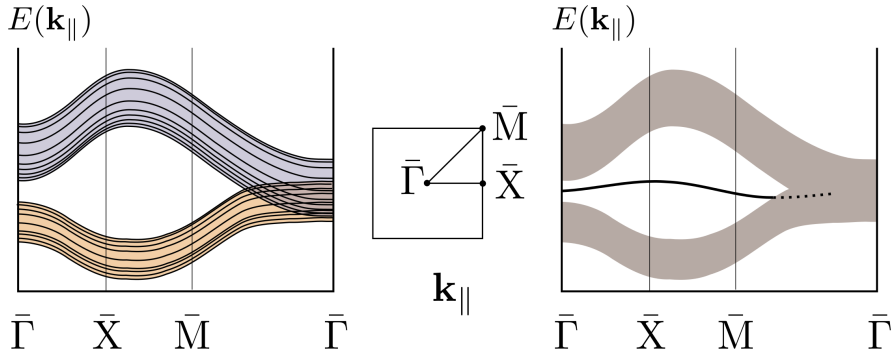


Figure 2.2: Schematic visualization of a surface projected bulk band structure (left) together with a surface state (right). In the left diagram several bands, each for a different value of $\mathbf{k}_\perp$, are plotted which form the projected bulk continuum (filled area) in the right diagram. The band structure is that of a hypothetical cubic crystal. Its BZ is shown together with the characteristic k-points (middle).

$\mathbf{k}_\perp$ along a path in the corresponding two-dimensional BZ, the partitioned bulk bands form allowed energy intervals. These intervals constitute the surface projected bulk band structure, called bulk continuum. A schematic representation is given in Fig. 2.2. Comparing the bulk continuum and the surface band structure reveals the surface states which lie in the forbidden (gap) regions. It should be mentioned that there is a distinction between a surface state and a so-called resonance state. The latter features an enhanced amplitude close to the surface but propagates deep into the bulk, like a Bloch wave.

## 2.6 Solid State Electron Transport

One of the biggest challenge for quantum chemists is the combination of microscopic quantum mechanical properties with macroscopic classical properties. One prominent example is charge transport, i.e. electron movements. However, promisingly efficient and reasonably accurate results are often obtained when quantum chemical and classical theories are combined in a statistical way. A well-performing example is the combination of Boltzmann theory with modern quantum chemical electronic structure theory. It allows the calculation of macroscopic transport properties. An introduction to the theory is given in the following.

### 2.6.1 The Boltzmann Equation

The probability of finding an electron of state $\mathbf{k}$ in a crystal at a position $\mathbf{r}$ at a time $t$ is completely described by the distribution function $f(\mathbf{r},\mathbf{k},t) = |\Psi(\mathbf{r},\mathbf{k},t)|^2$. Unfortunately, to find an exact solution of $f(\mathbf{r},\mathbf{k},t)$ for a many-electron system is not possible because of the high dimensionality of the problem and because of many-body interactions. Nonetheless, transport properties can be obtained in a statistical way by treating electrons in a crystal as a quasi-particle gas and applying Boltzmann theory. Although developed for gases originally, Boltzmann theory has many applications in physics and works surprisingly well for crystals, too. In fact, Boltzmann theory works well if the considered charge carriers can be assigned to an energy $E$ and, therefore, also a group velocity $\nabla_\mathbf{k} E$ [215]. A detailed overview and

derivation of the Boltzmann theory can be found in the following References [199, 215–220]. Here, the focus is solely on electron transport in solids.

The first assumption in Boltzmann transport theory is that electrons in equilibrium follow the Fermi-Dirac distribution function

$$f_0(\mathbf{r},\mathbf{k}) = \frac{1}{1+e^{\frac{E(\mathbf{k})-\mu(\mathbf{r})}{k_B T(\mathbf{r})}}}, \tag{2.52}$$

where $E(\mathbf{k})$ is the quasi-particle energy, $\mu(\mathbf{r})$ is the chemical potential, $k_B$ is the Boltzmann constant and $T(\mathbf{r})$ is the temperature. Although electrons instantaneously move from a state $\mathbf{k}$ to a state $\mathbf{k}'$ by collisions, this motion is not included in the Fermi-Dirac function. However, the mean distribution of electrons in equilibrium is always given by the Fermi-Dirac function, as long as there are no external forces. Including external forces via a perturbation $f_1$ the near-equilibrium distribution function $f$ can be written as

$$f = f_0 + f_1. \tag{2.53}$$

For a stationary near-equilibrium distribution, the Boltzmann equation is

$$\frac{\mathrm{d}f}{\mathrm{d}t} = 0 = \frac{\partial f}{\partial t} + \nabla_{\mathbf{r}} f \cdot \frac{\partial \mathbf{r}}{\partial t} + \nabla_{\mathbf{k}} f \cdot \frac{\partial \mathbf{k}}{\partial t} + \left.\frac{\partial f}{\partial t}\right|_{scat.}, \tag{2.54}$$

where the explicit time-evolution of $f$ due to scattering processes is written separately in the last term. The time evolution of $\mathbf{k}$, in the second to last term, is identified with the force $\mathbf{F}_\mathrm{e} = \frac{1}{\hbar}\frac{\partial \mathbf{k}}{\partial t}$ that acts on the electrons. By additionally assigning the velocity $\mathbf{v}$ and momentum $\mathbf{p}$

$$\mathbf{p} = \hbar\mathbf{k}, \qquad \mathbf{v} = \frac{\partial \mathbf{r}}{\partial t} = \frac{1}{\hbar}\nabla_{\mathbf{k}} E(\mathbf{k}), \tag{2.55}$$

to the electrons and by assuming a steady-state ($\frac{\partial f}{\partial t} = 0$) the Boltzmann equation simplifies to

$$\nabla_{\mathbf{r}} f \cdot \mathbf{v} + \frac{1}{\hbar}\nabla_{\mathbf{k}} f \cdot \mathbf{F}_\mathrm{e} + \left.\frac{\partial f}{\partial t}\right|_{scat.} = 0. \tag{2.56}$$

The two terms on the left-hand side of Eq. 2.56 are called drift terms. While the first one contains the electron drift due to a temperature gradient and the chemical potential, the second one describes the external forces. Here, the external force is the Lorentz force acting on the electrons

$$\mathbf{F}_\mathrm{e} = -e\,(\mathbf{E} + \mathbf{v} \times \mathbf{B}), \tag{2.57}$$

where $\mathbf{E}$ is the electric field, $\mathbf{B}$ is the magnetic field and $e$ is the electron charge.

The position dependence of the distribution function $\nabla_{\mathbf{r}} f$ is contained solely in the position dependence of the chemical potential $\mu(\mathbf{r})$ and the temperature $T(\mathbf{r})$. Provided that the position (or the temperature dependence) of the perturbation is small compared to the equilibrium distribution function $\nabla_{\mathbf{r}} f_1 \ll \nabla_{\mathbf{r}} f_0$, the gradient of the near-equilibrium distribution

function is

$$\begin{aligned}\nabla_{\mathbf{r}} f(\mathbf{r},\mathbf{k},t) \approx \nabla_{\mathbf{r}} f_0(\mathbf{r},\mathbf{k}) &= \frac{e^{\frac{E(\mathbf{k})-\mu(\mathbf{r})}{k_B T(\mathbf{r})}}}{\left(1+e^{\frac{E(\mathbf{k})-\mu(\mathbf{r})}{k_B T(\mathbf{r})}}\right)^2} \frac{1}{k_B T(\mathbf{r})} \left(\nabla_{\mathbf{r}}\mu(\mathbf{r}) + \frac{E(\mathbf{k})-\mu(\mathbf{r})}{T}\nabla_{\mathbf{r}} T(\mathbf{r})\right) \\ &= -\frac{\partial f_0(\mathbf{r},\mathbf{k})}{\partial E(\mathbf{k})}\left(\nabla_{\mathbf{r}}\mu(\mathbf{r}) + \frac{E(\mathbf{k})-\mu(\mathbf{r})}{T}\nabla_{\mathbf{r}} T(\mathbf{r})\right). \end{aligned} \tag{2.58}$$

Applying the definitions in Eq. 2.53 and 2.55 and neglecting the contribution of $\mathbf{E}\cdot\nabla_{\mathbf{k}} f_1$ in the linear approximation, the term describing the external forces in Eq. 2.56 becomes

$$\begin{aligned}\frac{1}{\hbar}\nabla_{\mathbf{k}} f(\mathbf{r},\mathbf{k},t)\cdot\mathbf{F}_{\mathrm{e}} &= -\frac{e}{\hbar}\left[\nabla_{\mathbf{k}} f_0\cdot\mathbf{E} + \nabla_{\mathbf{k}} f_0\cdot(\mathbf{v}\times\mathbf{B}) + \underbrace{\nabla_{\mathbf{k}} f_1\cdot\mathbf{E}}_{=0 \text{ (lin. approx.)}} + \nabla_{\mathbf{k}} f_1\cdot(\mathbf{v}\times\mathbf{B})\right] \\ &= -\frac{e}{\hbar}\left[\frac{\partial f_0}{\partial E}\nabla_{\mathbf{k}} E\cdot\mathbf{E} + \underbrace{\frac{\partial f_0}{\partial E}\nabla_{\mathbf{k}} E\cdot(\nabla_{\mathbf{k}} E\times\mathbf{B})}_{=0} + \frac{1}{\hbar}\nabla_{\mathbf{k}} f_1\cdot(\nabla_{\mathbf{k}} E\times\mathbf{B})\right] \\ &= -\frac{e}{\hbar}\left[\frac{\partial f_0}{\partial E}\nabla_{\mathbf{k}} E\cdot\mathbf{E} + \frac{1}{\hbar}\nabla_{\mathbf{k}} f_1\cdot(\nabla_{\mathbf{k}} E\times\mathbf{B})\right]. \end{aligned} \tag{2.59}$$

## 2.6.2 Constant Relaxation Time Approximation

The last term on the left-hand side of Eq. 2.56 regards the scattering of electrons and is in general very complex to solve. Thus, certain approximations are necessary. As a first one, scattering is considered to occur instantaneously. In other words, upon scattering electrons change their state $\mathbf{k}$ but not their position $\mathbf{r}$. Often the scattering mechanisms are summarized in the so-called collision operator $\hat{C}$. Thus, the scattering term is

$$\left.\frac{\partial f}{\partial t}\right|_{scatt} = \hat{C} f. \tag{2.60}$$

In general, collision rates can be obtained by applying Fermis golden rule (see e.g. Refs. [215–217]). However, these calculations are demanding. A often reasonable approximation is to keep the relaxation-time $\tau$ constant. This approach is the so-called constant relaxation time approximation (RTA) in which Eq. 2.60 is approximated by a difference quotient

$$\hat{C} f \approx \frac{f(\mathbf{r},\mathbf{k},t+\tau) - f(\mathbf{r},\mathbf{k},t)}{\tau}. \tag{2.61}$$

Assuming that after a time $\tau$ the perturbed system relaxes into the ground state, $f(\mathbf{r},\mathbf{k},t+\tau) = f_0(\mathbf{r},\mathbf{k})$, Eq. 2.61 simplifies to

$$\hat{C} f \approx \frac{f_0(\mathbf{r},\mathbf{k}) - f(\mathbf{r},\mathbf{k},t)}{\tau} = -\frac{f_1(\mathbf{r},\mathbf{k},t)}{\tau}. \tag{2.62}$$

In general terms, the RTA can be understood in the following way. A system out of equilibrium will relax back into equilibrium exponentially after a characteristic relaxation time

$\tau$

$$f_1 = f_1(0)e^{-\frac{t}{\tau}}. \tag{2.63}$$

The RTA turns out to be applicable where scattering is isotropic and/or elastic. An example for isotropic scattering is acoustic phonon scattering, one for elastic scattering is impurity scattering [215].

The aforementioned prerequisites allow to treat scattering processes in a much simplified way and allows to find an approximated solution to the Boltzmann equation. Inserting Eq. 2.58 and 2.59 into Eq. 2.56 yields the linearized Boltzmann equation within the RTA approximation

$$\begin{aligned} 0 = & - \frac{\partial f_0}{\partial E}\left(\nabla_{\mathbf{r}}\mu(\mathbf{r}) + \frac{1}{T}\nabla_{\mathbf{r}}T(\mathbf{r})\right)\cdot\mathbf{v} \\ & - \frac{e}{\hbar}\left[\frac{\partial f_0}{\partial E}\nabla_{\mathbf{k}}E\cdot\mathbf{E} + \frac{1}{\hbar}(\nabla_{\mathbf{k}}E\times\mathbf{B})\cdot\nabla_{\mathbf{k}}f_1\right] - \frac{f_1(\mathbf{r},\mathbf{k},t)}{\tau}. \end{aligned} \tag{2.64}$$

### 2.6.3 Transport Coefficients

In a steady state non-equilibrium process, transport properties can be derived by applying the Onsager method which relates flows and forces in thermodynamic systems that are out of equilibrium. The method is described in great detail in Refs. [218,221]. Here, the equations of this theory are only utilized to derive the electronic transport properties.

In the presence of an electric field and a temperature gradient, the electric current density $\mathbf{j}$ and the heat current density $\mathbf{j}_Q$ are

$$\mathbf{j} = L_{11}\mathbf{E} - L_{12}\nabla_{\mathbf{r}}T, \tag{2.65}$$

$$\mathbf{j}_{\mathrm{Q}} = L_{21}\mathbf{E} - L_{22}\nabla_{\mathbf{r}}T, \tag{2.66}$$

where $L_{11}$, $L_{12}$, $L_{21}$ and $L_{22}$ are the transport tensors which, for isotropic systems, reduce to scalars. From Eq. 2.65 the electrical conductivity $\sigma$ can be extracted. Without a temperature

Table 2.1: Summary of transport tensor relations as derived by Onsager's theory (see e.g. Refs. [218,221]). In this theory the $L_{ij}$s refer to the transport tensors as given in Eqs. 2.65 and 2.66.

| Name | Symbol | Onsager Relation |
|---|---|---|
| electrical conductivity | $\sigma$ | $L_{11}$ |
| Seebeck coefficient | $S$ | $(L_{11})^{-1}L_{12}$ |
| Peltier coefficient | $\Pi$ | $(L_{11})^{-1}L_{21}$ |
| thermal conductivity | $\kappa$ | $L_{22} - \left[L_{12}L_{21}(L_{11})^{-1}\right]$ |
| electronic part of thermal conductivity | $\kappa_0$ | $L_{22}$ |

gradient $\nabla_{\mathbf{r}} T = 0$, Eq. 2.65 yields

$$\mathbf{j} = L_{11}\mathbf{E}, \tag{2.67}$$

which is Ohm's law with $L_{11} = \sigma$. Similarly, relations for the Seebeck coefficient $S$, the Peltier coefficient $\Pi$, and the thermal conductivity $\kappa$ can be derived. A summary is given in Table 2.1.

A system $f(\mathbf{r},\mathbf{k},t)$ out of equilibrium will automatically result in moving charge carriers and subsequently in an electric current $\mathbf{j}$. The differential electric current is given by the product of the charge $e$, the velocity $\mathbf{v}$, and the charge carrier density per unit volume $\mathrm{d}n$ [219]

$$\mathrm{d}\mathbf{j} = e\mathbf{v}\mathrm{d}n, \qquad \text{with} \qquad \mathrm{d}n = 2\frac{1}{(2\pi)^3}\, f(\mathbf{r},\mathbf{k},t)\,\mathrm{d}^3k. \tag{2.68}$$

By considering that only the perturbation $f_1(\mathbf{r},\mathbf{k},t)$ will have an influence on the net current and by integrating Eq. 2.68 the electric current density is

$$\mathbf{j} = \frac{2e}{\hbar(2\pi)^3}\int_{\mathrm{BZ}} \nabla_{\mathbf{k}} E(\mathbf{k})\, f_1(\mathbf{r},\mathbf{k},t)\,\mathrm{d}^3k. \tag{2.69}$$

**Electrical Conductivity**

In general terms, the electrical conductivity, $\sigma$, is a measure of how well a system conducts electrons due to an applied electric field. The relation was first published by Ohm and is, therefore, often referred to as Ohm's law [222] as given by

$$\mathbf{j} = \sigma\mathbf{E}. \tag{2.70}$$

Assuming that there is no temperature gradient $\nabla_{\mathbf{r}} T = 0$, no magnetic field $\mathbf{B} = 0$, and the system is homogeneous $\nabla_{\mathbf{r}}\mu = 0$, Eq. 2.64 can be rewritten in terms of $f_1$ and inserted into Eq. 2.69, which yields the electric current of a single electron band $i$,

$$\mathbf{j}_i = -\frac{2e^2\tau}{\hbar^2(2\pi)^3}\left[\int_{\mathrm{BZ}} \frac{\partial f_0}{\partial E_i}\,\nabla_{\mathbf{k}} E_i(\mathbf{k})\nabla_{\mathbf{k}} E_i(\mathbf{k})\,\mathrm{d}^3k\right]\mathbf{E}, \tag{2.71}$$

where $\nabla_{\mathbf{k}} E_i(\mathbf{k})\nabla_{\mathbf{k}} E_i(\mathbf{k})$ is in principle a tensor product. By comparing Eq. 2.71 and Eq. 2.70, the electrical conductivity tensor for a single electron band $i$ is

$$\sigma_i = -\frac{2e^2\tau}{\hbar^2(2\pi)^3}\int_{\mathrm{BZ}} \frac{\partial f_0}{\partial E_i}\,\nabla_{\mathbf{k}} E_i(\mathbf{k})\nabla_{\mathbf{k}} E_i(\mathbf{k})\,\mathrm{d}^3k. \tag{2.72}$$

The total electric current is the sum of all partial electric currents of each band. In conclusion, the total electrical conductivity is

$$\sigma = \sum_i \sigma_i. \tag{2.73}$$

**Seebeck Coefficient**

The Seebeck effect describes the voltage drop $U$ that will occur if two dissimilar materials are connected via two junctions in an open circuit and experience at the same time a temperature difference $\Delta T$ at these junctions [13, 16, 182]. This temperature difference defines the magnitude of the voltage drop via a proportionality constant, the Seebeck coefficient $S$, defined by

$$U = S\Delta T. \tag{2.74}$$

More generally, the Seebeck coefficient is the combination of the individual Seebeck coefficients of the two involved materials. To determine a single material dependent Seebeck coefficient, we assume for one of the two materials $S = 0$.

Assuming there are no external electromagnetic fields and the position dependence of the chemical potential can be neglected, $\nabla_{\mathbf{r}}\mu(\mathbf{r}) = 0$, Eq. 2.64 can be solved for the perturbation $f_1$ and inserted into Eq. 2.69. Then, the electric current for a single band $i$ is

$$\mathbf{j}_i = -\frac{2e\tau}{\hbar^2(2\pi)^3 T}\nabla_{\mathbf{r}}T(\mathbf{r})\int_{\mathrm{BZ}}\frac{\partial f_0}{\partial E_i}\,\nabla_{\mathbf{k}}E_i(\mathbf{k})\cdot\nabla_{\mathbf{k}}E_i(\mathbf{k})\,\left(E_i(\mathbf{k})-\mu\right)\,\mathrm{d}^3k. \tag{2.75}$$

Additionally, with Eq. 2.65 the electric current is

$$\mathbf{j} = -L_{12}\nabla_{\mathbf{r}}T = -\sigma S\,\nabla_{\mathbf{r}}T = -\sum_i \sigma_i S_i \nabla_{\mathbf{r}}T, \tag{2.76}$$

where $\sigma_i$ is the $i$-th electronic band electrical conductivity and $S_i$ the $i$-th band Seebeck coefficient. By comparing Eq. 2.75 and Eq. 2.76 the $i$-th band Seebeck coefficient is

$$S_i = \frac{2e\tau}{\hbar^2(2\pi)^3 T\sigma_i}\int_{\mathrm{BZ}}\frac{\partial f_0}{\partial E_i}\,\nabla_{\mathbf{k}}E_i(\mathbf{k})\,\nabla_{\mathbf{k}}E_i(\mathbf{k})\,\left(E_i(\mathbf{k})-\mu\right)\,\mathrm{d}^3k. \tag{2.77}$$

From Eq. 2.76 the total Seebeck coefficient is

$$S = \sigma^{-1}\cdot\sum_i \sigma_i S_i. \tag{2.78}$$

### 2.6.4 Boltzmann Transport by Quantum Chemical First Principles

The application of the aforementioned approximations and formulas reduces the challenge of calculating transport tensors to a challenge of computing first and second derivatives of the electronic bands. Modern quantum chemical solid-state codes, like VASP [207–211] or CRYSTAL [212, 213], allow to calculate the electronic band structure of large systems very efficiently. This efficient calculation of the band structure is exploited very elegantly in the BOLTZTRAP code by Madsen and Singh [223].

In general terms, the BOLTZTRAP code employs star functions, that maintain the space group symmetry, to expand the band energies in a Fourier series. This Fourier expansion is performed such that it reproduces the calculated band energies exactly and, additionally, suppresses oscillations between data points by minimizing a roughness function (for more details on the Fourier expansion, the reader is referred to Ref. [223] and references therein).

This analytical representation of the band-structure allows a straightforward calculation of band-structure related properties.

In BoltzTraP the integrations are completely performed within energy space. In this case, the electrical conductivity tensor, as shown in Eq. 2.72, is expressed as

$$\sigma_{\alpha\beta}(i,\mathbf{k}) = e^2 \tau_{i,\mathbf{k}} v_\alpha(i,\mathbf{k}) v_\beta(i,\mathbf{k}), \qquad \text{with} \qquad v_\alpha(i,\mathbf{k}) = \frac{1}{\hbar}\frac{\partial E_{i,\mathbf{k}}}{\partial k_\alpha}. \tag{2.79}$$

The energy projected conductivity tensor is

$$\sigma_{\alpha\beta}(E) = \frac{1}{N}\sum_{i,\mathbf{k}} \sigma_{\alpha\beta}(i,\mathbf{k}) \frac{\delta(E - E_{i,\mathbf{k}})}{\mathrm{d}E}, \tag{2.80}$$

where $N$ is the number of sampled $\mathbf{k}$-points. After projection on the energy the transport tensors are calculated by

$$\sigma_{\alpha\beta}(T;\mu) = (L_{11})_{\alpha\beta} = \frac{1}{\Omega}\int \sigma_{\alpha\beta}(E)\left(-\frac{\partial f_\mu(T;E)}{\partial E}\right)\mathrm{d}E, \tag{2.81}$$

$$(L_{12})_{\alpha\beta} = \frac{1}{eT\Omega}\int \sigma_{\alpha\beta}(E)(E-\mu)\left(-\frac{\partial f_\mu(T;E)}{\partial E}\right)\mathrm{d}E, \tag{2.82}$$

$$S_{mn} = \left(L_{11}^{-1}\right)_{\alpha m}(L_{12})_{\alpha n}. \tag{2.83}$$

For different values of $T$ and $\mu$, Eqs. 2.81 - 2.83 yield the transport tensors with respect to the temperature and the chemical potential. While the electrical conductivity depends on the relaxation-time $\tau$, the Seebeck coefficient will be relaxation-time independent if $\tau$ is direction independent.

## 2.7 Local Correlation Methods in the Solid State

Electron correlation methods are computationally expensive. Already in HF, the computational effort scales formally with $\mathcal{O}(N^4)$, where $N$ is the relative measure of the system size. However, by storing integrals in memory and applying efficient implementations the scaling is rather $\mathcal{O}(N^3)$ or even lower. $\mathcal{O}(N^3)$ is also in the range of formal scaling of DFT and generally accepted as a bearable price-performance ratio. Higher-level correlation methods often trade higher accuracy for time. Already MP2 formally scales between $\mathcal{O}(N^4)$ and $\mathcal{O}(N^5)$, depending on the implementation and the number of occupied orbitals. MP3 and CCSD formally scale with $\mathcal{O}(N^6)$ and MP4 and CCSD(T) scale between $\mathcal{O}(N^6)$ and $\mathcal{O}(N^7)$. Additional cost-intensifying complications occur due to periodic boundaries.

To reduce computational costs, efficient electron correlation schemes often exploit the locality of the correlation hole. They are based on localized orbitals that allow to expand the correlation energy with respect to the distance and to apply sophisticated truncation schemes. Additional techniques, like density-fitting, reduce the computational effort further. An overview about state-of-the art developments has been given in the introduction (Chapter 1). Interested readers are referred to Refs. [140, 151, 224, 225].

In this work, two local electron correlation schemes, the MoI [152–155, 226] and the periodic LMP2 [149, 151, 201], are applied for surface computations. Although their main con-

cepts will be described briefly in the following section, the focus is on the adaption of these methods to surface energies. A more exhaustive overview on periodic LMP2 and MoI is given elsewhere [140, 151].

### 2.7.1 Periodic Local MP2 for Surface Energies

The molecular orbitals obtained by solving the HF equations are in principle delocalized and extend over the whole crystalline unit cell or the whole molecule. However, if an atomic orbital basis is employed, the HF molecular orbitals can be localized to a limited spatial region, e.q. to bonds or to atoms, by a unitary transformation. In practice the localization is achieved by either the Foster-Boys [227, 228] or Pipek-Mezey [229] localization scheme. The CRYSCOR code [149, 151] is based on the localized crystalline orbitals of the the periodic HF solution obtained by the CRYSTAL code [212, 213]. Bloch functions in CRYSTAL are localized by applying Wannier orbitals and the Boys localization scheme [230, 231].

The idea of the LMP2 method by Pulay and Saebø [144–146] is to exploit the exponential decay of Hamilton matrix elements between excited determinants and the ground state determinant [144, 146, 232], with respect to the distance of the localized orbitals. This is achieved by localizing and truncating the virtual space. The localized virtual space is non-orthogonal and obtained by projecting out the occupied space directly from the atomic orbital basis, i.e. creating PAOs. Then, the LMP2 correction to the HF wave function is

$$|\Psi^{(1)}\rangle \quad = \quad \frac{1}{2} \sum_{(\boldsymbol{ij})\in P} \sum_{(\boldsymbol{ab})\in[\boldsymbol{ij}]} T_{\boldsymbol{ab}}^{\boldsymbol{ij}} |\Phi_{\boldsymbol{ij}}^{\boldsymbol{ab}}\rangle, \tag{2.84}$$

where $\Phi_{\boldsymbol{ij}}^{\boldsymbol{ab}}$ are doubly excited determinants and $T_{\boldsymbol{ab}}^{\boldsymbol{ij}}$ are the corresponding amplitudes. In Eq. (2.84), the labels $(\boldsymbol{i},\boldsymbol{j})$ indicate pairs of occupied Wannier functions (WFs) obtained from a truncated list $P$, in which the first WF $\boldsymbol{i}$ is located in the reference unit cell and the second WF $\boldsymbol{j}$ is restricted within a given distance to the first WF $\boldsymbol{i}$. Bold indices combine the index within the unit cell and the translation (lattice) vector $\boldsymbol{i}=i\mathscr{I}$, according to the notation of Ref. [149]. The labels $(\boldsymbol{a},\boldsymbol{b})$ indicate pairs of mutually non-orthogonal virtual PAOs. The sum is confined to the pair-domain $[\boldsymbol{ij}]$ of PAOs that are spatially close to at least one of the WF $\boldsymbol{i}$ or $\boldsymbol{j}$. This truncation of the virtual space reduces the computational cost of the periodic LMP2 method to linear scaling with respect to the supercell size. A schematic illustration of the method is given in Fig. 2.3.

Many properties, like cohesive, adsorption, or surface energies, are obtained by computing the difference of a system and its constituting parts. Constrained excitation domains, like PAO, often bear the practical challenge to describe the different parts of a system with an equally sized virtual space as employed for the whole system (see Fig. 2.4). In general terms, this problem can be identified as a BSSE, which is also present in other methods, but becomes critical within the local approximation due to the truncation of the virtual space.

The BSSE prevents a straightforward application of the LMP2 method to relaxed surfaces. As apparent from Fig. 2.4a and 2.4b, truncating a bulk in one dimension leads automatically to differently sized excitation domains. Domain consistency is ensured by reintroducing atoms at their former positions and by transforming them into ghosts. Ghost atoms contribute no electronic or nuclear charge but possess the same basis set as the former atoms

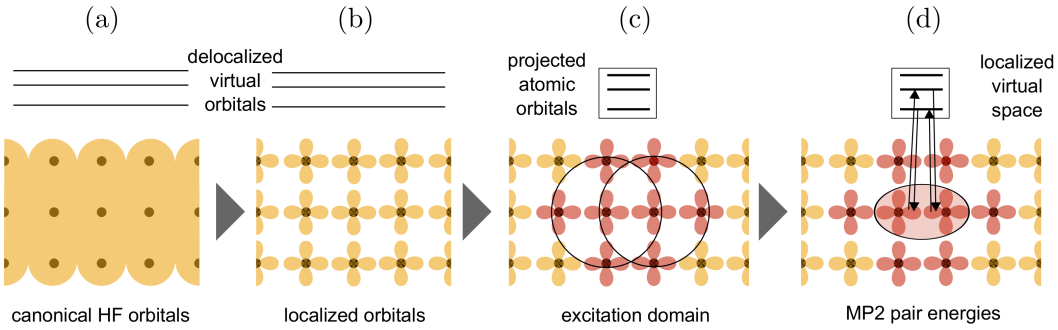


Figure 2.3: Schematic illustration of the periodic LMP2 method. The procedure is as follows: (a) First, HF orbitals (yellow) are obtained from an SCF calculation. (b) The HF orbitals are localized (yellow clubs). (c) PAOs are created by projecting out the occupied orbitals of an excitation domain. All orbitals (yellow clubs) that belong to nuclei (black dots) within a certain radius of a given nuclei (large black circles) are included in the excitation domain. (d) Pair energies are calculated for pairs of orbitals and summed up for the total energy.

and, thus, compensate missing PAOs (shown in Fig. 2.4c). However, introducing ghost atoms is meaningful only for unrelaxed slab structures, since ghost atoms can not be relaxed.

The following remarks demonstrate the procedure for calculating surface energies with consistent excitation domains. In general, the surface energy, $E_{\text{surface}}$ is

$$E_{\text{surface}} = \frac{1}{2\Lambda}\left(E_{\text{slab}} - n E_{\text{bulk}}\right), \tag{2.85}$$

where $E_{\text{bulk}}$ is the bulk energy per unit cell, and $E_{\text{slab}}$ is the slab energy, $n$ is the number of bulk units that appear in the slab unit cell and $\Lambda$ is the slab surface. Eq. (2.85) can be partitioned into a HF and a post-HF (i.e. electron correlation) term,

$$\begin{aligned} E_{\text{surface}} &= E^{\text{HF}}_{\text{surface}} + E^{\text{corr}}_{\text{surface}} \\ 2\Lambda E_{\text{surface}} &= E^{\text{HF}}_{\text{slab}} + E^{\text{corr}}_{\text{slab}} - n\left(E^{\text{HF}}_{\text{bulk}} + E^{\text{corr}}_{\text{bulk}}\right). \end{aligned} \tag{2.86}$$

In an LMP2 treatment the term on the right-hand side of Eq. 2.86 is

$$2\Lambda E^{\text{LMP2}}_{\text{surface}} = E^{\text{CP,rlx}}_{\text{slab}} - n E_{\text{bulk}}, \tag{2.87}$$

where $E_{\text{bulk}}$ is the LMP2 energy of the bulk. $E^{\text{CP,rlx}}_{\text{slab}}$ is the counterpoise corrected (CP) LMP2 energy of a relaxed slab with an equivalently sized excitation domain as in the bulk. Unfortunately, $E^{\text{CP,rlx}}_{\text{slab}}$ is not directly accessible. Consequently, Eq. 2.87 is reformulated as

$$2\Lambda E^{\text{LMP2}}_{\text{surface}} = \Delta E^{\text{rlx}} + E^{\text{CP,urlx}}_{\text{slab}} - n E_{\text{bulk}}, \tag{2.88}$$

where $E^{\text{CP,urlx}}_{\text{slab}}$ is the CP corrected, unrelaxed slab energy corresponding to the same excitation domain as in the bulk, and $\Delta E^{\text{rlx}}$ is the relaxation energy. The relaxation energy can be approximated as

$$\Delta E^{\text{rlx}} \approx E^{\text{rlx}}_{\text{slab}} - E^{\text{unrlx}}_{\text{slab}}, \tag{2.89}$$

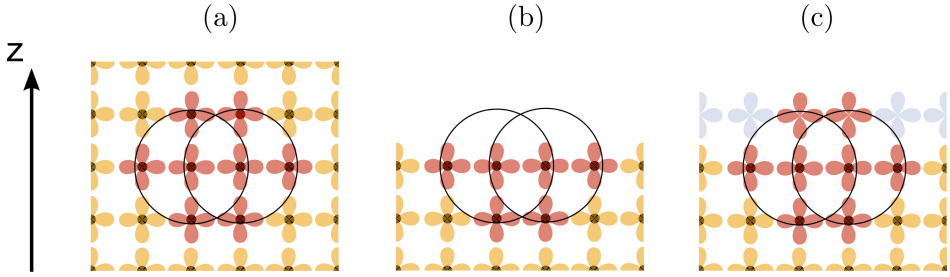


Figure 2.4: Schematic view on a two-dimensional CRYSCOR domain construction. Red orbitals indicate the excitation domain. Starting from a bulk domain (a) a slab is created by truncating the bulk in one dimension (b). This leads likewise to a truncation of the excitation domain. (c) Inconsistencies in the excitation domains are prevented by reintroducing orbitals at the former atom positions (ghost atoms, blue orbitals).

where $E_{\text{slab}}^{\text{rlx}}$ and $E_{\text{slab}}^{\text{unrlx}}$ are the CP uncorrected energies of the relaxed and unrelaxed slab. Eq. 2.89 is an approximation, since in the CP uncorrected slabs, atoms at top layers miss coordination partners and create less PAOs. In conclusion, the BSSE corrected MP2 surface energy in a CRYSCOR calculation of a relaxed slab is

$$E_{\text{surface}}^{\text{MP2}} = \frac{1}{2A}\left(E_{\text{slab}}^{\text{CP,unrlx}} + E_{\text{slab}}^{\text{rlx}} - E_{\text{slab}}^{\text{unrlx}} - nE_{\text{bulk}}\right). \tag{2.90}$$

## 2.7.2 Method of Increments for Surface Energies

In the MoI the electron correlation energy is expanded in terms of correlation contributions of groups of localized HF orbitals. In this context, these orbital groups are called *centers* and can be localized at atoms, ions, molecules or bonds. The correlation contribution arising from a single center is a *1-body* or *one-center* increment,

$$\epsilon_i \quad = \quad E_i - E_{\text{HF}}. \tag{2.91}$$

The correlation contribution arising from two centers, subtracted by the one-center contribution, is a *2-body* or *two-center* increment,

$$\Delta\epsilon_{ij} \quad = \quad E_{ij} - E_{\text{HF}} - \epsilon_i - \epsilon_j = \epsilon_{ij} - \epsilon_i - \epsilon_j. \tag{2.92}$$

Here, $E_i$ is the correlation energy from the localized orbitals of group $i$, $E_{ij}$ the correlation energy from the localized orbitals of the group $i$ and $j$, and $E_{\text{HF}}$ is the HF energy. Higher-order increments are defined accordingly.

The total electron correlation energy is obtained by summing up the contributions of all centers,

$$E_{\text{corr}}^{\text{solid}} = \sum_i \epsilon_i + \frac{1}{2}\sum_{i\neq j}\Delta\epsilon_{ij} + \frac{1}{6}\sum_{i\neq j\neq k}\Delta\epsilon_{ijk} + \ldots, \tag{2.93}$$

where $\Delta\epsilon_{ijk}$ is a three-center increment. The index $i$ sums over all atoms in the unit cell,

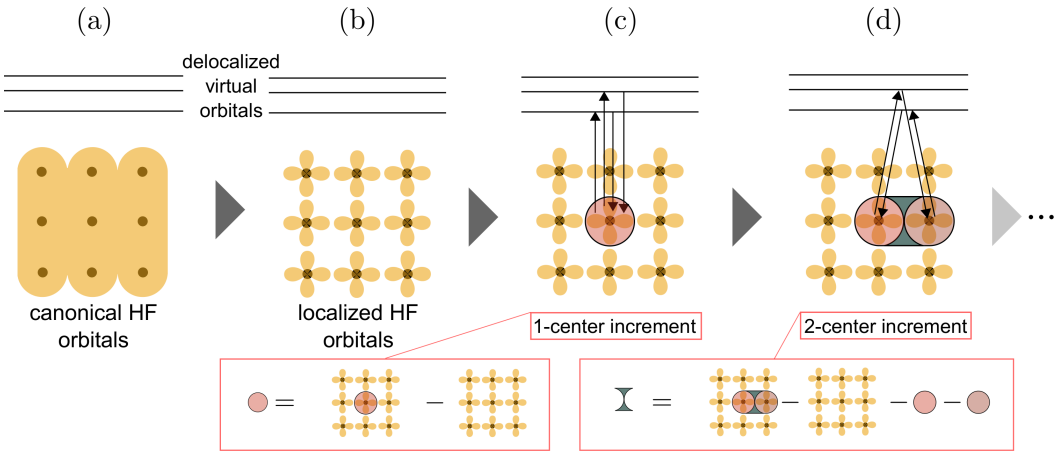


Figure 2.5: Schematic illustration of the MoI in a cluster. The procedure is as follows: (a) First, HF orbitals (yellow) are obtained from an SCF calculation. (b) The HF orbitals are localized (yellow clubs). (c) A group of orbitals (center) is defined. For a one-center increment, orbitals are correlated solely at this center. (d) For a two-center increment, orbitals of two centers are correlated. The complete sum of all correlation contribution yields the exact correlation energy.

while indices $j,k,\ldots$ sum also over atoms outside the unit cell. In principle, Eq. 2.93 sums up to the exact electron correlation energy. However, the effort to compute the complete sum is even higher than to directly calculate the full system. Fortunately, the expansion can be truncated because increments typically decrease rapidly with the inter-center distance and the order of the increments. Often, a small number of one- and two-center increments is enough to obtain more than 97 % of the total electron correlation energy. The general MoI procedure is shown pictorially in Fig. 2.5.

The MoI is conveniently applied to compute adsorption energies by introducing so-called interaction increments according to the adsorption energy [163, 166]. Similar to an interaction increment, a surface increment $\sigma$ is defined as the difference of an increment in HF the slab and an increment in the bulk. Thus, the 1-body and 2-body surface increments are defined as

$$\sigma_i = \epsilon_i^{\text{slab}} - \epsilon_i^{\text{bulk}}, \tag{2.94}$$

$$\sigma_{ij} = \Delta\epsilon_{ij}^{\text{slab}} - \Delta\epsilon_{ij}^{\text{bulk}}. \tag{2.95}$$

Higher-order increments are defined accordingly. The index $i$ runs over all localized orbital groups in the unit cell of a slab and the index $j$ runs over all the other localized orbital groups, not necessarily in the same unit cell. $\epsilon_i^{\text{slab}}$ is the $i$-th increment in the slab that corresponds to the $i$-th increment in the bulk. For 1-body increments the correspondence between slab and bulk increments is one-to-one. However, 2-body and higher order increments may vary in their inter-center distance of bulk and slab increments, due to the different nuclear positions in relaxed surfaces.

Thus, the incremental correlation contribution to the surface energy is the sum over all

surface increments

$$E_{\text{surface}}^{\text{corr}} = \sum_i \omega_i \sigma_i + \sum_{ij} \omega_{ij} \sigma_{ij} + \sum_{ijk} \omega_{ijk} \sigma_{ijk} + \ldots, \tag{2.96}$$

where $\omega$ refers to the weighting factors, i.e. how often the specific increment occurs.

Equally to increments, pair-energies in LMP2 can be summed up with respect to certain centers. Although such sums of pair-energies allow to compare results of the MoI and LMP2 directly, they are not exactly the same as increments in the MoI. The main difference is in their embedding. While LMP2 employs full periodic boundaries, the MoI obtains increments from embedded clusters that mimic the infinitely extended system. Although an embedding introduces a certain embedding error compared to the periodic treatment, the advantage of the MoI over other local correlation methods is the possibility to directly apply large basis sets in combination with any size-extensive method.

# Chapter 3

# Models and Computational Specifications

This work combines many approaches for theoretical descriptions of solid state materials and surfaces. The computational requirements differ for each property of interest. This section summarizes the applied computational parameters and the applied models. For the theoretical studies, that are presented in Papers A1 - A5, computational parameters are summarized in the respective publication. This section is rather an extension than a repetition of these parameters.

## 3.1 Computational Parameters

Generally, if not stated otherwise, plane wave DFT calculations were performed by employing the VASP 5.3.3 program package together with the GW projector augmented wave (PAW) potentials [207–211]. Electronic structure properties for thermoelectric material were generally computed by applying the PBE exchange-correlation functional [188]. Electronic wave functions were expanded to an energy cutoff of 350 eV. k-point grids were Γ-centered and were constructed automatically via the Monkhorst-Pack scheme. Thermoelectric transport properties and the electronic density of states were calculated on a 28x28x28 k-point mesh. Such a dense k-point mesh is necessary to ensure converged electronic properties. For structure relaxations a 8x8x8 k-point mesh was sufficient.

The full structure relaxation was performed by applying the RMM-DIIS quasi-Newton algorithm [233] together with a Gaussian smearing with a smearing factor of 0.001 eV and a force convergence criterion of $10^{-2}$ eV/Å$^2$. Further decreasing the smearing factor has no effect on the minimum structure. The electronic density of states were calculated by applying the tetrahedron method with Blöchl corrections [211]. Sampling of the band structures was performed along high-symmetry paths in the Brillouin zone. The DFT calculations were either performed spin polarized or unpolarized. However, transport properties were obtained from the unpolarized ground state within the limits of Boltzmann theory (see Sec. 2.6) and the constant relaxation time approximation as implemented in the BOLTZTRAP code [223].

Self-consistent atomic basis set computations for the PbTe were performed by applying the CRYSTAL14 program package [212,213]. Pb was described by an energy-consistent scalar-relativistic effective core potential that simulates its chemically inactive [Kr] $4d^{10}4f^{14}$ core [234] together with the corresponding cc-pVDZ (8s6p6d)/[4s3p2d] basis set [235]. The Te atom was described by a core potential of similar quality that simulates the chemically in-

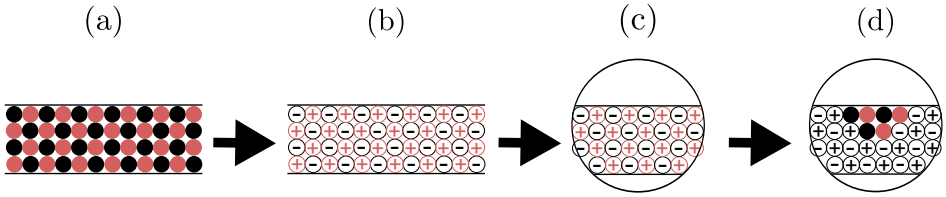


Figure 3.1: Illustration of the embedding scheme that is applied in the incremental cluster method. The scheme is as follows: Atoms in the periodic slab (a) are replaced by formal point charges (b). The infinite array of point charges is truncated at a certain cut-off radius (c). Subsequently the quantum mechanically treated cluster replaces the formal point charges at the center (d).

active [Ar] $3d^{10}$ core together with the corresponding cc-pVDZ (8s6p6d)/[4s3p2d] basis set [236]. Unfortunately, the computational demands of the LMP2 method made it necessary to enlarge the effective core potential of Te such that it described the [Kr] $4d^{10}$ core. The corresponding (6s6p)/[4s4p] (VQZ quality) basis set was employed [237].

Shrinking factors of 12 were employed for the Monkhorst-Pack and Gilat k-point net. Values of 12, 12, 12, 40, and 60 were applied as truncation criteria for the bielectronic integrals. An energy convergence criterion of $10^{-7}$ a.u. was used in the self-consistent field iterations. Localizations of periodic wave functions were performed for valence electrons only, following the scheme in Ref. [230]. Default Boys control parameters were applied with initial and final tolerances for the density matrix element calculation and a convergence criterion of $10^{-7}$. Density fitting was performed purely in the direct space using the aVTZ-PP_MP2F basis sets for Te and Pb, developed by Hättig et al. [238]. Domain sizes were defined manually to ensure consistency in the LMP2 computations. Domain sizes were set to 1, including only the atom itself, since LMP2 calculations had to be performed without symmetry for numerical reasons. Without symmetry, however, larger domains become too large to handle.

In the incremental cluster calculation I adopted the embedding scheme developed by Herschend et al. [239] and Müller and Hermansson [240]. This scheme is illustrated in Fig. 3.1 and replaces atoms around a quantum mechanically treated cluster as formal point charges. In the case of $MgF_2$ these point charges were $+2$ and $-1$ for $Mg^{2+}$ and $F^-$, respectively. At a certain distance this field of formal point charges is truncated and point charges along a sphere mimic the long range interactions of point charges. Close to the quantum mechanically treated cluster borders, positive charges are replaced by effective core potentials.

## 3.2 Surface Models

In Paper A3 we introduce a model to calculate the surface energy of symmetric but off-stoichiometric slabs that is based on the extrapolation scheme proposed by Gay et al. [241]. Since we are the first to apply this approach to off-stoichiometric surface slabs, I strongly believe a more detailed description and discussion of the method is necessary.

Typically, surface energies are calculated as shown in Eq. 2.85. However, this notation has certain drawbacks, of which one is that the slab and bulk units have to be described on a consistent numerical level. This comprises, for example, a consistent numerical treatment of bielectronic integral sums in each case (e.g. thresholds) or the correctly considered in-

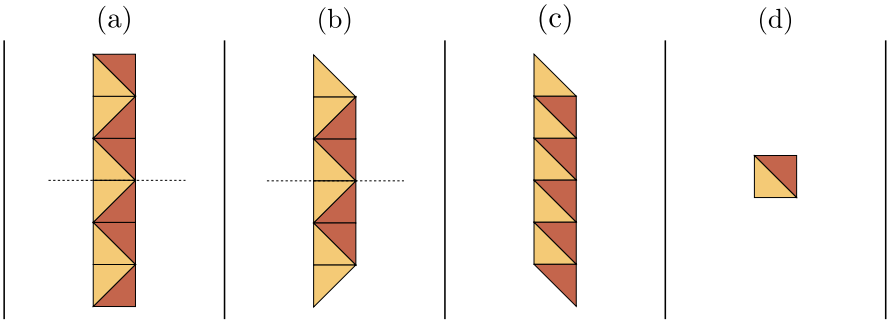


Figure 3.2: Illustration of different slab types and their corresponding bulk unit. From left to right: (a) symmetric, stoichiometric slab; (b) symmetric, off-stoichiometric slab; (c) asymmetric, stoichiometric slab; (d) corresponding bulk unit. The dashed line indicates a mirror plane.

fluence of the BSSE. Otherwise the subtraction leads to significant errors, since the surface energy is generally a very small number that results from the difference of two large numbers. Systematic errors are canceled by a different definition of the surface energy as

$$E_{\text{surface}} = \frac{1}{2\Lambda} E(N) - N\left[E(N) - E(N-1)\right], \tag{3.1}$$

where $E(N)$ is the energy of an $N$-layer slab. In Eq. 3.1 the bulk energy $E_{\text{bulk}}$ is exchanged for the expression $E(N) - E(N-1)$, which should converge to the energy of a single layer in the bulk for large enough slabs. This notation has the advantage that every term is calculated under the same numerical conditions (as mentioned above, e.g. treatment of bielectronic integrals or BSSE).

The extrapolation scheme of Gay et al. [241] is based exactly on Eq. 3.1. They proposed to rewrite Eq. 2.85 as

$$E_{\text{slab}}(N) = 2\Lambda E_{\text{surface}} + N E_{\text{bulk}}^{N}, \tag{3.2}$$

where $E_{\text{bulk}}^{N}$ corresponds to the term $E(N) - E(N-1)$ from Eq. 3.1 and is an abstract bulk energy per slab layer. For large enough slabs, $E_{\text{slab}}$ can be plotted as a function of $N$ and the surface energy can be extracted directly as the $y$-intercept from a linear fit.

Besides the numerical errors, which I will assume to be negligible for now, all three Eqs. 2.85, 3.1, and 3.2 have the drawback of not being universally applicable. 2.85 is only well defined for integer values of $n$, the number of bulk units in the slab, while Eqs. 3.1 and 3.2 require well defined layers. Fig. 3.2 illustrates schematically different types of slabs, where Eq. 2.85 can only be applied to the stoichiometric ones. However, stoichiometric slabs are not always symmetric (see Fig. 3.2c). This again leads to a mixture of surface terminations and, hence, a mixture of surface energies of these two terminations. Then again, the existence of symmetric and stoichiometric slabs for complex crystalline systems – where a complex system might already be one with a two-atom basis – is hardly the rule and rather the exception. Additionally, the definition of layers is often ambiguous if possible at all (see Fig. 3.2). Usually, these two points prevent the straightforward surface energy calculation for such systems.

For each surface plane of $CoSb_3$ there exist in principle stoichiometric slabs. However, they are asymmetric. Then again there exist symmetric slabs, which are off-stoichiometric. To nonetheless calculate the surface energies, in Paper A3 we proceed in the following way. First we define layers in reference to the $z$-coordinate. Thus, all atoms with the same $z$-coordinate in the slab belong to the same layer. Next, we calculate the slab energy for different slab sizes. The slabs were enlarged by adding complete bulk units (in Fig. 3.2b this corresponds to a whole square). Thus, the difference between two slabs of different sizes is always a stoichiometric unit of the bulk. Afterwards, the slab energies are plotted and fitted to obtain the surface energies.

For these calculations the definition of the layers is crucial, because they determine where the linear fit hits the $y$-axis and therefore the absolute value of the surface energy. Additionally, the layer partitioning of slabs that belong to different planes might be significantly different and consequently the comparability might suffer. In the case of $CoSb_3$ we confirm consistency by comparing the fitted results with surface energies obtained from the asymmetric but stoichiometric slabs and Eq. 2.85. Since for the latter the surface energy is constituted by two different terminations we compare the sum of these two surface energies. In the case of $CoSb_3$ these energies add up nicely and differ by $\pm 5$ % at most.

# Chapter 4

# Applications

The investigations in this thesis were performed in close cooperation with our experimental partners. Thus, a strong motivational source of this work is the interpretation and explanation of experimental results but also the prediction of not yet experimentally observed properties. At the same time this work presents and assesses widely adopted quantum chemical methods and provides alternative schemes for calculating key properties, like surface energies. The main results and outcomes are summarized in five papers A1-A5 that are added to this thesis. The idea of this section is to summarize important outcomes and to provide additional results that are not yet included in publications.

Starting with its still debated electronic properties, in **Paper A1** I have revisited the ground state properties of $CoSb_3$ skutterudites with various methods. In this first paper, special attention was given to the methodical part and the peculiar electronic structure. I found that structure parameters of all applied DFT functionals agree reasonably well with experiment, while the bulk modulus is only sufficiently described by GGA functionals. The cohesive energy is strongly underestimated by HF which emphasizes the importance of electron correlation for these materials, which has not been investigated so far. Additionally, the results in Paper A1 show that most of the confusion of earlier studies concerning the size of the band gap is due to its dependence on the lattice parameter and due to different DFT exchange-correlation functionals. The electronic structure was found to be strongly influenced by the lattice structure of the $Sb_4$ rings. Upon deformation of the $Sb_4$ rings the dispersion of the highest occupied (HO) band increases or decreases significantly. Further explanations and more details are given in Sec. 4.1. The calculations and the preparation of the manuscript for Paper A1 were done by myself. The co-authors contributed with supervision and discussions of results to this project.

In **Paper A2**, a joint theoretical and experimental investigation, I studied the electronic transport properties of the meta-stable $FeSb_3$ and its similarities to $CoSb_3$. Measurements by the co-authors Daniel et al. of the electrical conductivity of $FeSb_3$ films revealed metallic-like behavior and a large hole density, however, at the same time a large Seebeck coefficient. This unusual but fortunate combination for a thermoelectric material results in a promising power factor. The computations of the electronic band structure and of the corresponding transport coefficient verified that the measured properties are due to the specific shape of the $FeSb_3$ band structure. Due to the electron deficiency compared to cobalt, the $FeSb_3$ is a p-type semiconductor. In fact the band structure bears striking resemblance to the typical p-type doped skutterudite $CoSb_3$ band structure. This description explains very nicely the measured electronic transport properties. All theory contributions to Paper A2 were done by

myself, including the preparation of the theory parts of the manuscript.

From the parent materials, there are two ways to further proceed the investigation on skutterudites, which are filling and nanostructuring. Both, in principle, aim at reducing the thermal conductivity but have an influence on the electronic properties as well. While filling is discussed in Sec. 4.2, a first step towards nanostructuring is taken in **Paper A3**. This work was performed together with Marcel Quennet (co-supervised master thesis) and Kai Töpfer (co-supervised research internship) and considers surface energies for all low-index surfaces of $CoSb_3$. For Paper A3, structure relaxations were performed by Marcel Quennet. The calculations of bulk band structures were performed by Kai Töpfer. My contributions to Paper A3 include the supervision of the work, the preparation of the manuscript and the calculation of the electronic structure of the slabs. Although cubic, $CoSb_3$ surfaces are challenging to describe. Besides a large quantity of possible cuts through the low-index surfaces, i.e. terminations, stoichiometric surface slabs are hardly ever symmetric. Therefore, in Paper A3 we propose an extrapolation scheme that allows us to calculate the surface energies in spite of slabs being off-stoichiometric. We find one very stable (110) termination that is strongly favored over other surfaces and their terminations. The energetic order is (110), (100) and (111), respectively. Besides the surface energetics we have investigated the electronic structure of surfaces and reveal surface states that lead to a metallic behavior at the surface. The metallic behavior is well reflected by measurements on $CoSb_3$ thin films. These measurements were performed by our cooperation partners, the group of Prof. Dr. E. Müller, and showed an increased electrical conductivity and indications of a shift towards metallic behavior [242].

Methodical improvements on our quantum chemical description can be obtained in principle by applying wave function based electron correlation methods. As mentioned in the beginning of this work, electron correlation contributes quite strongly to the cohesive energy of $CoSb_3$. This is indeed the case for PbTe too, which is shown in Sec. 4.3. However, the application of wave function based electron correlation to complex, and, more importantly, small gap semiconductors, is a challenging task in itself. In **Paper A5** we show how to apply periodic LMP2 to group-12 fluorides. The electron correlation contribution in that case increases with increasing atom sizes. For an increasing electron correlation contribution MP2 is insufficient to describe it accurately enough. Improvements can be obtained in the method of increments that allows in principle the application of any size-consistent correlation method. For Paper A5 I prepared the manuscript and performed the ab-initio calculations. **Paper A4** shows how to apply the method of increments to surface energies and compares it for MP2 with the periodic LMP2 method. In principle, this method can be applied to thermoelectric materials and their surfaces as well. In general terms, the results on the test case of $MgF_2$ show that short range electron correlation stabilizes the surface, while, due to missing coordination partners, long range electron correlation destabilizes the surface. The scheme proposed in Paper A4 was developed in close cooperation with Lorenzo Maschio. All the ab-initio calculations were performed by myself as was the preparation of the manuscript.

## 4.1 Skutterudites as Thermoelectrics

Although there exists a huge variety of possible compositions – including filling and doping – for the different types of skutterudites, as a start I focused my investigation on iron and cobalt antimony skutterudites. With the desire for better and better performing thermoelectric materials the general attention of the thermoelectric community has shifted towards filled and doped skutterudites. However, already for the parent material $CoSb_3$ many issues are still unresolved. As mentioned in the introduction and as an example, investigations on $CoSb_3$ so far yielded ambiguous results concerning the peculiar electronic structure. Up to now, it is still under debate, whether or not this ambiguity is due to methodical reasons or due to "impurities" in the material.

Independent of the method, theoretical investigations so far revealed that the strongly dispersive HO band in $CoSb_3$ makes it a narrow band gap semiconductor and as such makes it difficult to characterize, both by experiment and theory. While the purity and homogeneity of samples are major experimental challenges, theoretical computations were found to depend strongly on the applied method. In fact in Paper A1 I reinvestigated the $CoSb_3$ ground state properties with various methods, including standard DFT functionals and the HF method, with plane-wave and atomic basis set codes. I found that not only previous results are nicely reproduced by the respective methods, but also that the energy gap depends strongly on the applied exchange-correlation functional. Band gaps obtained with GGA functionals (PBE, PW91), for example, are about 50 % smaller than obtained with the LDA functional. Hybrid functionals yield by far the largest band gap, which is related to the overestimation by HF and the mixing of HF exchange into the hybrid functional energies. This deviation of the functionals makes an educated assessment of the methods very challenging. However, results are independent of the applied basis set type, plane wave or atomic basis sets. Improved optical band gaps might be obtained from electron correlation methods like the configuration interaction singles method (see e.g. Ref. [243] and references therein). However, this method is still under development.

Contributing to the aforementioned ambiguous results is another important point. The electronic structure depends also strongly on the lattice parameter. The energy gap is almost inverse proportional to the size of the lattice parameter. This point remains true independent of the applied method and the transition metal. In Fig. 4.1 the band gap size

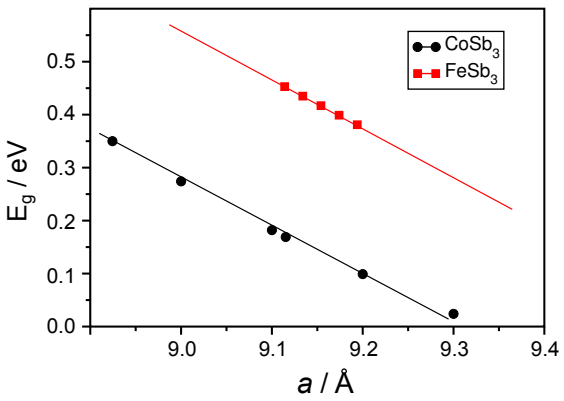


Figure 4.1: Energy gaps with respect to the lattice parameter $a$ for $CoSb_3$ and $FeSb_3$.

is plotted as a function of the lattice parameter for both parent materials $CoSb_3$ and $FeSb_3$. Many previous investigations employed different lattice structures and, thus, obtained different band gaps, which explains many deviations published earlier. The same method, at the experimental or the optimized lattice structure, results in significantly different energy gaps.

In addition, the electronic structure is not only strongly influenced by the lattice parameter, but also by the two free inner parameters, $y$ and $z$ of the skutterudite lattice. Altering these two parameters leads to a conformational change in the $Sb_4$ rings and a change in the dispersion of the HO band at $\Gamma$ (see Paper A1 and Figs. 4.2 and 4.3). Increasing $y$ decreases one edge (referred to as $q$, see Fig. 4.2 top) of the $Sb_4$ ring, which is directed towards the voids. Increasing $z$ increases the edge of the $Sb_4$ rings in the direction parallel to the voids (referred to as $p$, see Fig. 4.3 top). Experimentally, however, randomly manipulating $y$ and $z$ is challenging, especially independent from each other. Filling or doping, however, can influence the $Sb_4$ ring structure quite strongly. Thus, changing $y$ and $z$ in the parent material is not only of academical interest but reflects actual experimental structures from a fundamental point of view. The influence of the $Sb_4$ rings is illustrated in Figs. 4.2-4.5 by analyzing the electronic structure and transport properties.

The ground state properties of $CoSb_3$ and $FeSb_3$ have been investigated and shown in detail in Papers A1 and A2. By comparison with experiment, we found that for a given experimental carrier concentration, transport properties obtained by PBE agree nicely with experiment. Apart from that, qualitatively LDA and other GGA exchange-correlation functionals yield very similar results for the transport properties, differing in absolute values only by a few percent. Based on this I applied the PBE functional in further DFT computations.

Figs. 4.2-4.5b show the electronic structure and the electronic transport properties at the optimized equilibrium structure, while Figs. 4.2-4.5a and Figs. 4.2-4.5c for increased or decreased $q$- or $p$-$Sb_4$ ring edges, respectively. The figures show that, independent of the transition metal, an $Sb_4$ shift towards or away from the voids increases or decreases the dispersion of the HO band at the $\Gamma$-point significantly. However, shifts parallel to the voids leave it almost unaffected. Instead, in the latter, the dispersion at the P-point is increased or decreased. The same results are achieved for the $FeSb_3$. Here, however, due to the electron deficiency compared to $CoSb_3$, the Fermi level is shifted into the valence bands, which leads to a p-doped semiconductor.

Besides the apparent effect on the electronic band structure, the transport properties, with respect to the chemical potential, are much less affected. In the following the transport coefficients are always discussed with respect to the chemical potential. The electrical conductivity changes only slightly, compared to the equilibrium structure, for the simple reason that the HO band contributes only very little to the electrical conductivity. The Seebeck coefficient is already effected more strongly. However, more interesting for the quality of the electronic transport properties is the interplay of these two quantities, given by the power factor. Assuming for each case an equal relaxation time $\tau$, the power factor increases quite strongly for larger $q$ values (see Fig. 4.2a). This is due to an enhancement in the Seebeck coefficient. As a reminder, according to Eq. 2.78, the total Seebeck coefficient is the sum of the single band Seebeck coefficients weighted by the single band electrical conductivity and divided by the total electrical conductivity, $S = \left(\sum_i \sigma_i S_i\right)/\sigma$. Hence, the Seebeck coefficient is largest for a chemical potential where the weighted Seebeck coefficient of a single band is

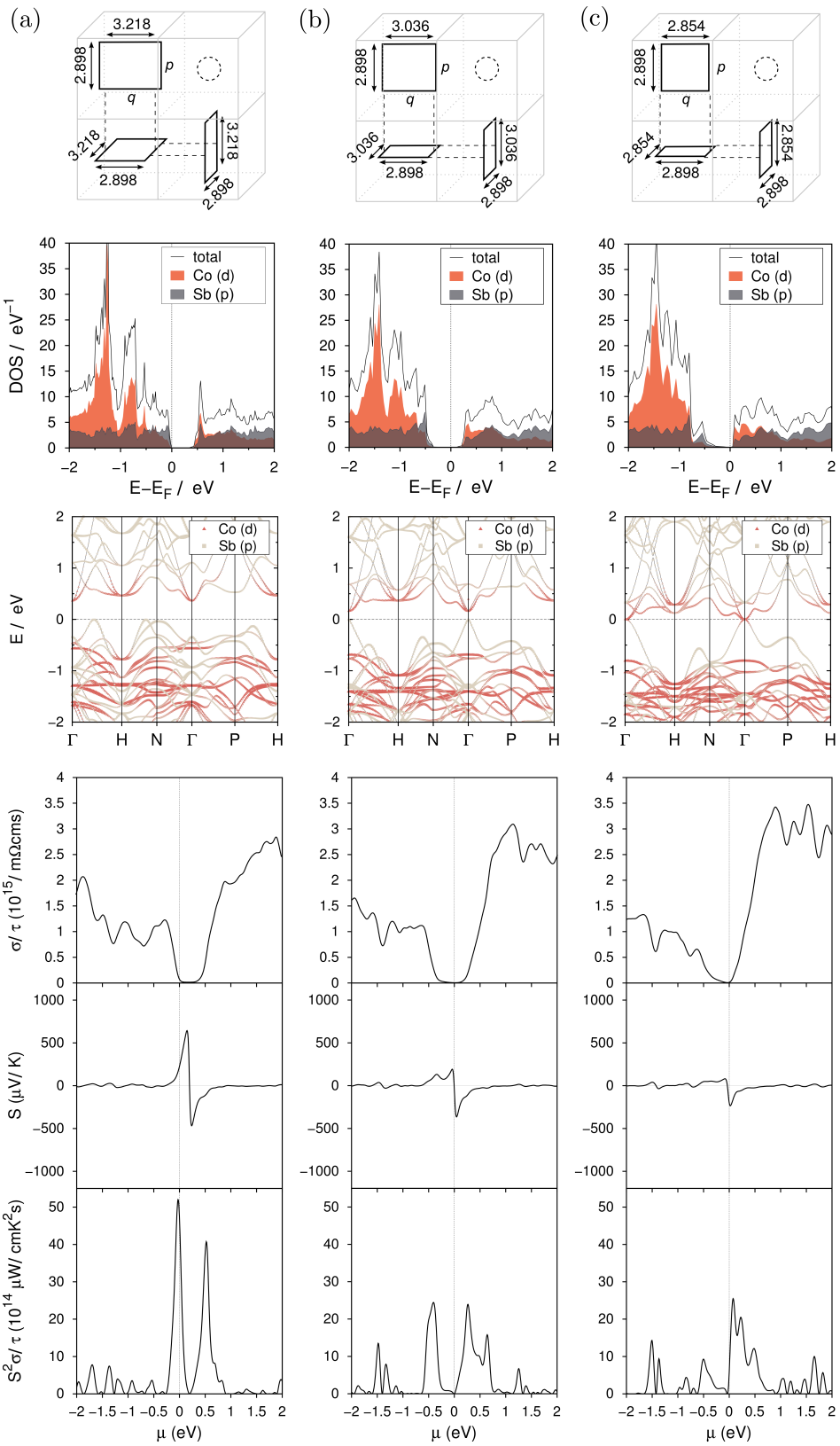


Figure 4.2: Variation of the free $y$-coordinate of Sb in $CoSb_3$. From top to bottom: schematic illustration of the $Sb_4$ ring change, Co(d) and Sb(p) projected density of states and band structure, transport properties at 300 K. The free coordinates are $z = 0.159$ and (a) $y = 0.3234$, (b) $y = 0.3334$, (c) $y = 0.3434$. The void is illustrated by the dashed circle.

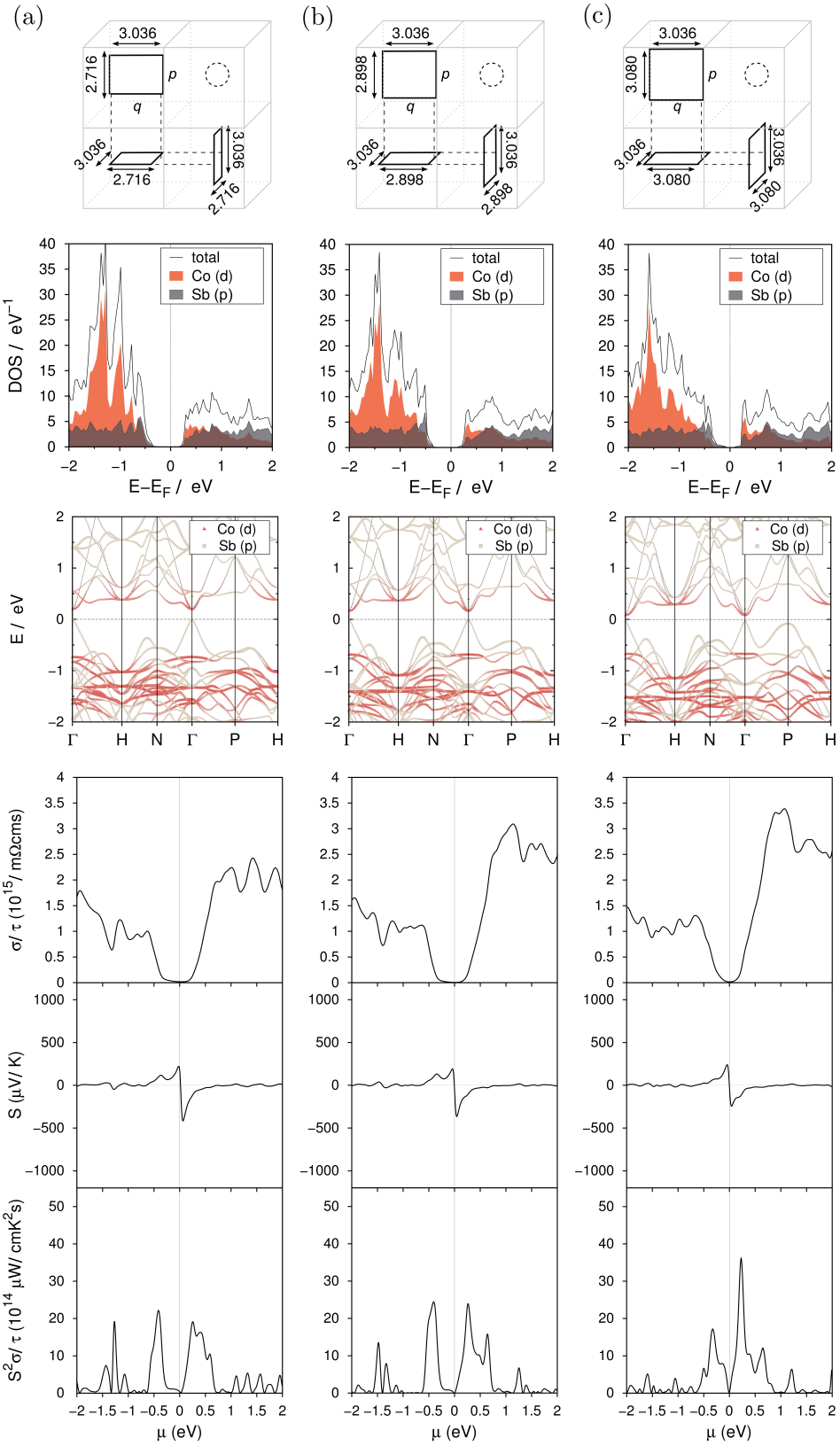


Figure 4.3: Variation of the free $z$-coordinate of Sb in $CoSb_3$. From top to bottom: schematic illustration of the $Sb_4$ ring change, Co(d) and Sb(p) projected density of states and band structure, transport properties at 300 K. The free coordinates are $y = 0.3334$ and (a) $z = 0.149$, (b) $z = 0.159$, (c) $z = 0.169$. The void is illustrated by the dashed circle.

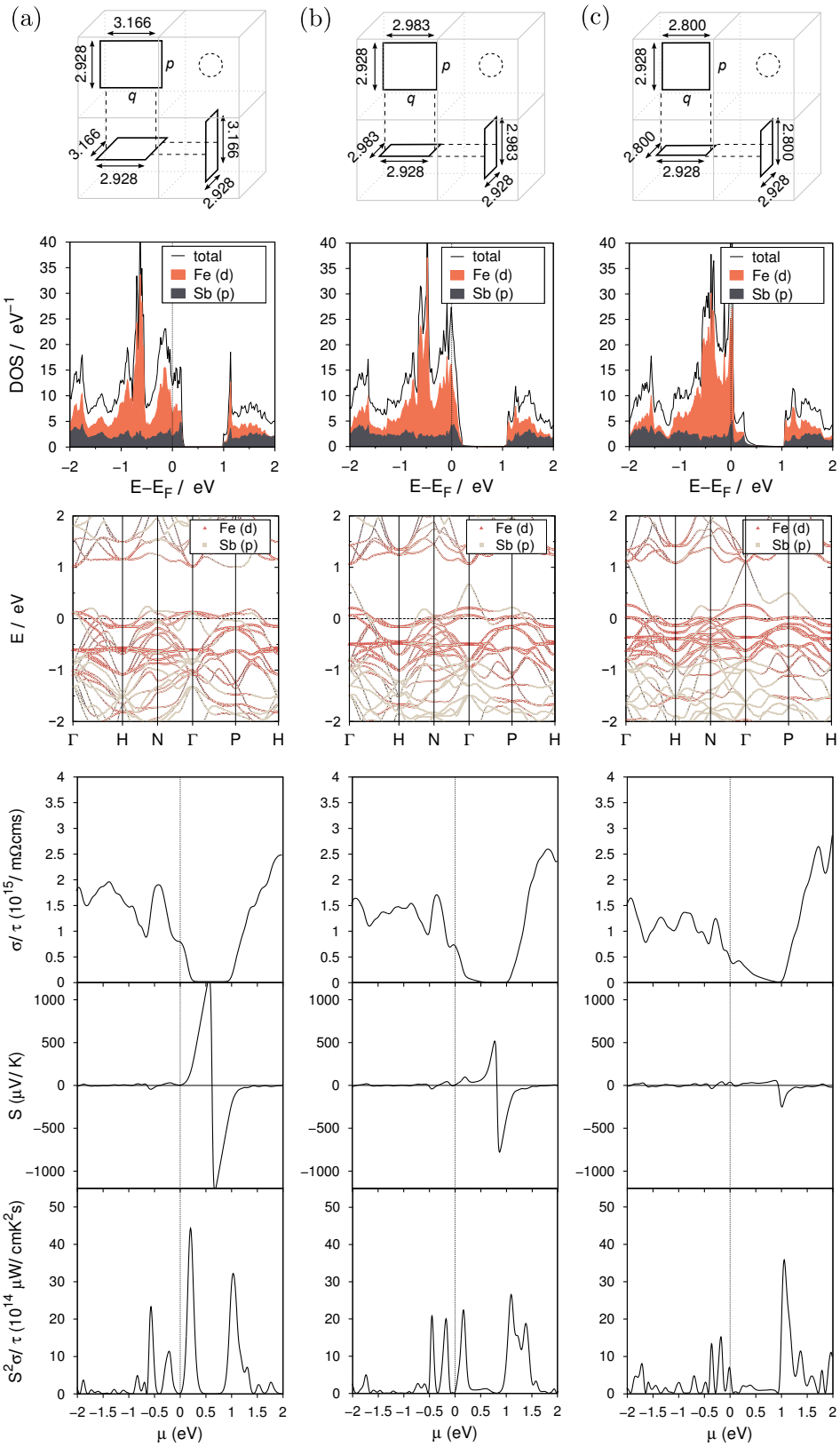


Figure 4.4: Variation of the free $y$-coordinate of Sb in $FeSb_3$. From top to bottom: schematic illustration of the $Sb_4$ ring change, Fe(d) and Sb(p) projected density of states and band structure, transport properties at 300 K. The free coordinates are $y = 0.3334$ and (a) $z = 0.149$, (b) $z = 0.159$, (c) $z = 0.169$. The void is illustrated by the dashed circle.

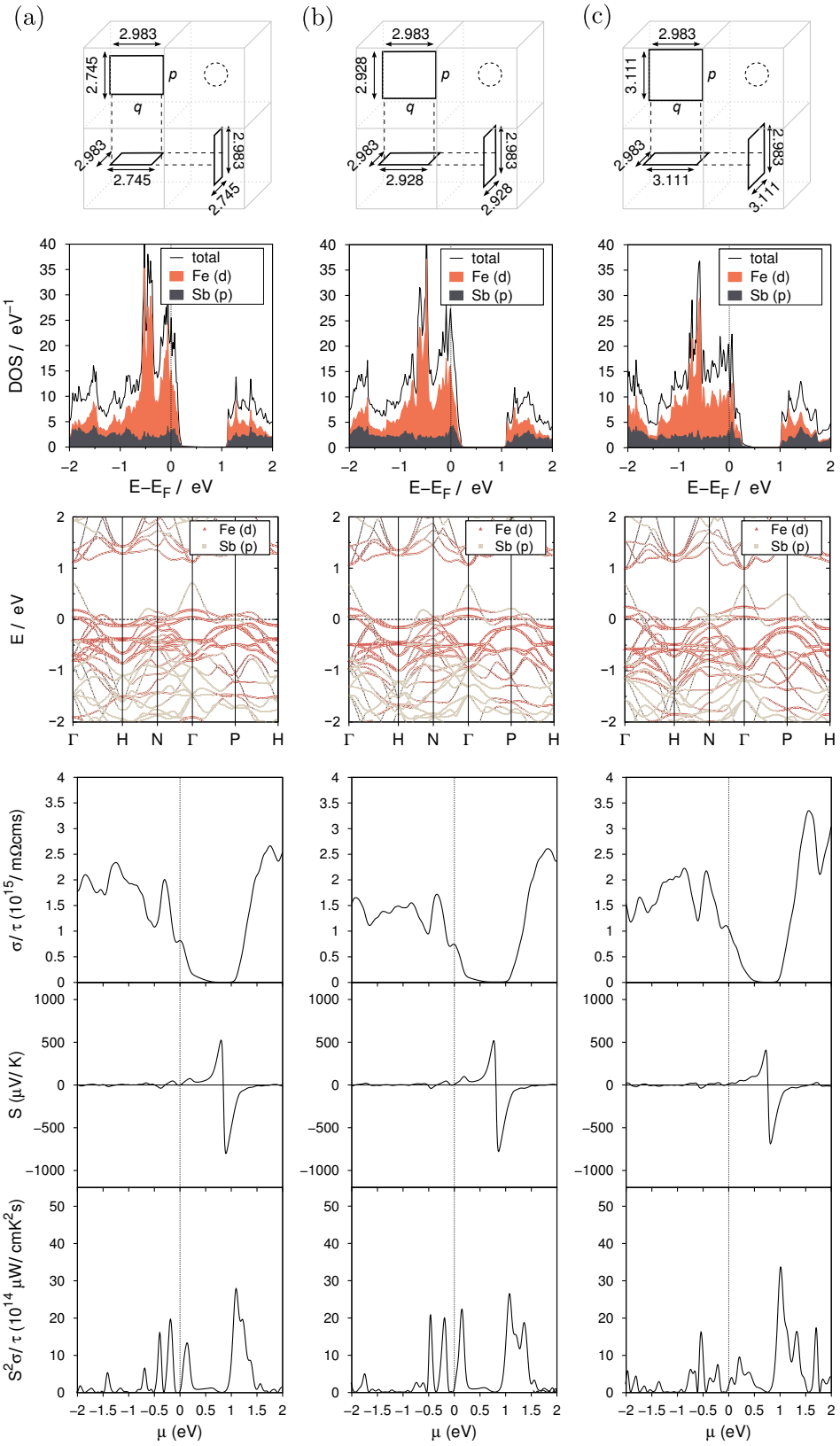


Figure 4.5: Variation of the free $z$-coordinate of Sb in $FeSb_3$. From top to bottom: schematic illustration of the $Sb_4$ ring change, Fe(d) and Sb(p) projected density of states and band structure, transport properties at 300 K. The free coordinates are $y = 0.3334$ and (a) $z = 0.149$, (b) $z = 0.159$, (c) $z = 0.169$. The void is illustrated by the dashed circle.

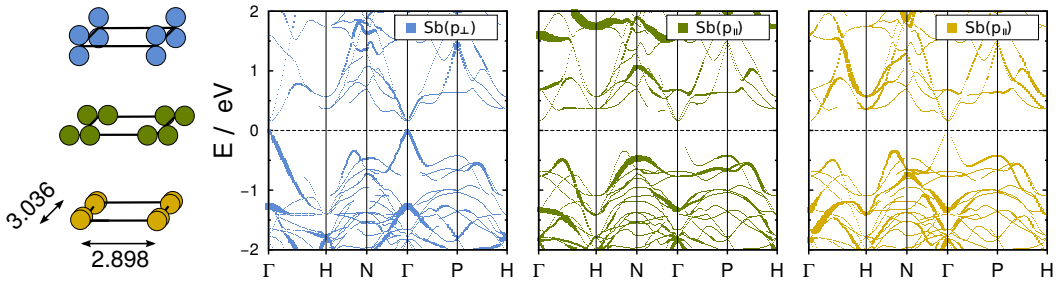


Figure 4.6: Sb p-orbital projected $CoSb_3$ band structure for p-orbitals perpendicular (blue) and parallel (green, yellow) to the $Sb_4$ ring plane.

large and where the total conductivity is small. This is the case at band edges close to a gap.

In Fig. 4.2a the former HO band shrinks into the valence bands and two other prominent bands become the new HO bands. They are both close to the gap and, therefore, contribute to an enhanced Seebeck coefficient compared to the smaller one from the equilibrium structure. However, the contribution of these bands can also be seen in the equilibrium structure in Fig. 4.2b. In this case the Seebeck coefficient shows two small maxima, one very close to $\mu = 0$ eV, the other close to $\mu = -0.4$ eV. Although for both peaks the Seebeck coefficient is of the order of 250 $\mu$V/K, the electrical conductivity is much smaller for the equilibrium structure, which results in a smaller power factor. In Fig. 4.2c the HO band reaches into the conduction bands, which leads to a metallic character. As a result the Seebeck coefficient weakens. In the case of an enlarged $p$-edge of the $Sb_4$ rings (parallel to the voids) the electronic transport properties are much less effected. Very similar conclusions as above can be drawn in the case of $FeSb_3$.

The aforementioned points emphatically show how the $Sb_4$ ring structure affects the shape of the HO band. Indeed, this finding leads directly to another still debated point of the electronic structure of skutterudites, which is the composition of the HO band. p-projected band structures show a strong Sb(p) character for the HO band (see e.g. Paper A1 or Figs. 4.2-4.5). Further partitioning of the projection into $p_x$, $p_y$ and $p_z$ (see Fig. 4.6) reveals that mostly only p orbitals perpendicular to the $Sb_4$ ring plane ($p_\perp$) contribute to the prominent HO band. Jung et al. [244] investigated the electronic structure of La filled $FeP_3$ and proposed that $Sb_4^{4-}$

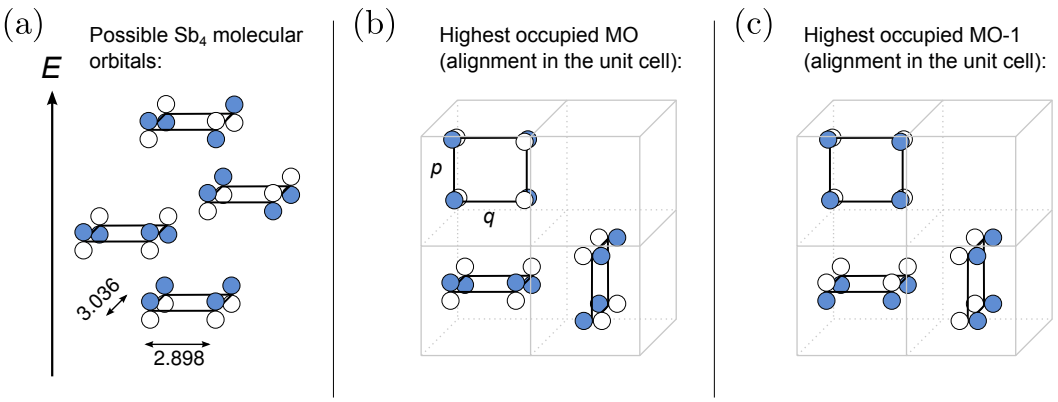


Figure 4.7: a) Schematic illustration of possible $Sb_4$ molecular orbitals in energetic order. b) The HO and c) the HO-1 molecular orbitals in half of the unit cell.

units form molecular orbitals similar to cyclobutadien as illustrated in Fig. 4.7a. Thus, for a $Sb_4^{4-}$ unit all four molecular orbitals are occupied and the HO band is then constituted by the highest molecular orbital. However, in my studies for the parent material $CoSb_3$, Bader charge analyses reveal no negative charge at the Sb atoms and instead indicate a slightly positive charge.

Besides the charge, the theory by Jung et al. does not explain why the energy level of the HO band changes drastically when the $Sb_4$ rings are elongated towards the voids and almost not when the $Sb_4$ rings are elongated along the voids. If we keep, however, the simple molecular orbital picture and assume an uncharged $Sb_4$ unit, the highest occupied molecular orbital is the second in energetic order in Fig. 4.7a. This configuration in the unit cell is shown in Fig. 4.7b. In this case, increasing or decreasing $q$ leads to a more favorable or less favorable orbital energy, while increasing or decreasing $p$ has not a large effect. The dispersion at Γ is then caused by the inter-ring overlap, which stays approximately the same, as is indeed the case for the HO band in any of the elongated ring structures. In the region of −1 to −2 eV at the Γ-point (see Fig. 4.6) is another prominent band almost exclusively formed by the $p_\perp$ orbitals. In the above picture this corresponds to the lowest of the four $Sb_4$ molecular orbitals, as illustrated in Fig. 4.7c.

Despite its appealing nature, the aforementioned model is rather simple. On the one hand $Sb_4$ rings are considered to form independent molecular orbitals, on the other hand, hybridizations of Sb(p) and Co orbitals are neglected. Pardo et al. [116] examined the transi-

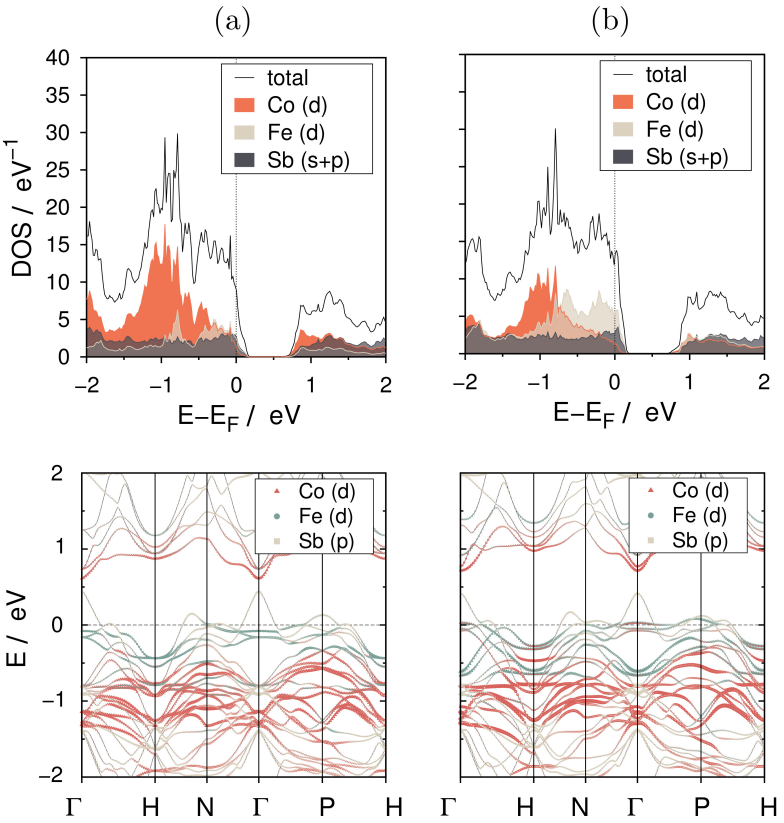


Figure 4.8: Projected DOS and projected band structure of the Fe substituted $CoSb_3$ skutterudite obtained by DFT/PBE: (a) $FeCo_3Sb_{12}$ and (b) $Fe_2Co_2Sb_{12}$.

Table 4.1: Optimized lattice parameter for the gradually Fe substituted $CoSb_3$ skutterudite, as obtained with DFT and the PBE exchange-correlation functional and spin-polarization.

| Structure | $a_0$ | $B_0$ / GPa | $B_0'$ |
|---|---|---|---|
| $Co_4Sb_{12}$ | 9.115 | 82.5 | 3.94 |
| $FeCo_3Sb_{12}$ | 9.129 | 81.9 | 4.73 |
| $Fe_2Co_2Sb_{12}$ | 9.144 | 81.1 | 4.81 |
| $Fe_3CoSb_{12}$ | 9.161 | 80.3 | 4.81 |
| $Fe_4Sb_{12}$ | 9.167 | 79.7 | 5.22 |

tion of $CoSb_3$ from the perovskite to the skutterudite structure and found that the gap only opens when the $p_{\parallel}$ bonding-antibonding splitting becomes strong. This is due to a mixing of Co(3d) with Sb(5p) orbitals. However, considering the local $D_{3d}$ symmetry in the $CoSb_6$ unit, mixing is symmetry allowed only if Sb atoms form molecular orbitals that again can be classified in terms of even or odd parity. Pardo et al. claimed that 12 such molecular orbitals are formed by the 12 $\pi$-oriented Sb($p_{\perp}$) orbitals in the primitive unit cell and are centered at the void. How these 12 molecular orbitals look like exactly is quite challenging to determine. However, it is sensible to assume that the strongest interaction, i.e. the biggest overlap, is between p-orbitals within an $Sb_4$ ring and only then followed by the $Sb_4$-$Sb_4$ interaction. Hence, the strong dispersion of the HO band is more likely due to p-orbital interactions than inter $Sb_4$-ring interactions. A molecular orbital, out of the possible 12, that corresponds to such a situation, and which still reproduces the peculiar behavior of the HO band, is very likely to have the same shape as shown before for independent $Sb_4$ rings (see Fig. 4.7b). Thus, one of the 12 molecular orbitals might correspond to the same configuration as in the simpler picture of independent $Sb_4$ rings.

From an experimental point of view, $FeSb_3$ skutterudites are often produced by substituting Co with Fe. The gradual substitution of Co with Fe has two effects on the electronic properties. Since Fe misses one electron compared to Co, the $FeSb_3$ is a p-type semiconductor. Gradual substitution leads therefore to a gradual p-doping of $CoSb_3$, although the total density of states keeps its $CoSb_3$-typical shape. Fig. 4.8 shows the electronic structure for the $FeCo_3Sb_{12}$ and $Fe_2Co_2Sb_{12}$ cases. Additionally, Fe atoms mainly contribute to the valence bands adding to a larger density of states close to the Fermi level. These additional states contribute to an improved Seebeck coefficient.

Besides the changes in the electronic structure, substitution of Co with Fe increases the lattice constants and leads to a slightly reduced bulk modulus (cf. Tab. 4.1). The $Sb_4$ rings gradually change towards their conformation as found in the completely filled $FeSb_3$ structure. Thus, the substitution leads to a slightly stretched $Sb_4$ ring towards the voids. Consequently, the HO band slightly decreases and the band gap widens.

## 4.2 Filled $CoSb_3$ Skutterudites

In principle, with their vacant 2$a$ sites, skutterudites are ideal cage compounds that allow to be filled. Indeed, as mentioned in the introduction, many studies report filling with various atoms and filling species. Even filling with two filler atoms is possible. However, filling of the voids is not always thermodynamically favored over substitution of antimony atoms. Thus, whether or not filler atoms really enter the voids, or rather substitute, is still under debate for many filling species. A prominent example of such a species is the gallium atom. Hence, besides its evident success in tuning skutterudites as thermoelectrics, filling still poses a challenging task for experiment and theory to describe.

By analyzing the lattice structure upon gradually filling of the 2$a$ vacant sites and comparing to experimental results, I show a simple relation between the structure of filled skutterudites and the occupation of either Sb or void sites. For that, I consider three filler species (Y = In, Ga, Tl) in 2x2x2 supercells that allow for nine filling fractions $X$, starting from 0 to 1. In this model, lattice parameters refer to structures where filler atoms solely occupy the 2$a$ vacant sites. Additionally, only the most favorable configuration for each filling fraction was considered, although there exists a huge variety of possible filling configurations. The lattice parameters obtained in this way increase almost linearly with increasing filling fraction (cf. Tab. 4.2), independent of the applied filling species.

Experimentally, there is a material dependent maximum of up to which a skutterudite can be filled [102] and thus experimental data is normally available in the range of $x < 0.3$ only. Unfortunately, very small filling indices require unfeasibly large supercells in the computations. However, if I compare experimental data with my calculated data and assume a linearly expanding lattice parameter with respect to an increasing filling fraction, I might easily extra- or interpolate to smaller or larger fractions, respectively. Such an extrapolation is shown in Fig. 4.9.

Up to now, there are quite a few experimental investigations on the lattice parameter with

Table 4.2: Lattice parameters ($a_0$ in Å) of $Y_XCo_4Sb_{12}$ for three different filler species (Y = Ga, In, Tl) and nine different filling fractions (X = 0, 0.125, 0.25, 0.375, 0.5, 0.625, 0.75, 0.875, 1).

| X | Y = Ga | In | Tl |
|---|---|---|---|
| | | $a_0$ / Å | |
| 0 | | 9.11491 | |
| 0.125 | 9.12619 | 9.12263 | 9.12767 |
| 0.25 | 9.13635 | 9.12876 | 9.13933 |
| 0.375 | 9.14559 | 9.13410 | 9.15045 |
| 0.5 | 9.15480 | 9.13905 | 9.16084 |
| 0.625 | 9.16401 | 9.14466 | 9.17260 |
| 0.75 | 9.17312 | 9.15016 | 9.18278 |
| 0.875 | 9.18189 | 9.15530 | 9.19319 |
| 1 | 9.19060 | 9.16028 | 9.20361 |

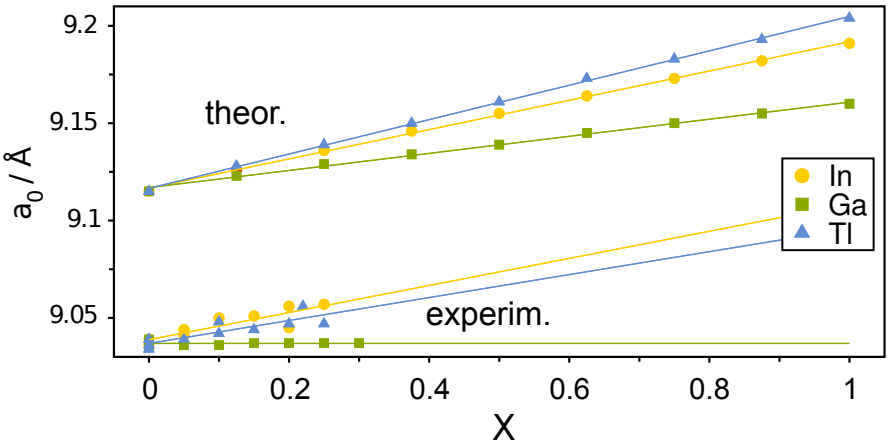


Figure 4.9: Computed (DFT/PBE) and measured lattice parameters $a_0$ as functions of the filling fraction X for $Y_XCo_4Sb_{12}$. Experimental values are taken from Refs. [31, 78, 245–248].

respect to the filling, which allows me to assess, if the above mentioned assumption is reasonable. Fig. 4.9 shows the lattice parameter plotted against the filling fraction for a large collection of measured values (taken from Refs. [31, 78, 245–248]) together with my calculated values. For both, the experimental and theoretical results, I assume a linear expansion of the lattice parameter and simply fit a linear curve via a least square fit to the data points. Thus, by simply comparing the slopes, one can estimate on whether or not Ga, In, or Tl occupy solely the voids.

For the In atom as a filler, theoretical values are in good agreement with experimental values overestimating the lattice parameter by about 1 %. Comparing the two slopes of $0.075 \pm 0.001$ Å and $0.070 \pm 0.015$ Å for the theoretical and the experimental data, respectively, shows that the relative prediction of the lattice parameter is in very good agreement with experiment.

A very similar trend can be observed for the Tl filled skutterudite. Theoretical lattice parameters are again overestimated by about 1 %, however, the calculated relative increase, i.e. the slope, ($0.088 \pm 0.001$ Å) is captured in reasonable good agreement compared to experiment ($0.066 \pm 0.015$ Å). That is true even though experimental values show a large distribution and consequently the fit features a rather large standard deviation.

For Ga the situation changes significantly. Experiments show a much lower increase of the lattice parameter with increasing filling ($0.0046 \pm 0.0015$ Å), compared to the theoretical model ($0.0439 \pm 0.0010$ Å). This already is an indication that Ga might not occupy solely the $2a$ vacant sites but additionally or exclusively substitutes Sb at the $24g$ Wyckoff positions. Additional support to my argument arises from recent work by Shi et al. [249], who found further indications that Ga indeed occupies both, the voids and the Sb sites of $CoSb_3$. Our cooperation partners in the AG Schlecht were able to reproduce the experimental findings of Shi et al. However, they went a step further and beyond a 50 % filling. After this percental threshold the lattice parameter increases again linearly with the filling fraction [250]. Given my theoretical predictions, these results indicate that Ga first substitutes the Sb atom position, until a certain substitution limit is reached. After that, Ga atoms begin to occupy the filling positions.

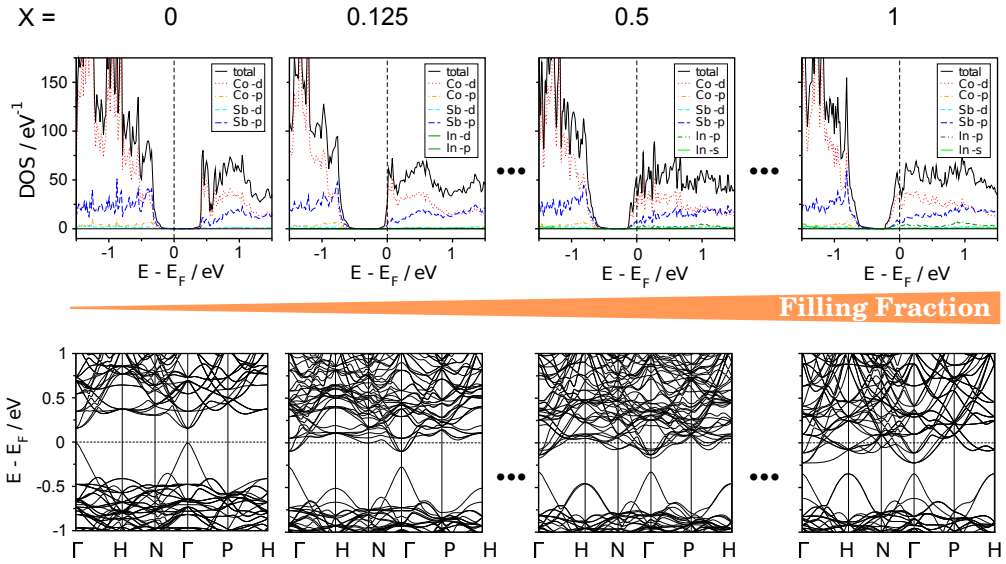


Figure 4.10: Electronic structure of $In_XCo_4Sb_{12}$ with respect to an increasing filling fraction X as obtained by applying DFT and the PBE exchange-correlation functional. Computations were performed in a 2x2x2 supercell and for the most stable configuration at each filling fraction.

Although much less than the lattice parameter, the bulk modulus is also affected by filling of the voids. For a filling fraction of 1 the bulk moduli for Ga, In and Tl filled $CoSb_3$ are summarized in Tab. 4.3. The gradual filling has a surprisingly small effect on the bulk moduli and changes them by about 1 % at maximum, keeping the linearity. Compared to the unfilled $CoSb_3$ skutterudite the bulk modulus decreases. However, along the group-13 elements (Ga, In, Tl) as fillers, the bulk modulus increases again, while for indium the bulk modulus is the same as for the unfilled $CoSb_3$.

Besides the effect on the lattice structural properties, filling also has an influence on the electronic properties and on the performance of $CoSb_3$ as a thermoelectric material. Introducing a group-13 filling species leads to an electron excess and, hence, to n-doping. Doping, however, proceeds gradually upon gradual filling. This effect is shown exemplary for indium in a 2x2x2 supercell in Fig. 4.10. With an increasing filling fraction, the n-doping increases. The HO band at the Γ-point, however, remains quite unaffected, as does the density of states close to the Fermi level. Upon increased filling, another band rises at the H-point.

Table 4.3: Optimized lattice parameter $a_0$ of $YCo_4Sb_{12}$ (Y = Ga, In, Tl) together with the bulk modulus $B_0$ and its pressure derivative $B_0'$ as obtained by DFT and the PBE exchange-correlation functional. The bulk modulus for the unfilled $CoSb_3$ is 80.6 GPa.

| Filler / | $a_0$ | $B_0$ / GPa | $B_0'$ |
|---|---|---|---|
| Ga | 9.160 | 75.93 | 10.02 |
| In | 9.191 | 80.62 | 10.70 |
| Tl | 9.204 | 81.99 | 10.24 |

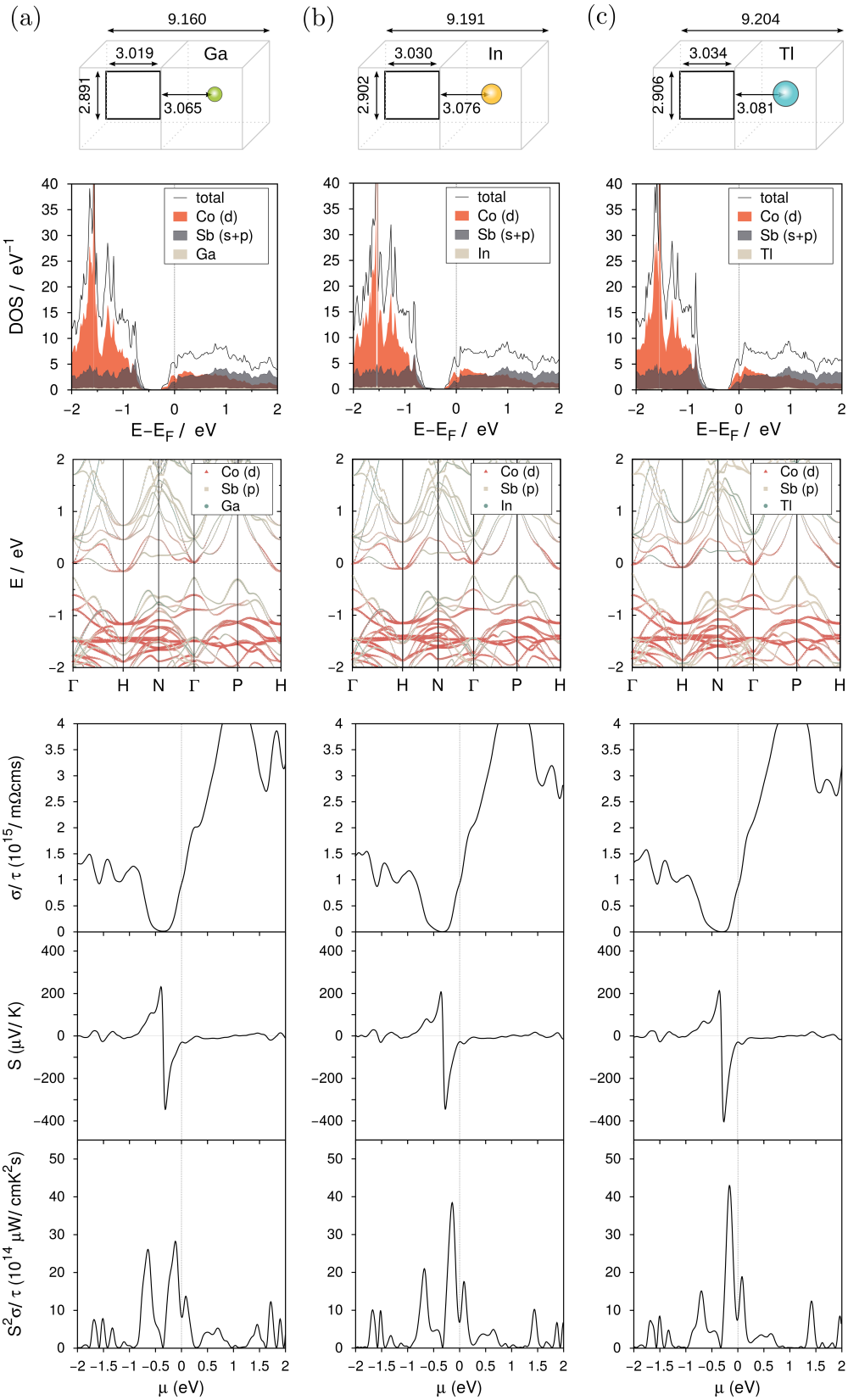


Figure 4.11: Ga, In and Tl filled $Co_4Sb_{12}$. From top to bottom: schematic illustration of the $Sb_4$ ring change and distance to the filler atom, Co(d), Sb(p) and filler projected density of states and band structure, transport properties at 300 K.

Since the change in the electronic structure proceeds quite linearly, further analyses of filling can be focused solely on the single unit cell. This provides the additional advantage that the symmetry of the unfilled $CoSb_3$ is kept, which in turn allows for a direct comparison between these two structures and their electronic properties. The obtained results are shown for all three filler species in Fig. 4.11. Filling of the voids leads to increased $Sb_4$ rings. However, due to the simultaneous increase of the lattice parameter, the void to $Sb_4$ ring distance increases too. This leaves the shape of the former prominent HO band almost unaffected, while its dispersion rises at the P-point. Projected band structure computations show a clear contribution of the In orbitals in the former HO bands. This indicates a mixing of indium p-orbitals and the 12 Sb molecular orbitals.

The electronic transport properties change only slightly with the filling, as can be seen in Fig. 4.11. The differences between the three filling species are even less significant. The electrical conductivity increases compared to the unfilled case, assuming an equal relaxation time. The Seebeck coefficient does not change significantly either. The largest changes can be seen for the power factor. In this case the peak at about $\mu = -0.2$ eV increases for the different filler atoms. While the power factor of the gallium filled $CoSb_3$ still bears a striking resemblance to the unfilled case, the power factor at $\mu = -0.2$ eV increases from indium to thallium. Additionally, the results reveal that a 100 % filling dopes the skutterudite too strongly, which agrees with the predictions for the unfilled case. A theoretically predicted optimal filling fraction $X$ at 300 K, assuming a linear dependency of the transport coefficients upon filling, would lie at 0.70, 0.66, 0.63 for gallium, indium and thallium, respectively. However, experiments reach a filling limit of 20 % at most.

The gradual transition from the unfilled to the fully filled $Y_XCo_4Sb_{12}$ with its minor influence on the transport properties and the very small experimentally achieved filling fractions, allow to estimate the transport properties with respect to the chemical potential from the unfilled structure. The calculated transport properties of the unfilled skutterudite show that the maximum of the Seebeck coefficient is already very close to the Fermi level. Consequently, already very small n-doping should lead to a large Seebeck coefficient. Then, upon further doping the Seebeck coefficient should decrease. Indeed, this is exactly the case in experimental observations for $In_XCo_4Sb_{12}$, where the Seebeck coefficient is $-226$, $-180$, and $-169\,\mu VK^{-1}$ for 5, 10, and 20 % filling [246].

Besides this nice qualitative agreement, for absolute values the situation is more complex. In the case of $In_{0.2}Co_4Sb_{12}$ (20 % filling), Hall measurements find a charge carrier concentration of $9.1{\cdot}10^{19}$ cm$^{-3}$ [246]. For a chemical potential that corresponds to a similar carrier concentration in the unfilled case, the computations reveal a Seebeck coefficient of $-141\,\mu VK^{-1}$, which is slightly smaller than what is predicted experimentally. This result is quite unusual, since theoretical predictions generally rather overestimate the Seebeck coefficient. This underestimation of the Seebeck coefficient from the unfilled skutterudite computations is most probably due to two effects. One might be an insufficient description of the band gap. The other, more important effect, are the changes induced by the fillers on the band structure, which lead to an enhanced Seebeck coefficient. This fact is nicely illustrated by comparing the Seebeck coefficient of pure $CoSb_3$ (see Fig. 4.2b) with the one of 100 % filling 4.11b. Thus filling with indium affects the electronic structure positively, although not very strongly.

All aforementioned transport properties were computed for T= 300 K. As can be seen in Fig. 4.12 the electrical conductivity and the Seebeck coefficient both increase for absolute

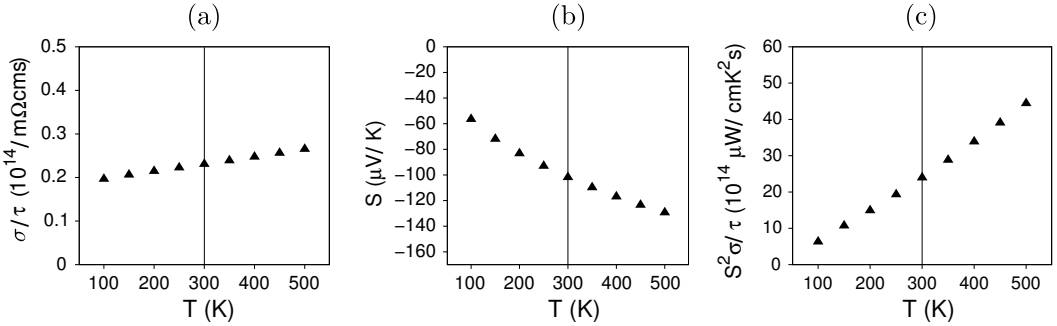


Figure 4.12: Electronic transport properties with respect to the temperature for $CoSb_3$: (a) electrical conductivity, (b) Seebeck coefficient and (c) power factor. The electrical properties of $InCo_4Sb_{12}$ show qualitatively the same temperature dependence compared to $CoSb_3$.

values with increasing temperature, hence does the power factor. This agrees again nicely with experimental results [246]. Consequently, Ga, In, and Tl filled skutterudites should work optimally in high temperature applications. In conclusion, Ga, In, and Tl are ideal filling species, since they do not deteriorate the good electronic properties and, to the contrary, contribute to an enhanced electron transport.

## 4.3 Electron Correlation in Thermoelectrics: PbTe as a Case Study

So far, all the aforementioned and presented results were obtained applying the DFT method and the exchange-correlation functional PBE. The results are in reasonable good agreement with experimental data. This besides the insufficient description of the electron correlation, which is quite underestimated in $CoSb_3$ (see Paper A1). However, including electron correlation in solid state and especially in electron transport properties, is a very challenging task. As a step into this direction, I have investigated the influence of electron correlation by means of local correlation methods (LMP2) in thermoelectric materials and compare it to a variety of standard density functionals and the HF method. For that case, PbTe, the prototypical thermoelectric material, serves as a test candidate. Unfortunately, an extension of the investigation to $CoSb_3$ is difficult. $CoSb_3$ is a narrow band gap semiconductor and as such difficult to describe by local correlation methods. Since periodic LMP2 is still under development, a description of $CoSb_3$ with periodic LMP2 remains a very challenging task.

The calculated DFT results for the lattice parameter, as shown in Tab. 4.4, are quite typical for these types of materials and these trends are reflected by results shown in Paper A1 and Paper A4. While LDA underestimates the lattice parameter, the GGA functionals overestimate it. However, with a deviation of less than 0.7 % LDA is in surprisingly good agreement with experiments. This excellent agreement is most probably due to error cancellations. Deviations for PBE and PW91 are about 2 % compared to experiments and both functionals result in almost the same value. Hybrid functionals perform equally or even much worse, due to a strong overestimation by the HF method. B3PW performs comparably to the GGA functionals, while B3LYP overestimates the lattice parameter by about 3.6 %. The overesti-

mation by HF is large enough that even MP2 leads to no significant improvement.

Since relativistic effects are only included via the core potentials (see Sec. 3.1), parts of the deviations between computed and measured results are most probably due to a neglect of spin-orbit coupling and to some extent relativistic effects. These effects account for about 0.04 Å in the lattice parameter and are much more important for the electronic structure [258]. However, the latter is not considered here. A much bigger source of error, at least for MP2, are the restrictions in the local treatment. This includes the insufficient size of the excitation domain and the rather small basis set.

The trends for the bulk modulus are again very nicely reflected by earlier studies (see Paper A1 and A5). LDA generally overestimates the bulk modulus, while GGA and hybrid functionals rather underestimate it. All methods, however, are in quite good agreement with experiment. HF performs surprisingly well, which does not change much by MP2. The pressure derivatives of the bulk moduli for each method are in very good agreement with each other. Unfortunately, there are no experimental values for the pressure derivative.

The trends change drastically for the cohesive energy. Here, LDA strongly overestimates by about 40 %. GGA functionals still overestimate the cohesive energy by about 25 to 30 %. Hybrid functionals perform already quite well with deviations compared to experiment by about 10 to 15 %. HF underestimates the cohesive energy by 60 %, which shows a large electron correlation contribution. The best result is achieved by MP2, which underestimates the cohesive energy by only about 5 %. These results show, on the one side, that about 50 % of the binding energy in PbTe is due to electron correlation and, on the other side, that standard DFT functionals describe the binding insufficiently. These trends are quite similar for the $CoSb_3$ skutterudite and application of electron correlation methods is an interesting task.

Table 4.4: Lattice parameter ($a_0$ in Å), bulk modulus ($B_0$ in GPa) and its pressure derivative ($B_0'$) together with the lattice and cohesive energy ($E_{lat}$ and $E_{coh}$ in eV) of PbTe for DFT with various functionals, the HF method and the MP2 method.

| Method / Functionals | $a_0$ | $B_0$ / GPa | $B_0'$ | $E_{coh}$ / eV |
|---|---|---|---|---|
| LDA | 6.397 | 49.8 | 4.639 | −7.75 |
| PBE | 6.582 | 39.0 | 4.466 | −6.74 |
| PW91 | 6.574 | 39.8 | 4.497 | −6.22 |
| B3LYP | 6.679 | 36.5 | 4.554 | −5.28 |
| B3PW | 6.560 | 41.5 | 4.554 | −5.55 |
| HF | 6.686 | 48.8 | 3.650 | −1.92 |
| MP2 | 6.641 | 50.3 | 4.723 | −4.44 |
| EXP | [a] 6.438 | [c] 46.8 | | [e] −4.70 |
| EXP | [b] 6.425 | [d] 39.8 | | |

[a] at 120 K [251]; [b] at room temperature [252]; [c] at ∼0 K [253]; [d] at room temperature [254]; [e] obtained from: cohesive energies of the elements [255] and heats of formation of compounds [256, 257]

# Chapter 5

# Conclusions

Although thermoelectric materials are not expected to cope with humanity's energy turnaround by themselves, the admirable progress in enhancing the efficiency of thermoelectric materials cemented their share as niche products in various applications. One very promising class of thermoelectric materials are skutterudites. The presented work reviewed the concept of skutterudites as thermoelectric materials and investigated their peculiar electronic structure and electronic transport properties by means of theoretical first-principles.

Earlier studies on the electronic structure of $CoSb_3$ skutterudites revealed ambiguous results and left open questions concerning for example the size of the energy band gap and the prominent HO band at the $\Gamma$-point. Based on electronic structure computations, the presented work reveals a strong dependence of the electronic structure on the lattice structure. This dependence explains many disagreements of earlier studies. Additionally, the reevaluated and extended orbital model is applied to explain the peculiar shape and dispersion of the HO band. Besides $CoSb_3$, the iron based parent material $FeSb_3$ shows all the typical characteristics of a skutterudite. However, due to the electron deficiency compared to the cobalt based form, the Fermi level is shifted into the valence bands and, hence, $FeSb_3$ bears a striking resemblance to a a p-doped skutterudite. This p-doping character explains very nicely the surprisingly large Seebeck coefficient and the surprisingly large electrical conductivity found in experiment.

Skutterudites allow for two ways to optimized their thermoelectric transport properties. While the first is filling, the second is nanostructuring. Both possibilities mainly aim at reducing the large thermal conductivity of skutterudites. However, they will both only be practical if they leave the good electronic properties undeteriorated. In this study both optimization possibilities are assessed with respect to their electronic properties. The group-13 atoms are found to be ideal doping agents that rather enhance the good electronic transport properties of the parent material. From a structural analysis of filled skutterudites, the study predicts that Ga atoms substitute Sb atoms up to a certain filling threshold. For filling beyond that threshold a comparison to preliminary experimental results shows that Ga occupies the voids sites. Indium and thallium are found to prefer the filling position.

A step towards nanostructuring is taken by analyzing the low-index surfaces of $CoSb_3$. Typically, slabs of these surfaces are off-stoichiometric. Thus, a new model was developed that allows to compute surface energies for symmetric but off-stoichiometric slabs. The (110) surface is found to be the most stable surface, followed by (100) and (111). Bulk projected surface band structures for the three low-index surfaces show that surface states appear at the $CoSb_3$ surfaces and lead to a metallic behavior at the surface. These results are in

good agreement with preliminary conductivity measurements on thin films.

The methodological studies presented in this work show that electron correlation accounts with up to 50 % for a large portion of the binding in thermoelectric materials. An improved description of thermoelectric materials could be achieved by applying high-level wave function based electron correlation methods. Unfortunately, for solids many of these methods are still untested or simply not applicable. This work shows how to generally apply these methods – when they are based on local orbitals – to large and complicated test systems like transition metal fluorides and surfaces. These methods are then applied to the PbTe thermoelectric material and reveal a significant electron correlation contribution to the binding.

# Chapter 6

# Publications

# 6.1 Paper A1

"Electronic structure and the ground-state properties of cobalt antimonide skutterudites: Revisited with different theoretical methods"

L. Hammerschmidt, S. Schlecht, and B. Paulus

Phys. Status Solidi A, **210**, 131-139 (2013)

**DOI** 10.1002/pssa.201228453
**URL** http://dx.doi.org/10.1002/pssa.201228453

## 6.2 Paper A2

"Structural and Thermoelectric Properties of $FeSb_3$ Skutterudite Thin Films"

M. V. Daniel, L. Hammerschmidt, C. Schmidt, F. Timmermann, J. Franke, G. Beddies, N. Jöhrmann, M. Hietschold, D. C. Johnson, B. Paulus, and M. Albrecht

Phys. Rev. B, **91**, 085410 (2015)

**DOI** 10.1103/PhysRevB.91.085410
**URL** http://dx.doi.org/10.1103/PhysRevB.91.085410

## 6.3 Paper A3

"Low-index Surfaces of $CoSb_3$ Skutterudites From First Principles"

L. Hammerschmidt, M. Quennet, K. Töpfer and B. Paulus

Surf. Sci., **637-638**, 124-131 (2015)

**DOI** 10.1016/j.susc.2015.03.020
**URL** http://dx.doi.org/10.1016/j.susc.2015.03.020

## 6.4 Paper A4

"Electron Correlation at the $MgF_2$ (110) Surface: A Comparison of Incremental and Local Correlation Methods"

L. Hammerschmidt, L. Maschio, C. Müller, and B. Paulus

J. Chem. Theor. Comput., **11**, 252-259 (2015)

**DOI** 10.1021/ct500841b
**URL** http://dx.doi.org/10.1021/ct500841b

# 6.5 Paper A5

"*Ab Initio* Investigation of Ground-State Properties of Group-12 Fluorides"

S. Torabi, L. Hammerschmidt, E. Voloshina, and B. Paulus

Int. J. Quant. Chem., **114**, 943-951 (2014)

**DOI** 10.1002/qua.24695
**URL** http://dx.doi.org/10.1002/qua.24695

# Bibliography


[1] Bundesministerium für Wirtschaft und Energie (Hrsg.); *Energiedaten: Gesamtausgabe (Stand: November 2014)*, Berlin, **2014**. http://www.bmwi.de/BMWi/Redaktion/PDF/E/energiestatistiken-grafiken (last accessed 30.01.2015).

[2] Snyder, G. J.; Toberer, E. *Nat. Mater.* **2008**, *7*, 105–114.

[3] Bell, L. E. *Science* **2008**, *321*, 1457–1461.

[4] DiSalvo, F. J. *Science* **1999**, *285*, 703–706.

[5] Lindley, D. *Nature* **2009**, *458*, 138–141.

[6] Vining, C. B. *Nature* **2003**, *423*, 391–392.

[7] Yang, J.; Caillat, T. *MRS Bulletin* **2006**, *31*, 224–229.

[8] Heremans, J. P. *Nature* **2014**, *508*, 327–328.

[9] Zhang, Q.; Sun, Y.; Xu, W.; Zhu, D. *Adv. Mater.* **2014**, *26*, 6829–6851.

[10] Li, J.-F.; Liu, W.-S.; Zhao, L.-D.; Zhou, M. *NPG Asia Mater.* **2010**, *2*, 152–158.

[11] Goldsmid, H. J. *Introduction to Thermoelectricity*, Vol. 121 of *Springer Series in Materials Science;* Springer: Berlin Heidelberg, 2010.

[12] Vining, C. B. *Nat. Mater.* **2009**, *8*, 83–85.

[13] Seebeck, T. J. *Annalen der Physik* **1826**, *82(2)*, 133–160.

[14] Peltier, J. C. A. *Annales de Chimie et de Physique* **1834**, *LVI*, 371–387.

[15] Thomson, W. *Proceedings of the Royal Society of Edinburgh* **1851**, *III*, 91–98.

[16] Thomson, W. *Proc. R. Soc. Lond.* **1854**, *7*, 49–58.

[17] Altenkirch, E. *Physikalische Zeitschrift* **1909**, *10*, 560–568.

[18] Altenkirch, E. *Physikalische Zeitschrift* **1911**, *12*, 920–924.

[19] Ioffe, A. F. *Semiconductor Thermoelements and Thermoelectric Cooling;* Infosearch: Michigan, 1st ed., 1957.

[20] Rowe, D. M. *CRC Handbook of Thermoelectrics;* CRC Press: Florida, 1st ed., 1995.

[21] Slack, G. A. In *Solid State Physics*; Seitz, F., Turnbull, D., Ehrenreich, H., Eds., Vol. 34; Academic Press: New York, 1979.

[22] Mahan, G. D. *J. Appl. Phys.* **1989**, *65*, 1578.

[23] Goldsmid, H. J. *Electron Refrigeration;* Pion Limited: London, 1986.

[24] Beekman, M.; Nolas, G. S. *J. Mater. Chem.* **2008**, *18*, 842.

[25] Nolas, G. S.; Beekman, M.; Gryko, J.; Lamberton Jr., G. A.; Tritt, T. M.; McMillan, P. F. *Appl. Phys. Lett.* **2003**, *82*, 910.

[26] Sootsman, J. R.; Chung, D. Y.; Kanatzidis, M. G. *Angew. Chem. Int. Ed.* **2009**, *48*, 8616.

[27] Christensen, M.; Abrahamsen, A. B.; Christensen, N. B.; Juranyi, F.; Andersen, N. H.; Lefmann, K.; Andreasson, J.; Bahl, C. R. H.; Iversen, B. B. *Nat. Mater.* **2008**, *7*, 811.

[28] Tse, J. S.; Shpakov, V. P.; Murashov, V. V.; Belosludov, V. R. *J. Chem. Phys.* **1997**, *107*, 9271.

[29] Sales, B. C.; Mandrus, D.; Williams, R. K. *Science* **1996**, *272*, 1325.

[30] Sales, B. C.; Mandrus, D.; Chakoumakos, B. C.; Keppens, V.; Thompson, J. R. *Phys. Rev. B* **1997**, *56*, 15081.

[31] Sales, B. C.; Chakoumakos, B. C.; Mandrus, D. *Phys. Rev. B* **2000**, *61*, 2475.

[32] Nolas, G. S.; Morelli, D. T.; Tritt, T. M. *Annu. Rev. Mater. Sci.* **1999**, *29*, 89.

[33] Shi, X.; Yang, J.; Salvador, J. R.; Chi, M.; Cho, J. Y.; Wang, H.; Bai, S.; Yang, J.; Zhang, W.; Chen, L. *J. Am. Chem. Soc.* **2011**, *133*, 7837–7846.

[34] Koza, M. M.; Johnson, M. R.; Viennois, R.; Mutka, H.; Girard, L.; Ravot, D. *Nat. Mater.* **2008**, *7*, 805.

[35] Minnich, A. J.; Dresselhaus, M. S.; Ren, Z. F.; Chen, G. *Energy Environ. Sci.* **2009**, *2*, 466–479.

[36] Nielsch, K.; Bachmann, J.; Kimling, J.; Böttner, H. *Adv. Energy Mater.* **2011**, *1*, 713.

[37] Kanatzidis, M. G. *Chem. Mater.* **2010**, *22*, 648–659.

[38] Hicks, L. D.; Dresselhaus, M. S. *Phys. Rev. B* **1993**, *47*, 12727–12731.

[39] Wang, K. L.; Balandin, A. A. In *Optics of Nanostructured Materials*; Markel, V., George, T., Eds.; Wiley: New York, 2001; page 515.

[40] Harman, T.; Taylor, P.; Spears, D.; Walsh, M. *J. Electron. Mater* **2000**, *29*, L1–L2.

[41] Khitun, A.; Balandin, A.; Liu, J. L.; Wang, K. L. *J. Appl. Phys.* **2000**, *88*, 696–699.

[42] Balandin, A. A.; Lazarenkova, O. L. *Appl. Phys. Lett.* **2003**, *82*, 415–417.

[43] Hicks, L. D.; Dresselhaus, M. S. *Phys. Rev. B* **1993**, *47*, 16631–16634.

[44] Walkauskas, S. G.; Broido, D. A.; Kempa, K.; Reinecke, T. L. *J. Appl. Phys.* **1999**, *85*, 2579–2582.

[45] Broido, D. A.; Reinecke, T. L. *Appl. Phys. Lett.* **1995**, *67*, 100–102.

[46] Melnichuk, S.; Kosyachenko, S.; Vozny, M. In *Thermoelectrics, 1997. Proceedings ICT '97. XVI International Conference on*, pages 438–441, 1997.

[47] Harman, T. C.; Taylor, P. J.; Walsh, M. P.; LaForge, B. E. *Science* **2002**, *297*, 2229–2232.

[48] Venkatasubramanian, R.; Siivola, E.; Colpitts, T.; O'Quinn, B. *Nature* **2001**, *413*, 6856.

[49] Venkatasubramanian, R. *Phys. Rev. B* **2000**, *61*, 3091–3097.

[50] Venkatasubramanian, R.; Colpitts, T.; Watko, E.; Lamvik, M.; El-Masry, N. *J. Cryst. Growth* **1997**, *170*, 817–821.

[51] Kanatzidis, M. G. *Semicond. Semimetals* **2000**, *69*, 51.

[52] Sales, B. C. *Science* **2002**, *295*, 1248–1249.

[53] Sze, S. M. *Physics of Semiconductor Device;* Wiley Interscience Publication: New York, 1981.

[54] Dughaish, Z. *Physica B: Condensed Matter* **2002**, *322*, 205–223.

[55] Ravich, Y. I.; Efimova, B. A.; Smirnov, I. A. *Semiconducting Lead Chalcogenides;* Band 5, Plenum: New York, 1970.

[56] Ahmad, S.; Mahanti, S. D.; Hoang, K.; Kanatzidis, M. G. *Phys. Rev. B* **2006**, *74*, 155205.

[57] Heremans, J. P.; Jovovic, V.; Toberer, E. S.; Saramat, A.; Kurosaki, K.; Charoenphakdee, A.; Yamanaka, S.; Snyder, G. J. *Science* **2008**, *321*, 554–557.

[58] Poudeu, P. F. P.; D'Angelo, J.; Downey, A.; Pcionek, R.; Sootsman, J.; Zhou, Z.; Palchik, O.; Hogan, T. P.; Uther, C.; Kanatzidis, M. G. *Mater. Res. Soc. Symp. Proc.* **2006**, *886*, 195.

[59] Poudeu, P. F. P.; D'Angelo, J.; Kong, H.; Downey, A.; Short, J. L.; Pcionek, R.; Hogan, T. P.; Uher, C.; Kanatzidis, M. G. *J. Am. Chem. Soc.* **2006**, *128*, 14347–14355.

[60] Biswas, K.; He, J.; Blum, I. D.; Wu, C.-I.; Hogan, T. P.; Seidman, D. N.; Dravid, V. P.; Kanatzidis, M. G. *Nature* **2012**, *489*, 414–418.

[61] Heremans, J. P.; Thrush, C. M.; Morelli, D. T. *Phys. Rev. B* **2004**, *70*, 115334.

[62] Hsu, K. F.; Loo, S.; Guo, F.; Chen, W.; Dyck, J. S.; Uher, C.; Hogan, T.; Polychroniadis, E. K.; Kanatzidis, M. G. *Science* **2004**, *303*, 818–821.

[63] Ni, J.; Case, E. *J. Electron. Mater* **2013**, *42*, 1382–1388.

[64] Chen, N.; Gascoin, F.; Snyder, G. J.; Müller, E.; Karpinski, G.; Stiewe, C. *Appl. Phys. Lett.* **2005**, *87*, 171903.

[65] Androulakis, J.; Hsu, K. F.; Pcionek, R.; Kong, H.; Uher, C.; D'Angelo, J. J.; Downey, A.; Hogan, T.; Kanatzidis, M. G. *Advanced Materials* **2006**, *18*, 1170–1173.

[66] Hummer, K.; Grüneis, A.; Kresse, G. *Phys. Rev. B* **2007**, *75*, 195211.

[67] Mahanti, S. D.; Bilc, D. *Journal of Physics: Condensed Matter* **2004**, *16*, S5277.

[68] Venkatapathi, S.; Dong, B.; Hin, C. *J. Appl. Phys.* **2014**, *116*, 013708–013708–4.

[69] Shiga, T.; Shiomi, J.; Ma, J.; Delaire, O.; Radzynski, T.; Lusakowski, A.; Esfarjani, K.; Chen, G. *Phys. Rev. B* **2012**, *85*, 155203.

[70] Zhang, Y.; Ke, X.; Chen, C.; Yang, J.; Kent, P. R. C. *Phys. Rev. B* **2009**, *80*, 024304.

[71] Hoang, K.; Mahanti, S. D.; Kanatzidis, M. G. *Phys. Rev. B* **2010**, *81*, 115106.

[72] Hoang, K.; Mahanti, S. D.; Salvador, J. R.; Kanatzidis, M. G. *Phys. Rev. Lett.* **2007**, *99*, 156403.

[73] Ke, X.; Chen, C.; Yang, J.; Wu, L.; Zhou, J.; Li, Q.; Zhu, Y.; Kent, P. R. C. *Phys. Rev. Lett.* **2009**, *103*, 145502.

[74] Hazama, H.; Mizutani, U.; Asahi, R. *Phys. Rev. B* **2006**, *73*, 115108.

[75] Breithaupt, A. *Annalen der Physik und Chemie* **1827**, *9*, 115–116.

[76] Boebert, K. F. *Über das Modumer Blaufarbenwerk in Norwegen;* Archiv für Mineralogie, Geognosie, Bergbau und Hüttenkunde. G. Reimer: Berlin, 1847.

[77] Rowe, D. M. *Thermoelectrics Handbook: Macro to Nano;* CRC Press / Taylor and Francis: Florida, 1st ed., 2005.

[78] Schmidt, T.; Kliche, G.; Lutz, H. D. *Acta Crystallogr.* **1987**, *C43*, 1678.

[79] Jeitschko, W.; Braun, D. *Acta Crystallogr. B* **1977**, *33*, 3401–3406.

[80] Braun, D.; Jeitschko, W. *Journal of the Less Common Metals* **1980**, *72*, 147 – 156.

[81] Braun, D. J.; Jeitschko, W. *Journal of Solid State Chemistry* **1980**, *32*, 357 – 363.

[82] Braun, D.; Jeitschko, W. *Journal of the Less Common Metals* **1980**, *76*, 33 – 40.

[83] Noh, M.; Thiel, J.; Johnson, D. C. *Science* **1995**, *270*, 1181–1184.

[84] Hornbostel, M. D.; Hyer, E. J.; Thiel, J.; Johnson, D. C. *J. Am. Chem. Soc.* **1997**, *119*, 2665–2668.

[85] Möchel, A.; Sergueev, I.; Nguyen, N.; Long, G. J.; Grandjean, F.; Johnson, D. C.; Hermann, R. P. *Phys. Rev. B* **2011**, *84*, 064302.

[86] Sales, B. C. In *Handbook on the Physics and Chemistry of the Rare Earths*; Gschneider, K. A., Ed., Vol. 33; Elsevier: New York, 2003.

[87] Uher, C. In *Recent Trends in Thermoelectric Materials Research I*; Tritt, T. M., Ed., Vol. 69 of *Semiconductors and Semimetals;* Elsevier, 2001; pages 139 – 253.

[88] Morelli, D. T.; Meisner, G. P. *J. Appl. Phys.* **1995**, *77*, 3777–3781.

[89] Nolas, G. S.; Kaeser, M.; Littleton, R. T.; Tritt, T. M. *Appl. Phys. Lett.* **2000**, *77*, 1855–1857.

[90] Tang, X.; Chen, L.; Goto, T.; Hirai, T. *J. Mater. Res.* **2001**, *16*, 837.

[91] Nolas, G. S.; Sharp, J.; Goldsmid, H. J. *Thermoelectrics: Basic principles and new materials developments*, Vol. 45 of *Springer Series in Material Science;* Springer, 2001.

[92] Keppens, V.; Mandrus, D.; Sales, B. C.; Chakoumakos, B. C.; Dai, P.; Coldea, R.; Maple, M. B.; Gajewski, D. A.; Freeman, E. J.; Bennington, S. *Nature* **1998**, *395*, 876–878.

[93] Kitagawa, H.; Hasaka, M.; Morimura, T.; Nakashima, H.; ichiro Kondo, S. *Mater. Res. Bull.* **2000**, *35*, 185.

[94] Grytsiv, A.; Rogl, P.; Berger, S.; Paul, C.; Bauer, E.; Godart, C.; Ni, B.; Abd-Elmeguid, M. M.; Saccone, A.; Ferro, R.; Kaczorowski, D. *Phys. Rev. B* **2002**, *66*, 094411.

[95] Lu, Q. M.; Zhang, J. X.; Zhang, X.; Liu, Y. Q.; Liu, D. M.; Zhou, M. L. *J. Appl. Phys.* **2005**, *98*, 106107.

[96] Bérardan, D.; Alleno, E.; Godart, C.; Puyet, M.; Lenoir, B.; Lackner, R.; Bauer, E.; Girard, L.; Ravot, D. *J. Appl. Phys.* **2005**, *98*, 033710.

[97] Schnelle, W.; Leithe-Jasper, A.; Rosner, H.; Cardoso-Gil, R.; Gumeniuk, R.; Trots, D.; Mydosh, J. A.; Grin, Y. *Phys. Rev. B* **2008**, *77*, 094421.

[98] Tang, X.; Zhang, Q.; Chen, L.; Goto, T.; Hirai, T. *J. Appl. Phys.* **2005**, *97*, 093712.

[99] Puyet, M.; Dauscher, A.; Lenoir, B.; Dehmas, M.; Stiewe, C.; Müller, E.; Hejtmanek, J. *J. Appl. Phys.* **2005**, *97*, 083712.

[100] Dyck, J. S.; Chen, W.; Uher, C.; Chen, L.; Tang, X.; Hirai, T. *J. Appl. Phys.* **2002**, *91*, 3698–3705.

[101] Puyet, M.; Lenoir, B.; Dauscher, A.; Dehmas, M.; Stiewe, C.; Müller, E. *J. Appl. Phys.* **2004**, *95*, 4852–4855.

[102] Shi, X.; Zhang, W.; Chen, L. D.; Yang, J. *Phys. Rev. Lett.* **2005**, *95*, 185503.

[103] Hermann, R. P.; Jin, R.; Schweika, W.; Grandjean, F.; Mandrus, D.; Sales, B. C.; Long, G. J. *Phys. Rev. Lett.* **2003**, *90*, 135505.

[104] Williams, J. R.; Johnson, M.; Johnson, D. C. *J. Am. Chem. Soc.* **2001**, *123*, 1645–1649.

[105] Ackermann, J.; Wold, A. *J. Phys. Chem. Solids* **1977**, *38*, 1013.

[106] Singh, D. J.; Pickett, W. E. *Phys. Rev. B* **1994**, *50*, 11235.

[107] Dudkin, L. D.; Abrikosov, N. K. *Zh. Neorg. Khim.* **1956**, *1*, 2096.

[108] Smith, J. C.; Banerjee, S.; Pardo, V.; Pickett, W. E. *Phys. Rev. Lett.* **2011**, *106*, 056401.

[109] Caillat, T.; Borshchevsky, A.; Fleurias, J.-P. *J. Appl. Phys.* **1996**, *80*, 4442.

[110] Kurmaev, E. Z.; Moewes, A.; Shein, I. R.; Finkelstein, L. D.; Ivanovskii, A. K.; Anno, H. *J. Phys.: Condens. Matter* **2004**, *16*, 979.

[111] Arushanov, E.; Respaud, M.; Rakoto, H.; Broto, J. M.; Caillat, T. *Phys. Rev. B* **2000**, *61*, 4672–4676.

[112] Sofo, J. S.; Mahan, G. D. *Phys. Rev. B* **1998**, *58*, 15620.

[113] Lefebvre-Devos, I.; Lassalle, M.; Wallart, X.; Olivier-Fourcade, J.; Monconduit, L.; Jumas, J. C. *Phys. Rev. B* **2001**, *63*, 125110.

[114] Lu, P.-X.; Ma, Q.-H.; Li, Y.; Hu, X. *J. Magn. Magn. Mater.* **2010**, *322*, 3080.

[115] Bertini, L.; Cenedese, S. *Phys. Status Solidi RRL* **2007**, *1*, 244.

[116] Pardo, V.; Smith, J. C.; Pickett, W. E. *Phys. Rev. B* **2012**, *85*, 214531.

[117] Toprak, M. S.; Stiewe, C.; Platzek, D.; Williams, S.; Bertini, L.; Müller, E.; Gatti, C.; Zhang, Y.; Rowe, M.; Muhammed, M. *Advanced Functional Materials* **2004**, *14*, 1189–1196.

[118] Pyykkö, P.; Stanton, J. F. *Chemical Reviews* **2012**, *112*, 1–3.

[119] Cramer, C. J.; Truhlar, D. G. *Phys. Chem. Chem. Phys.* **2009**, *11*, 10757–10816.

[120] Sholl, D. S.; Steckel, J. A. *Density Functional Theory: A practical Introduction;* Wiley: Hoboken, New Jersey, 2009.

[121] Cohen, A. J.; Mori-Sánchez, P.; Yang, W. *Chemical Reviews* **2012**, *112*, 289–320.

[122] Krityán, S.; Pulay, P. *Chem. Phys. Lett.* **1994**, *229*, 175.

[123] Hobza, P.; Sponer, J.; Reschel, T. *J. Comp. Chem.* **1995**, *16*, 1315.

[124] Pérez-Jordá, J. M.; Becke, A. D. *Chem. Phys. Lett.* **1995**, *233*, 134.

[125] Pérez-Jordá, J. M.; San-Fabián, E.; Pérez-Jiménez, A. J. *J. Chem. Phys.* **1999**, *110*, 1916.

[126] Binnie, S.; Sola, E.; Alfè, D.; Gillan, M. *Mol. Simul.* **2009**, *35*, 609–612.

[127] Grimme, S. *J. Comput. Chem.* **2006**, *27*, 1787–1799.

[128] Grimme, S.; Antony, J.; Ehrlich, S.; Krieg, H. *J. Chem. Phys.* **2010**, *132*, 154104.

[129] Civalleri, B.; Zicovich-Wilson, C.; Valenzano, L.; Ugliengo, P. *Cryst. Eng. Comm.* **2008**, *10*, 405–410.

[130] de-la Roza, A. O.; Johnson, E. R. *J. Chem. Phys.* **2012**, *137*, 054103.

[131] Tkatchenko, A.; Scheffler, M. *Phys. Rev. Lett.* **2009**, *102*, 073005.

[132] Dion, M.; Rydberg, H.; Schröder, E.; Langreth, D. C.; Lundqvist, B. I. *Phys. Rev. Lett.* **2004**, *92*, 246401.

[133] Vydrov, O. A.; Van Voorhis, T. *J. Chem. Phys.* **2010**, *133*, 244103.

[134] Schatschneider, B.; Liang, J.; Reilly, A. M.; Marom, N.; Zhang, G. X.; Tkatchenko, A. *Phys. Rev. B* **2013**, *87*, 060104.

[135] Grimme, S. *J. Chem. Phys.* **2006**, *124*, 034108.

[136] Sharkas, K.; Toulouse, J.; Savin, A. *J. Chem. Phys.* **2011**, *134*, 064113.

[137] Sharkas, K.; Toulouse, J.; Maschio, L.; Civalleri, B. *J. Chem. Phys.* **2014**, *141*, 044105.

[138] Cizek, J. *Adv. Chem. Phys.* **1969**, *14*, 35.

[139] Møller, C.; Plesset, M. S. *Phys. Rev.* **1934**, *46*, 618.

[140] Muller, C.; Paulus, B. *Phys. Chem. Chem. Phys.* **2012**, *14*, 7605–7614.

[141] Stollhoff, G.; Fulde, P. *Z. Phys. B* **1977**, *26*, 257–262.

[142] Stollhoff, G.; Fulde, P. *J. Chem. Phys.* **1980**, *73*, 4548–4561.

[143] Stollhoff, G. *J. Chem. Phys.* **1996**, *105*, 227–234.

[144] Pulay, P. *Chem. Phys. Lett.* **1983**, *100*, 151–154.

[145] Pulay, P.; Saebø, S. *Theoret. Chim. Acta* **1986**, *69*, 357–368.

[146] Saebø, S.; Pulay, P. *J. Chem. Phys.* **1987**, *86*, 914–921.

[147] Molpro, version 2012.1, a package of ab initio programs. Werner, H.-J.; Knowles, P. J.; Knizia, G.; Manby, F. R.; Schütz, M.; Celani, P.; Korona, T.; Lindh, R.; Mitrushenkov, A.; Rauhut, G.; Shamasundar, K. R.; Adler, T. B.; Amos, R. D.; Bernhardsson, A.; Berning, A.; Cooper, D. L.; Deegan, M. J. O.; Dobbyn, A. J.; Eckert, F.; Goll, E.; Hampel, C.; Hesselmann, A.; Hetzer, G.; Hrenar, T.; Jansen, G.; Köppl, C.; Liu, Y.; Lloyd, A. W.; Mata, R. A.; May, A. J.; McNicholas, S. J.; Meyer, W.; Mura, M. E.; Nicklass, A.; O'Neill, D. P.; Palmieri, P.; Peng, D.; Pflüger, K.; Pitzer, R.; Reiher, M.; Shiozaki, T.; Stoll, H.; Stone, A. J.; Tarroni, R.; Thorsteinsson, T.; Wang, M. **2012**.

[148] Werner, H.-J.; Knowles, P. J.; Knizia, G.; Manby, F. R.; Schütz, M. *WIREs Comput. Mol. Sci.* **2012**, *2*, 242–253.

[149] Pisani, C.; Maschio, L.; Casassa, S.; Halo, M.; Schütz, M.; Usvyat, D. *J. Comput. Chem.* **2008**, *29*, 2113.

[150] Pisani, C.; Busso, M.; Capecchi, G.; Casassa, S.; Dovesi, R.; Maschio, L.; Zicovich-Wilson, C.; Schütz, M. *J. Chem. Phys.* **2005**, *122*, 094113.

[151] Pisani, C.; Schutz, M.; Casassa, S.; Usvyat, D.; Maschio, L.; Lorenz, M.; Erba, A. *Phys. Chem. Chem. Phys.* **2012**, *14*, 7615–7628.

[152] Stoll, H. *Chem. Phys. Lett.* **1992**, *191*, 548.

[153] Stoll, H. *J. Chem. Phys.* **1992**, *97*, 8449.

[154] Stoll, H. *Phys. Rev. B* **1992**, *46*, 6700.

[155] Paulus, B. *Phys. Rep.* **2006**, *428*, 1.

[156] Shukla, A.; Dolg, M.; Fulde, P.; Stoll, H. *Phys. Rev. B* **1999**, *60*, 5211–5216.

[157] Abdurahman, A.; Shukla, A.; Dolg, M. *J. Chem. Phys.* **2000**, *112*, 4801–4805.

[158] Manby, F. R.; Alfe, D.; Gillan, M. J. *Phys. Chem. Chem. Phys.* **2006**, *8*, 5178–5180.

[159] Martinez-Casado, R.; Mallia, G.; Usvyat, D.; Maschio, L.; Cassassa, S.; Schütz, M.; Harrison, N. M. *J. Chem. Phys.* **2011**, *134*, 014706.

[160] Halo, M.; Cassassa, S.; Maschio, L.; Pisani, C.; Dovesi, R.; Ehinon, D.; Baraille, I.; Rérat, M.; Usvyat, D. *Phys. Chem. Chem. Phys.* **2011**, *13*, 4434–4443.

[161] Usvyat, D.; Sadeghian, K.; Maschio, L.; Schütz, M. *Phys. Rev. B* **2012**, *86*, 045412.

[162] Müller, C.; Paulus, B.; Hermansson, K. *Surf. Sci.* **2009**, *603*, 2619.

[163] Müller, C.; Herschend, B.; Hermansson, K.; Paulus, B. *J. Chem. Phys.* **2008**, *128*, 214701.

[164] Müller, C.; Hermansson, K.; Paulus, B. *Chem. Phys.* **2009**, *362*, 91–96.

[165] Staemmler, V. *J. Phys. Chem. A* **2011**, *115*, 7153–7160.

[166] Hammerschmidt, L.; Müller, C.; Paulus, B. *J. Chem. Phys.* **2012**, *136*, 124117.

[167] Gilman, J. J. *J. Appl. Phys.* **1960**, *31*, 2208–2218.

[168] Gutshall, P. L.; Gross, G. E. *J. Appl. Phys.* **1965**, *36*, 2459–2460.

[169] Kraatz, P.; Zoltai, T. *J. Appl. Phys.* **1974**, *45*, 4741–4750.

[170] Burns, S. J.; Webb, W. W. *J. Appl. Phys.* **1970**, *41*, 2086–2095.

[171] Born, M.; Heisenberg, W.; Jordan, P. *Z. Phys.* **1925**, *35*, 557.

[172] Schrödinger, E. *Phys. Rev.* **1926**, *37*, 863.

[173] Popelier, P. *Solving the Schrödinger Equation: Has Everything Been Tried?;* Imperial College Press: London, 2011.

[174] Schwerdtfeger, P. *Chem. Phys. Chem.* **2011**, *12*, 3143–3155.

[175] Born, M.; Oppenheimer, R. *Annalen der Physik* **1927**, *84*, 457.

[176] Szabo, A.; Ostlund, N. S. *Modern Quantum Chemistry;* Dover Publication, Inc: Mineola, New York, 1st ed., 1996.

[177] Fock, V. *Z. Phys.* **1930**, *51*, 126.

[178] Slater, J. C. *Phys. Rev.* **1951**, *81*, 385.

[179] Roothaan, C. C. J. *Rev. Mod. Phys.* **1951**, *23*, 69.

[180] Hall, G. G. *Proc. R. Soc. Lond.* **1951**, *205*, 541.

[181] Parr, R. G.; Yang, W. *Density-Functional Theory of Atoms and Molecues;* Oxford University Press: Oxford, 1989.

[182] Thomas, L. H. *Proc. Campr. Phil. Soc.* **1927**, *23*, 542.

[183] Fermi, E. *Z. Phys.* **1928**, *48*, 73.

[184] Hohenberg, P.; Kohn, W. *Phys. Rev.* **1964**, *136*, B864.

[185] Ceperley, D. M.; Alder, B. J. *Phys. Rev. Lett.* **1980**, *45*, 566–569.

[186] Vosko, S. H.; Wilk, L.; Nusair, M. *Can. J. Phys.* **1980**, *58*, 1200.

[187] Dirac, P. A. M. *Proc. Cambridge Philos. Soc.* **1930**, *26*, 376.

[188] Perdew, J. P.; Burke, K.; Ernzerhof, M. *Phys. Rev. Lett.* **1996**, *77*, 3865.

[189] Perdew, J. P.; Wang, Y. *Phys. Rev. B* **1992**, *45*, 13244.

[190] Becke, A. D. *Phys. Rev. A* **1988**, *38*, 3098.

[191] Lee, C.; Yang, W.; Parr, R. G. *Phys. Rev. B* **1988**, *37*, 785.

[192] Bartlett, R. J. *Ann. Rev. Phys. Chem.* **1981**, *32*, 359–401.

[193] Shavitt, I. In *Methods of Electronic Structure Theory*; Schaefer, H. F., Ed., Vol. 3; Plenum Press: New York, 1977; chapter 6, pages 189–275.

[194] Jensen, F. *Introduction to Computational Chemistry;* John Wiley & Sons: West Sussex, 2nd ed., 2001.

[195] T. D. Crawford, H. F. S. *Rev. Comput. Chem.* **2000**, *14*, 33.

[196] Bartlett, R. J.; Musiał, M. *Rev. Mod. Phys.* **2007**, *79*, 291–352.

[197] Rayleigh, J. W. S. *Theory of Sound* **1894**, *1*, 115.

[198] Schrödinger, E. *Annalen der Physik* **1926**, *80*, 437.

[199] Ashcroft, N. W.; Mermin, D. N. *Solid State Physics;* CBS Publishing ASIA LTD.: Philadelphia, 1976.

[200] Bloch, F. *Z. Phys.* **1928**, *52*, 555.

[201] Pisani, C. *Quantum-Mechanical Ab-initio calculation of the Properties of Crystalline Materials*, Vol. 67 of *Lecture Notes in Chemistry;* Springer Verlag: Heidelberg, 1996.

[202] André, J. M.; Gouverneur, L.; Leroy, G. *Int. J. Quantum Chem.* **1967**, *1*, 427.

[203] André, J. M.; Gouverneur, L.; Leroy, G. *Int. J. Quantum Chem.* **1967**, *1*, 451.

[204] André, J. M. *J. Chem. Phys.* **1969**, *50*, 1536.

[205] Saunders, V. R.; Freyria Fava, C.; Dovesi, R.; Salasco, L.; Roetti, C. *Mol. Phys.* **1992**, *77*, 629–665.

[206] Hafner, J. *J. Comput. Chem.* **2008**, *29*, 2044–2078.

[207] Kresse, G.; Hafner, J. *Phys. Rev. B* **1993**, *47*, 558.

[208] Kresse, G.; Hafner, J. *Phys. Rev. B* **1994**, *49*, 14251.

[209] Kresse, G.; Furthmüller, J. *Comput. Mat. Sci.* **1996**, *6*, 15.

[210] Kresse, G.; Furthmüller, J. *Phys. Rev. B* **1996**, *54*, 11169.

[211] Blöchl, P. E. *Phys. Rev. B* **1994**, *50*, 17953.

[212] Dovesi, R.; Orlando, R.; Erba, A.; Zicovich-Wilson, C. M.; Civalleri, B.; Casassa, S.; Maschio, L.; Ferrabone, M.; Pierre, M. D. L.; D'Arco, P.; Noel, Y.; Causa, M.; Rerat, M.; Kirtman, B. *Int. J. Quantum Chem.* **2014**, *114*, 1287.

[213] Dovesi, R.; Saunders, V. R.; Roetti, C.; Orlando, R.; Zicovich-Wilson, C. M.; Pascale, F.; Civalleri, B.; Doll, K.; Harrison, N. M.; Bush, I. J.; D'Arco, P.; Llunell, M.; Causa, M.; Noel, Y. *CRYSTAL14, User's Manual;* University of Torino: Torino, 2014.

[214] Hoffmann, R. *Solids and Surfaces: A chemists view of Bonding in Extended Structures;* VCH: Weinheim, 1988.

[215] Allen, P. B. *Boltzmann Theory and Resistivity of Metals;* in: J. R. Chellkowsky and S. G. Louie (Eds.), Quantum Theory of Real Materials, Kluwer, Boston, 1996.

[216] Ziman, J. M. *Electrons and Phonons;* Oxford Classics Series, Clerendon Press, Oxford, 2001.

[217] Singh, J. *Modern Physics for Engineers;* Wiley-VCH, 2004.

[218] Czycholl, G. *Theoretische Festkörperphysik: Von den klassischen Modellen zu modernen Forschungsthemen;* Springer, 2008.

[219] Ibach, H.; Lüth, H. *Festkörperphysik;* Springer, 1995.

[220] Quinn, J. J.; Yi, K.-S. *Solid State Physics;* Springer, 2009.

[221] Goupil, C.; Seifert, W.; Zabrocki, K.; Müller, E.; Snyder, G. J. *Entropy* **2011**, *13(8)*, 1481–1517.

[222] Ohm, G. S. *Die galvanische Kette, mathematisch bearbeitet;* T. H. Riemann: Berlin, 1827.

[223] Madsen, G. K. H.; Singh, D. J. *Comput. Phys. Commun.* **2006**, *175*, 67.

[224] Krause, C.; Werner, H.-J. *Phys. Chem. Chem. Phys.* **2012**, *14*, 7591–7604.

[225] Zalesny, R., Papadopoulos, M. G., Mezey, P. G., Leszczynski, J., Eds. *Linear-Scaling Techniques in Computational Chemistry and Physics*, Vol. 13; Springer Netherlands, 2011.

[226] Müller, C.; Usvyat, D.; Stoll, H. *Phys. Rev. B* **2011**, *83*, 245136.

[227] Boys, S. F. *Rev. Mod. Phys.* **1960**, *32*, 296.

[228] Foster, J. M.; Boys, S. F. *Rev. Mod. Phys.* **1960**, *32*, 300.

[229] Pipek, J.; Mezey, P. G. *J. Chem. Phys.* **1989**, *90*, 4916.

[230] Zicovich-Wilson, C. M.; Dovesi, R.; Saunders, V. R. *J. Chem. Phys.* **2001**, *115*, 9708.

[231] Zicovich-Wilson, C. M.; Bert, A.; Roetti, C.; Dovesi, R.; Saunders, V. R. *J. Chem. Phys.* **2002**, *116*, 1121.

[232] Pulay, P.; Saebø, S. *Theoret. Chim. Acta* **1986**, *69*, 357–368.

[233] Pulay, P. *Chem. Phys. Lett.* **1980**, *73*, 393 – 398.

[234] Metz, B.; Stoll, H.; Dolg, M. *J. Chem. Phys.* **2000**, *113*, 2563–2569.

[235] Peterson, K. A. *J. Chem. Phys.* **2003**, *119*, 11099.

[236] Peterson, K. A. *J. Chem. Phys.* **2003**, *119*, 11113.

[237] Stoll, H.; Metz, B.; Dolg, M. *J. Comput. Chem.* **2002**, *23*, 767.

[238] Hattig, C.; Schmitz, G.; Koßmann, J. *Phys. Chem. Chem. Phys.* **2012**, *14*, 6549–6555.

[239] Herschend, B.; Baudin, M.; Hermansson, K. *J. Chem. Phys.* **2004**, *120*, 4939.

[240] Müller, C.; Hermansson, K. *Surf. Sci.* **2009**, *603*, 3329.

[241] Gay, J. G.; Smith, J. R.; Richter, R.; Arlinghaus, F. J.; Wagoner, R. H. *J. Vac. Sci. Technol. A* **1984**, *2*, 931.

[242] Müller, E.; Schmitz, A. personal communications.

[243] Lorenz, M. *Density fitted local configuration interaction singles method for calculating optical band gaps in periodic systems* PhD thesis, Universität Regensburg, Berlin, **2012**.

[244] Jung, D.; Whangbo, M.-H.; Alvarez, S. *Inorg. Chem.* **1990**, *29*, 2252.

[245] Mandrus, D.; Migliori, A.; Darling, T. W.; Hundley, M. F.; Peterson, E. J.; Thompson, J. D. *Phys. Rev. B* **1995**, *52*, 4926.

[246] Sesselmann, A. *Investigation on the Thermoelectric and Structural Properties of Cobalt-Antimony based Skutterudites and Modifications with Indium and Rare-Earth Elements* PhD thesis, Universität Augsburg, **2012**.

[247] He, T.; Chen, J.; Rosenfeld, H. D.; Subramanian, M. A. *Chem. Mater.* **2006**, *18*, 759.

[248] Harnwunggmoung, A.; Kurosaki, K.; Plirdpring, T.; Sugahara, T.; Ohishi, Y.; Muta, H.; Yamanaka, S. *J. Appl. Phys.* **2011**, *110*, 013521.

[249] Qiu, Y.; Xi, L.; Shi, X.; Qiu, P.; Zhang, W.; Chen, L.; Salvador, J. R.; Cho, J. Y.; Yang, J.; Chien, Y.-c.; Chen, S.-w.; Tang, Y.; Snyder, G. J. *Advanced Functional Materials* **2013**, *23*, 3194–3203.

[250] Schlecht, S. personal communications.

[251] Noda, Y.; Masumoto, K.; Ohba, S.; Saito, Y.; Toriumi, K.; Iwata, Y.; Shibuya, I. *Acta Crystallogr.* **1987**, *C43*, 1443–1445.

[252] G. Rousse, S. K.; Saitta, A. M.; Rodriguez-Carvajal, J.; McMahon, M. I.; Couzinet, B.; Mezouar, M. *Phys. Rev. B* **2005**, *71*, 224116.

[253] Rajagopalan, S. *Solid State Communications* **1969**, *7*, 1647 – 1648.

[254] Miller, A. J.; Saunders, G. A.; Yogurçu, Y. K. *J. Phys. C* **1981**, *14*, 1569–1584.

[255] Hultgren, R. *Selected Values of the Thermodynamic Properties of the Elements;* American Society for Metals: Metals Park, Ohio, 1973.

[256] Wagman, D. D. *Natl. Bur. Stand. Tech. Note* **1973**, *148*, 270.

[257] Wagman, D. D. *Natl. Bur. Stand. Tech. Note* **1968**, *191*, 270.

[258] Wei, S.-H.; Zunger, A. *Phys. Rev. B* **1997**, *55*, 13605.

# Acknowledgements

There are many people who have contributed either directly or indirectly to the success of my thesis. I am very grateful to these people and, unfortunately, can only mention a selection by name.

First and foremost I would like to express my sincerest gratitude to my supervisor Prof. Dr. Beate Paulus for her support and help throughout my thesis. She allowed me the room to roam around in my research field and to follow my own research ideas, whilst steadily guiding my independent work where it was necessary. I am grateful for the opportunities to stay in the Crystal group or to attend conferences and workshops all over the world. They broadened my scientific horizon and have often been a delight.

I am very grateful to Prof. Dr. Thomas Risse, who willingly accepted the task as second referee. His broad range of expertise in many scientific fields inspired my own efforts to gather knowledge.

In this sense, I would also like to thank Prof. Dr. Jörn Manz for all the things he taught me and for his support in many ways.

The postdoctoral researchers during my time in the Paulus group were always open for questions and gladly helped whenever their schedule allowed it. I would like to thank Dr. Elena Voloshina, Dr. Krista Steenbergen, Dr. Carsten Müller and Priv.-Doz. Dr. Dirk Andrae for discussions, their support and our nice cooperations. For the enjoyable working atmosphere I would like to thank the whole Paulus group and the groups of Jun.-Prof. Dr. Bettina Keller and Dr. Jean Christoph Tremblay.

There are many colleagues to whom I am grateful for collaborations, joint work or discussions related to my research. I am very grateful to Marcel Quennet, who I had the pleasure to co-supervise during his master thesis on skutterudite surfaces. His independence and enthusiasm allowed us to go beyond stoichiometric slabs. During their scientific internships I enjoyed to co-supervise and cooperate with Philomena Schlexer, Kai Töpfer, Clemens Richter and Guiseppe Sansone. For a very productive cooperation in the field of $FeSb_3$ skutterudites I would like to thank Prof. Dr. Manfred Albrecht, his group and in particular Marcus Daniel and Felix Timmermann, with whom cooperating was a delight and discussions always productive. I am very grateful to our SPP 1386 organizers, cooperation partners and the members of their group, in particular Dr. Sabine Schlecht and Prof. Dr. Eckhard Müller. For the name inspiration of BUCKELWAL I thank Emanuel Hupf.

In 2013 I had the pleasure to work in the group of Prof. Dr. Roberto Dovesi in Torino and to cooperate with Dr. Lorenzo Maschio. The whole group greeted me with nothing but kindness, especially Prof. Dovesi, for which I am very grateful. In particular I would like to thank Lorenzo Maschio for the organization of, the supervision during and the ongoing support after my stay. Additionally, I am very grateful to the following people who contributed with discussions or their expertise to my work in Turin (in alphabetical order): Dr. Silvia Casassa, Dr. Bartolomeo Civalleri, Dr. Roberto Orlando, and Dr. Denis Usvyat. For the introduction to “la dolce vita” in Torino and their friendship during my stay I would like to give special

thanks to (in order of appearance) Agnes Mahmoud, Valentina Lacivita, Simone Salustro, Alessio Masala, Dr. Alessandro Erba, Dr. Marco Lorenz.

Many people contribute to ensure the smooth working of a university. As representatives for all those who contribute, I would like to thank Julija Djordjevic for her continuous help with bureaucracy, and Bernd Melchers, Boris Proppe, Robert Schüttler, and Holger Weiß for technical support. Computer resources and technical support were provided by the North-German Supercomputing Alliance (Norddeutscher Verbund zur Förderung des Hoch- und Höchstleistungsrechnens - HLRN) and the Zentraleinrichtung für Datenverarbeitung (ZE-DAT).

I am very grateful for the opportunity to be a member of the International Max Planck Research School (IMPRS) "Functional Interfaces in Physics and Chemistry". As for the universities, there are many people responsible for a successfully operating research school. In this way I want to thank all of the contributers and in particular Bettina Menzel and Dr. Tobias Kampfrath.

There are many people who listened to my problems, cheered me up when I was desperate or took care of a well-earned distraction. I consider myself lucky to call them my friends. First, I would like to thank Dr. Axel Schild with whom I share many great memories that make me laugh in retrospect, but also for his support and the many discussions about science and life in general. Secondly, I would like to thank Elisa Kanaki who, in her own very different and great way, substituted Axel so well in our office. Together, we have shared many unforgettable moments above the ground. Furthermore in this respect I want to thank all the other people who supported me during the time of my thesis, and especially (in alphabetical order) Katharina Branz, Claudia Brieger, Zita Hüsges, Eva Mazgaj, Matthias Mundt, Juliane Krüger, Jenny Rahn, Simon Reiske, Hendrik Ronneburg, Nicole Schrader, Nina Volkamer, Daniel Ziemens, and Jenny Zieschang.

Financial support by the priority program SPP 1386 "Nanostrukturierte Thermoelektrika: Theorie, Modellsysteme und kontrollierte Synthese." of Deutsche Forschungsgemeinschaft (DFG) is gratefully acknowledged. Travel funds by the International Max Planck Research School (IMPRS) are highly appreciated.

Last but not least, I would like to thank my whole family – to which I dearly count Marianne and Hans Flückiger – for their support, their understanding and for providing a place of retreat.